Universidad Autónoma de San Luis Potosí

Centro de Investigación y Estudios de Posgrado

Facultad de Ingeniería

Analysis, Tuning of Controllers and Interconnection of a Battery Energy Storage System for Subsynchronous Resonance Mitigation in Wind Farms.

Tesis que para obtener el grado de:

Doctor en Ingeniería Eléctrica

Presenta:

M.I. Roberto Moreno Sánchez

Asesora:

Dra. Nancy Visairo Cruz

Coasesor:

Dr. Ciro Alberto Núñez Gutiérrez

México, San Luis Potosí, S.L.P.   Febrero 2022

Analysis, Tuning of Controllers and Interconnection of a Battery Energy Storage System for Subsynchronous Resonance Mitigation in Wind Farms ©

Dedicatoria

Dedico este trabajo a...

Dios...

a mi madre Ma. del Carmen y mi padre Roberto...

a mi hermana Sandra Mónica...

a mis hermanos Calixto, José Salvador y Eduardo...

a Eli...

"In the middle of difficulty lies opportunity."

... Albert E.

Agradecimientos

Resumen

La generación de energía eólica es la energía verde más prometedora para generación en grandes cantidades, y de acuerdo al Consejo Mundial de Energía Eólica (GWEC por sus siglas en Inglés), cada generación de aerogeneradores, se vuelve más rentable. Basados en el GWEC, el sistemas de conversión de energía eólica (WECS por sus siglas en Inglés) es la mejor solución para contribuir en contra del cambio climático. A pesar de que es una solución prometedora, esta tecnología presenta problemas asociados con su topología. El problema más notable se presenta debido a que, usualmente la ubicación de los WECS se encuentran retiradas de las instalaciones de consumo, como ha sido bien reportado

En cualquier inversión, la ubicación de estos parques eólicos requiere una planeación minuciosa. Al mismo tiempo, debido a la preocupación medioambiental, la construcción de nuevas líneas de transmisión aéreas es cuestionada. En este contexto, líneas de transmisión compensadas en serie son una excelente solución, ya que permite mayor capacidad de transmisión a través de las líneas existentes a una fracción del costo y pérdida de tiempo comparado con la construcción de una nueva línea de transmisión. Sin embargo, líneas de transmisión compensadas en serie son propensas a oscilaciones subsíncronas originadas por resonancia subsíncrona. Este es un fenómeno relativamente nuevo debido a que la primera vez que éste fue observado in un WECS fue en el 2003.

Considerando el contexto, esta Tesis aborda el problema de resonancia subsíncrona en líneas de transmisión compensadas en serie usando un marco de referencia de un parque eólico basado en un sistema DFIG. También, para explorar una posible solución para mitigar este problema, la incorporación de un sistema de almacenamiento de energía por baterías es incluida y analizada utilizando herramientas matemáticas para determinar su influencia en el mejoramiento de la confiabilidad de todo el sistema.

Como resultado, una metodología para la sintonización de los controladores de un convertidor back-to-back de el aerogenerador basado en un DFIG es llevada a cabo. Las herramientas matemáticas usadas en sistemas de potencia son implementadas para identificar los modos relacionados con resonancia subsíncrona, también enfoques matemáticos son propuestos para comprender las causas que producen resonancia subsíncrona. Un proceso de discriminación e identificación para resonancia subsíncrona es propuesto. Fi-

nalmente, la integración de un sistema de almacenamiento de energía por baterías es estudiado así como un esquema posible que contribuya a mejorar el desempeño de la instalación cuando éste se encuentre en una condición de resonancia subsíncrona; para este propósito dos esquemas para el sistema de almacenamiento de energía por baterías son analizados para la mitigación de la resonancia subsíncrona.

Abstract

Wind generation is the most promising green power for bulk production and, according to the Global Wind Energy Council (GWEC), each generation of wind turbines becomes more cost-efficient. Based on GWEC, wind energy conversion systems (WECS) is the best solution for contributing to climate change. Although this is a promising solution, this technology brings troubles associated with its topology. The most remarkable issue occurs because usually, the location of WECS is far away from the consumption facility, as it is well reported.

For any investment, the location of these wind farms requires thorough planning. At the same time, environmental awareness questions the construction of additional overhead transmission lines. In this context, series-compensated transmission lines are an excellent solution since enabling more power to be transmitted through existing lines at a fraction of the cost and time expenditure of a new line. However, series-compensated transmission lines are prone to subsynchronous oscillations originated by subsynchronous resonance. This is a relatively new phenomenon due to that the first time it was observed in a WECS was in 2003.

Considering the context, this Thesis addresses the problem of subsynchronous resonance in series compensated transmission lines using as a benchmark a DFIG-based wind farm for study case. The aim of this research work is to analyze thoroughly the reasons that provoke the subsynchronous resonance, putting special focus on its consequences in DFIG-based wind farms. Also, to explore possible solutions for mitigating this problem, the incorporation of a battery energy storage system is included and analyzed using mathematical tools to determine its influence to improve the reliability of the whole system.

As a result, a methodology for tuning the controllers of the back-to-back converter of the DFIG-based wind farm is performed. Mathematical tools used in power systems are used to identify the modes related to the subsynchronous resonance, also a mathematical approach is proposed to understand the causes that produce subsynchronous resonance. A discrimination and identification process for subsynchronous resonance is proposed. Finally, the integration of a battery energy storage system is studied as a possible scheme that contributes to improving the facility performance when it lies in a subsynchronous

resonance condition; for that purpose, two schemes for the battery energy storage system are analyzed to the subsynchronous resonance mitigation.

Contents

List of Figures

List of Tables

Acronyms

Table 1: Acronyms.

Abbreviation	Definition
AC	Alternating Current
BESS	Battery Energy Storage System
DC	Direct Current
DFIG	Doubly Fed Induction Generator
DPI	Driving Point Impedance
ERCOT	Electric Reliability Council of Texas
ES	Eigenvalue Sensitivity
FACT	Flexible AC Transmission System
GCSC	GTO Thyristor-Controlled Series Capacitor
GSC	Grid-Side Converter
GSCC	Grid-Side-Converter Controller
HVDC	High Voltage Direct Current
IEEE	Institute of Electrical and Electronics Enginering
IGE	Induction Generator Effect
MI	Modal Impedance
ODES	Ordinary Differential Equation System
PF	Participation Factors
PLL	Phase-Locked Loop
pu	Per Unit
PWM	Pulse Width Modulation
RSC	Rotor-side Converter
RSCC	Rotor-side-Converter Controller
SCIG	squirrel cage induction generator
SSCI	Subsynchronous Torsional Interaction
SSO	Subsynchronous Oscillation
SSR	Subsynchronous Resonance
SSTI	Subsynchronous Torsional Interaction
SSS	Small-Signal Stability
SSSA	Small-Signal-Stability Analysis
SSSC	Synchronous Series Compensator
SVC	Static Voltage Converter
TA	Torque Amplification
TCSC	Thyristor-Controlled Series Capacitor
TI	Torsional Interaction
TSSC	Thyristor-Switched Series Capacitor
VSC	Voltage Source Converter
WECS	Wind Energy Conversion System
WRIG	Wound Rotor Induction Generator

Chapter 1

Introduction

This introductory chapter has a purpose to provide the background, the motivation, hypothesis, and the scope of the Thesis.

1.1 Background of Subsynchronous Interactions Issue

The subsynchronous phenomena are divided into subsynchronous resonance, subsynchronous torsional interaction, and subsynchronous control interaction. In the context of subsynchronous phenomena [5], it is worthwhile to give the definition and understanding of basic concepts.

Subsynchronous Interaction

"Subsynchronous interaction is a general term that defines two parts of an electric-mechanical system exchanging energy with each other at one or more of the natural frequencies of the combined system below the fundamental frequency of the system. The energy exchange can be from the electrical to the mechanical subsystem or from the electrical to another electrical subsystem of a complete generation system" [5, 6], as it is shown in Figure 1.1.

Subsynchronous Oscillations

"Subsynchronous oscillation is a general term that defines the result of SSI described above". This term defines the effect of SSI in the system; the subsynchronous oscillations are observed with a low frequency below of synchronous frequency (50 Hz or 60 Hz), [5, 6].

Natural frequency

"The natural frequency refers to the frequency at which the electrical or mechanical system can resonate if it is disturbed at such frequency" [7].

Subharmonic

"This is a general term in which the frequency is below the fundamental frequency but at reflections of the harmonics (i.e., 1/2 - 30 Hz, 1/3 rd - 20 Hz for a 60 Hz as fundamental frequency)", [7].

Harmonics

"Harmonics are frequencies that are multiples of the fundamental frequency (i.e. 2nd - 120Hz, 3rd - 180 Hz for a 60 Hz of fundamental frequency)", [7].

General Classification of Subsynchronous Interactions

Figure 1.1 shows the general classification of the subsynchronous issues. This Thesis considers the classification shown in this figure. In general terms, SSR involves the mechanical part, electromechanical part, and series-compensated transmission line; SSTI involves the mechanical part and voltage source converter controllers; SSCI involves the VSC controllers and series-compensated transmission line [5, 6]. The specific description of each phenomenon is shown in detail in the following sections.
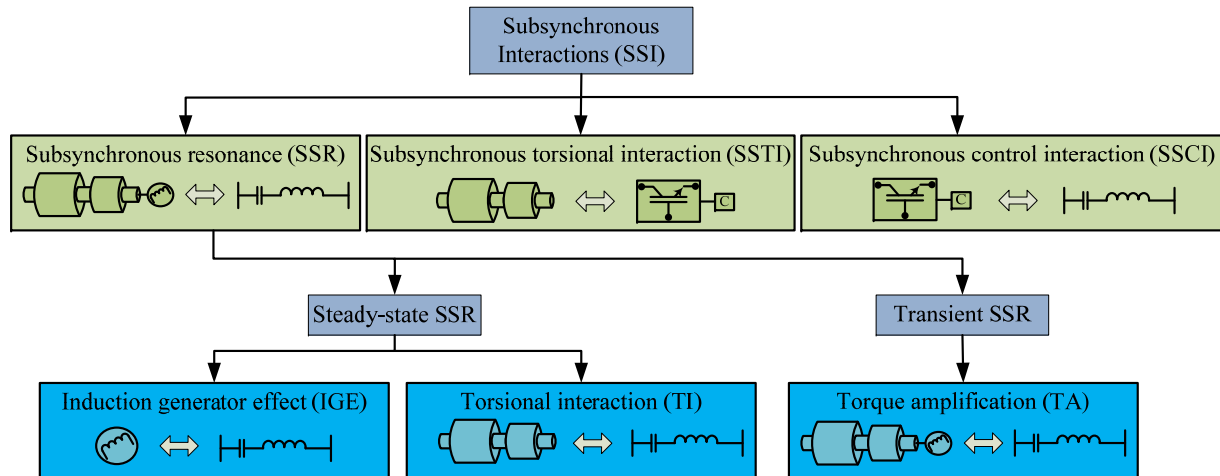
Figure 1.1: General classification of the phenomena involved in subsynchronous issues [1].

1.1.1 Subsynchronous Resonance

Series capacitors for transmission lines have been installed worldwide for many years and various purposes related to, economical benefits [8], voltage stability, voltage regulation, transient stability improvement [9], and power oscillation damping [10]. Those applications are successfully applied in improving the system performance, but, series capacitors

in transmission lines can bring some troubles related to sustained oscillations at frequencies below the system fundamental frequency, this phenomenon is called subsynchronous resonance and was firstly described in 1937 [10]. In spite of the phenomenon was described in 1937, it received attention until the 1970s, when, in Mohave Generating Station the failure of two turbine-generator shafts was observed two times in 1970 and a few months later in 1971 [11, 12]. After the repeated incidents, the phenomenon started to take interest leading to the understanding and development of solution methods, like [13] wherein 1971 describes a method for calculating the subsynchronous frequencies of the resonance due to self-excitation oscillations. After, in January 1972, a measurement system was implemented in Mohave Generating Station, where the real system was tested with the injection of small disturbances by insertion of series capacitor modulus. As a result, the first paper on "subsynchronous resonance in series compensated transmission lines" with experimental results was published in 1973 [11, 14]. In this sense, the electrical features of Mohave Generating Station were published in [15], where the location and geographical distribution of the system, the generating equipment, the one-line diagram, in general, the complete system is described for further investigations.

After the incidents, several papers have been published dealing with SSR, in parallel, the new technologies for the mitigation techniques have been evolving, as well. As a result, protection schemes applied to flexible AC transmission systems such as GTO thyristor-controlled series capacitor, thyristor-switched series capacitor, thyristor-controlled series capacitor, and less common static synchronous series compensator are used to mitigate SSR [16, 17, 18]. For example, in [18] the capabilities of the GCSC to mitigate SSR is verified in a steam turbine generator in a series compensated transmission line. As reported by [19] a study based on impedance models is carried out to investigate the impact of VSC to damp SSR problems, similar to [20] where a control scheme of VSC-based is proposed to mitigate the subsynchronous oscillations in a turbine-generator system. In [21] the authors developed a supplementary excitation damping control to mitigate SSR caused by a series compensated transmission line.

According to the formal definition given by the IEEE [5, 6, 11], "Subsynchronous resonance is an electric power system condition where the electric network exchanges energy with a turbine generator at one or more of the natural frequencies of the combined system below the synchronous frequency of the system".

Based on [5, 6, 11], the general series compensated system is shown in Figure 1.2, the frequencies of subsynchronous resonance can be defined by:

$$f_{er} = f_o \sqrt{\frac{X_C}{X'' + X_E + X_T}} = f_o \sqrt{\frac{X_C}{X_{tot}}} \tag{1.1}$$

where

f_{er} is the electrical system resonant frequency or natural frequency of the electrical system.

f_o is the system frequency.

X_C is the reactance of the series capacitor.

X'' is the average sub-transient reactance.

X_E is the reactance of the transmission line.

X_T is the transformer reactance.

X_{tot} is the sum of the all system inductive reactance, e.g. $X'' + X_E + X_T$.
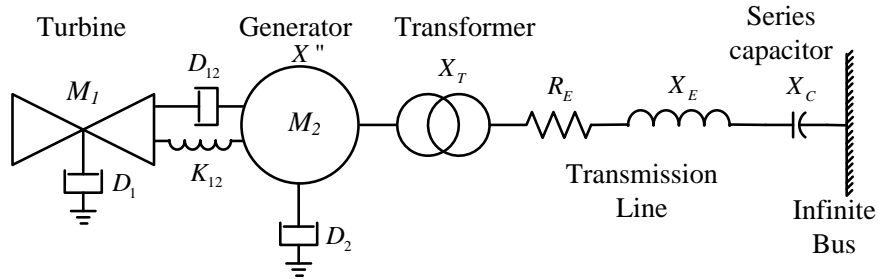
Figure 1.2: Turbine-generator system with compensated transmission line.

Generally, the series compensated transmission system is more complex and will result in many subsynchronous frequencies (f_{er}) [5].

SSR can be divided into three phenomena, two of them produce self-excitation, induction generator effect, and torsional interaction, the third one produces torque amplification; explained as follows.

Induction Generator Effect

In this case, self-excitation is produced by IGE and the rotor speed of the generator is assumed as constant (the rotor is rigid). "IGE involves an electric machine with the network and it is a purely electrical phenomenon, there is no mechanical system involved. IGE occurs due to the differences between the speed of the rotating magnetic field and the rotor speed of the generator", [5, 6]. From the point of view of a subsynchronously rotating stator flux, the synchronous generator acts as an induction machine [1]. Then, for synchronous and induction machines the slip at subsynchronous frequencies is described by [14]:

$$S_{ssr} = \frac{f_{er} - f_r}{f_{er}} \tag{1.2}$$

where:

   S_{ssr} is the slip at subsyncrhonous frequencies.

   f_r is the electrical rotor speed.

From the equivalent circuit of the induction machine, shown in Figure 1.3, the equivalent rotor resistance seen from the stator terminals at subsynchronous frequency is given by [1]:

$$R_{eq}^{S_{ssr}} = \frac{R_r}{S_{ssr}} \tag{1.3}$$

where:

$R_{eq}^{S_{ssr}}$ is the equivalent resistance seen from the stator terminals.

R_r is the rotor resistance.

The equivalent resistance for the synchronous machine can be calculated as in [14]. In the series compensated transmission line, the inequality $f_{er} < f_r$ is fulfilled (for SSR), S_{ssr} is negative, then $R_{eq}^{S_{ssr}}$ is negative. If the magnitude of $R_{eq}^{S_{ssr}}$ (seen from the stator terminals) exceeds the sum of the stator and network resistance, the system experiment a negative damping at subsynchronous frequency and the induction generator effect is observed.
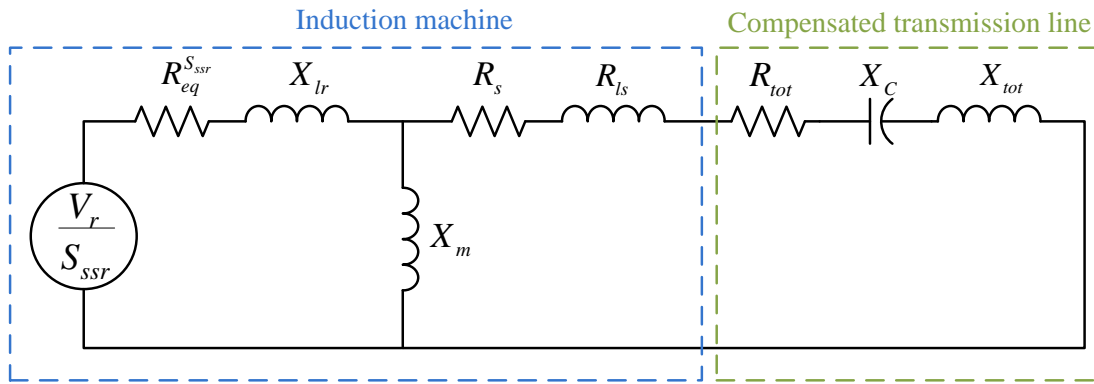
Figure 1.3: Equivalent circuit of the induction machine.

Torsional Interaction

"TI is the interaction between the turbine-generator mechanical system and a series-compensated electrical network. Small-signal disturbances in a power system result in simultaneous excitation of all-natural modes of the electrical and mechanical systems" [11]. For the simplified system shown in Figure 1.2, the natural mechanical frequency, neglecting damping (D), is given by (1.4).

$$f_n = \sqrt{\frac{K_{12}}{(M_1 M_2)/(M_1 + M_2)}} \tag{1.4}$$

where:

f_n is the mechanical system resonant frequency or natural frequency of the mechanical system.

M_{1-2} are the moment of inertia for the turbine and the generator, respectively.

K_{12} is the shaft stiffness.

Just as the electrical system, the real mechanical system (hydro turbine-generator) is multi-modal and will have more than one natural frequency. Oscillations of the generator rotor at this frequency result in modulation of the generator voltage [11]. These rotor torsional oscillations rendering to the generator terminals produce stator voltage components at the frequencies of:

$$f_{en} = f_o \pm f_n \tag{1.5}$$

When the frequency f_{en} is close to a natural frequency of the electrical system (f_{er}), the resulting armature currents produce a magnetic field which is phased to produce a torque which reinforces the aforementioned generator rotor oscillations. Then, the self-excitation phenomenon is observed produced by TI [11, 14].

Torque Amplification

"TA involves mechanical and electrical systems. TA occurs due to faults in the network or during switching operations. This results in system disturbances, which impose electromagnetic torques on generator rotors, subjecting shaft segments to torsional stresses", [11]. Following a significant disturbance in a series-compensated system, the resulting electromagnetic torque oscillates at frequencies of:

$$f_m = f_o \pm f_{er} \tag{1.6}$$

where f_m is the induced subsynchronous and supersynchronous frequency in the generator. If f_m corresponds to a natural torsional vibration frequency (f_n) of the turbine-generator shaft system, the magnitude of the rotor oscillations are greatly amplified, then TA is observed. It is shown that the oscillations frequencies at $f_m = f_o + f_{er}$ are reasonably well damped [11, 14].

1.1.2   Subsynchronous Torsional Interaction

The potential of interactions due to subsynchronous modes of turbine-generator shafts and electrical devices on bulk-power transmission systems has long been considered. For example, in 1970 the first phenomenon of SSR due to a series-compensated transmission line was observed, as it is described in Section 1.1.1. On the other hand, the new technology brings new challenges as the phenomenon called SSTI. This phenomenon is relatively new and involves an interaction between generator and power electronic devices such as HVDC, FACTS, power electronics devices, or other power electronic controllers [11, 22].

In October 1977, the HVDC system at Square Butte in North Dakota was interacting in an adverse way with an 11.5 Hz torsional mode of an adjacent turbine-generator unit [23]. Conforming to some publications, this is the first time where SSTI was observed [22, 24, 25]. As reported by [1, 7], SSTI defines the problem of a turbine generator near a power electronic controller when the mechanical system resonates with the negative

damping of the controller at sub-synchronous frequencies.

Essentially, the natural torsional vibrations of a turbine generator produce a slight modulation in the internal voltage of the machine, and, consequently, the voltage measured at the FACTS location. This variation in voltage causes control action through the voltage regulator of a nearby FACTS, producing a subsequent change in the electrical torque of the machine. Under the proper combination of circumstances, the modulation of electrical torque of the machine by the FACTS can reinforce the torsional vibrations in the machine rotor [22, 23].

1.1.3 Subsynchronous Control Interaction

According to [1, 7], "SSCI is an interaction between a power electronic control system (such as an HVDC link, SVC, and so on) and a series-compensated electrical network. SSCI involves only the electrical system and it is not related to the mechanical system". In October 2009, the first event known as SSCI was described in [26], the SSCI occurred in Electric Reliability Council of Texas system wind farm. This is the only one reported as a wind-farm exclusive phenomenon.

SSCI is the newest phenomenon reported under the subsynchronous oscillations family, in this sense, SSCI has not been investigated thoroughly and is not well-documented [24]. For example, the ERCOT study case is the only one reported in the literature and the effects of SSCI are not observed in steam or hydro turbine-generator systems.

There is a discussion about if SSCI is a new phenomenon, in a like manner, other researchers have questioned the veracity of SSCI [27]. ABB commented that SSCI is a misnomer because it is only a self-excitation phenomenon due to the induction generator effect is observed in asynchronous machines [24, 28, 29].

1.2 Background of Wind Energy Conversion Systems

The phenomena described in the previous sections were firstly stated for conventional generation (as turbine-generator based steam or hydro) systems, unlike SSCI which has been observed only on wind generation. In accordance with the analysis conducted by several authors [1, 24], SSI can be observed in wind energy conversion systems. In this sense, the types of WECS are explained, as well.

1.2.1 Wind Energy Conversion Systems Technologies

Despite the wind power has been exploited for more than 3,000 years, it was only until the early twentieth century that wind power was used to generate electricity. The records indicate that, in 1891, the Dane Poul La Cour was the first to build a wind turbine used to generated electricity [30]. In this context, the equipment to generate electricity with wind

power has evolved in several types of technologies. In this Thesis, the main technologies are explained and the most used WECS is analyzed.

In general terms, there are two basic WECS, with vertical and horizontal axis, this section describes the most common applied WECS of horizontal axis due to this investigation is focuses on those topologies. With the oil crisis at the beginning of the 1970s, wind power generation reinforce its importance, in this sense, the type 1 to type 4 WECS configurations have been developed since then. In the following sections, those technologies will be briefly described. It should be noted that some authors describe type 5 or even type 6 wind turbines, but these topologies arise from the combination of the previous four [31, 32].

Type 1 or Type A-based WECS Configuration: Fixed-Speed

The type 1 denotes a fixed-speed wind turbine with an squirrel cage induction generator directly connected to the grid via a transformer. The SCIG-based WECS is shown in Figure 1.4, this is the oldest and very first technology developed for wind turbines. The operation of type 1 wind turbine can be described as follows [31]:

- The gearbox is required to match the speed difference between the turbine and the generator.
- The generator speed varies 1 % around its corresponding synchronous speed at different wind speeds, and thus this configuration is called fixed-speed WECS.
- The soft-starter is bypassed after the start-up procedure.
- The SCIG draws reactive power from the system, to compensate this, a three-phase capacitor banks are usually employed.
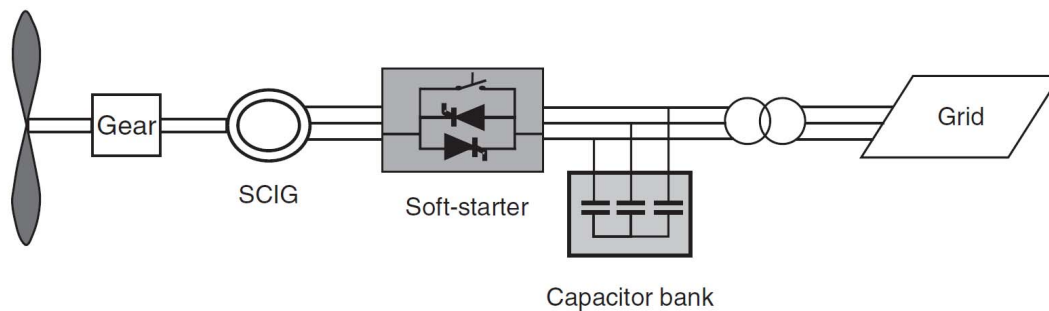
Figure 1.4: Type 1 or type A-based WECS configuration.

The operation of type 1 WECS encompasses several advantages as:

- Simplicity.
- Low initial cost.
- Reliable operation.

The drawbacks can be listed as follows:

- Low wind energy conversion efficiency.
- The changes in the wind speed are reflected to the grid.
- The grid faults cause several stress on the mechanical components of the wind turbine.

Type 1 WECS stopped being popular to be installed in wind parks in the years 1995 to 2000 when the semi-variable speed with power electronics began to become popular [32]. On the decay of type 1 WECS, at the end of 2001, the global installed of wind energy was 24 GW, which represents less than 4% of the actual global installation [33]. As stated by [31], the installed type 1 WECS are in the majority still working. Currently, there are no manufacturers that commercialize this wind energy technology (outdated). The rated power of type 1 wind turbines was from 50 kW to 2.3 MW. The main manufacturers were Vestas and Siemens.

Type 2 or Type B-based WECS Configuration: Semi-Fixed Speed

Type 2 denotes a semi-fixed speed wind turbine with a wound rotor induction generator directly connected to the grid via a transformer. The WRIG-based WECS is shown in Figure 1.5, the variable resistance connected to the rotor circuit allows to increase the variability of the rotor speed. Typically, the speed range is $0-10\%$ above the synchronous speed. Like type 1, the type 2 wind turbine draws reactive power from the system, then a three-phase capacitor bank performs the reactive power compensation. The softstarter is bypassed after the start-up procedure.

Type 2 wind turbine increases the energy conversion efficiency, and reduces the mechanical stress caused by wind gust. The rotor resistance is normally made adjustable by a power converter composed of a diode-rectifier and a chopper [31]. With variable-speed operation, the system captures more power from the wind, but also has energy losses in the rotor resistance.

Since the mid-1990s, the Danish manufacturer Vestas (among others) has used this technology with a power rating up to a couple of megawatts. A few examples of commercial solutions are: Vestas V66 of 2.0 MW and Suzlon Energy S88 of 2.1 MW. This configuration is also becoming less important among the wind turbine manufacturers due to limited speed range and low energy conversion efficiency, nowadays this configuration is not longer installed and less and less analyzed [30, 31, 34].

Type 3 or Type C-based WECS: Semi-Variable Speed

Since 2000, with the advancement of the two level Voltage Source Converters (2L-VSC) with bidirectional power flow, the power electronics started to handle the WECS. In that year, the double fed induction generator (or type 3) wind turbine started take relevance, in such a way that the size of the wind turbines started to increase from around 1.5 MW (from the manufacturer Acciona, Fuhrlander, Gamesa, among other) to sizes of 5 or 6 MW
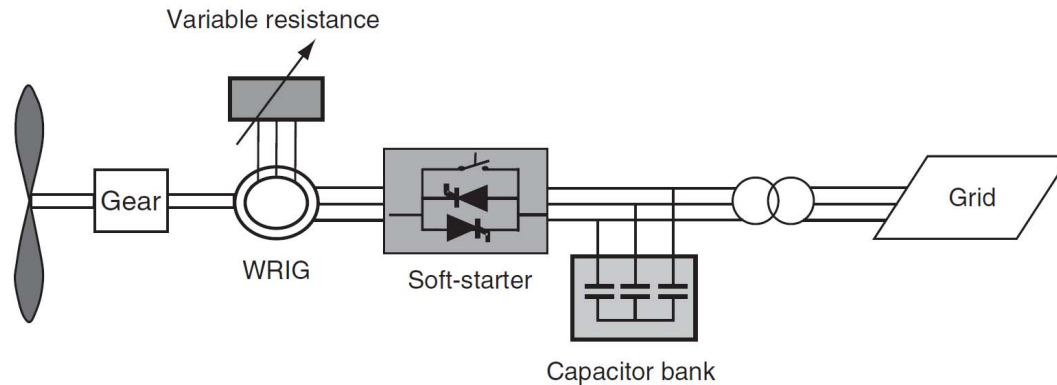
Figure 1.5: Type 2 or type B-based WECS configuration.

(from the manufacturers Bard and Repower, respectively). Figure 1.6 shows the general configuration of the DFIG-based turbine.

As the name implies, the power from the generator is fed to the grid through both stator and rotor windings. There are some big advantages of DFIG-based WECS between type 1 and 2 wind turbines, the variable speed is around 30% of the rated speed and there is no need of a soft starter, but in this configuration, a gearbox is still required.

This configuration improves the power conversion efficiency by first time performing maximum power point tracking [35, 36], in comparison with type 1 and 2 wind turbines, the dynamic performance and robustness against power system disturbance are enhanced.

This features have made DFIG-based WECS the dominant technology with approximately 50% of the world-wide installations. Despite of all the advantages, the main drawback is that the life time of brushes connected to slip rings is about 6-12 months. This maintenance is essential for the proper operation of the power converter connected to the rotor-side. This drawback is the cause of this wind turbine is not installed in the offshore environment.

Other particular aspects of the DFIG-based WECS is that, the power converter is about 30% of the rated wind turbine power. The typical range of the rotor speed from its synchronous speed is −40% to +30%. Other attractive benefit is due to the small size of the back-to-back converter; this topology is quite attractive from the economical point of view [30].
The benefits about the use of power converter in this topology can be listed as follows:

- Easy energy management.
- Reduced mechanical stress in the drive train.
- Reduced noise.
- Controlled active and reactive powers.
- The grid-side converter can be used as a reactive source.
- Improve the network stability by controlling its stator voltage.
- Improves power quality in the presence of external disturbances.

On the other side, the use of power converter in this topology can lead to the following disadvantages:

- The power converter implies an extra cost.
- There are extra losses due to the power switches.
- The power converter is a source of harmonics.
- The resonance due to harmonic is a problem.
- The low harmonics (below synchronous frequency) are a concerning problem.
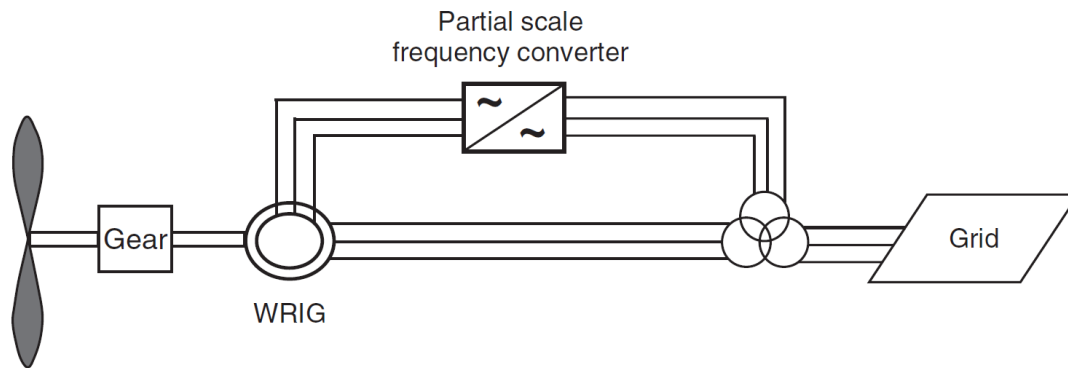
Figure 1.6: Type 3 or type C-based WECS configuration.

Despite of its benefits, the difficulties associated in complying with grid-fault ride-through requirements may limit its use in the future [34].

Type 4 or Type D-based WECS: Full-Variable Speed

The new type 4-based WECS is also know as full-rate wind turbine converter. This is the newest of the WECS family. The main aspect of this configuration is that the generator is not connected directly to the grid (fully decoupled), but rather the full-rate power converter is connected between the generator and grid, i.e., the DC-link provides decoupling between the generator and the grid [31]. In this sense, the power converter must manage the 100% of the power delivered by the wind turbine. Figure 1.7 shows the general configuration of the type 4 WECS.

There are important advantages of type 4 wind turbine, e.g. in this topology the permanent magnet synchronous generator, wound rotor synchronous generator, and wound rotor induction generator can be used. Due to full-rate power converter (or known as full-scale power converter) the type 4 wind turbine can operate at fully speed range $(0-100\%)$.

The full-rate power converter must be rated same as the generator capacity which increase the total cost of the wind turbine, weight, size, complexity of overall system increases, the losses are higher leading to low efficiency. But, the flexibility of operation in a high range of wind speed can overcome the disadvantages.

The full-rate power converter give extra advantages as, active and reactive power control, the overall wind energy efficiency is increased in comparison of the type 1 to 3 wind turbines, the use of gearbox can be eliminated by using a high number of poles in the generator. This configuration is more robust against system faults than type 1 to 3 wind turbines [30, 31, 34].
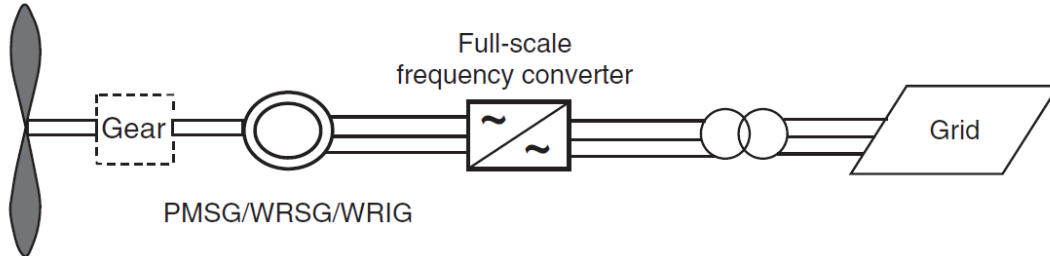
Figure 1.7: Type 4 or type D-based WECS configuration.

In general, the advantages and disadvantage of using power electronic can be summarized as the ones showed in previous section. Due to the power converter, the stator voltage, electric torque, rotor speed, and pitch angle of the blades can be controlled.

1.2.2 Overview of Wind Energy Generation

As reported by the Wind Energy Report [2] and despite the COVID-19 pandemic, 2020 saw global new installation surpass 90 GW, 53% growth compared to 2019, bringing total installed capacity to 743 GW worldwide, a growth of 14 % compared to last year. Figure 1.8 shows the new installation of power capacity for onshore and offshore wind energy.

New installations in the onshore wind market reached 86.9 GW, while the offshore wind market reached 6.1 GW, making 2020 the highest and the second highest year in history for new wind installations for both onshore and offshore.
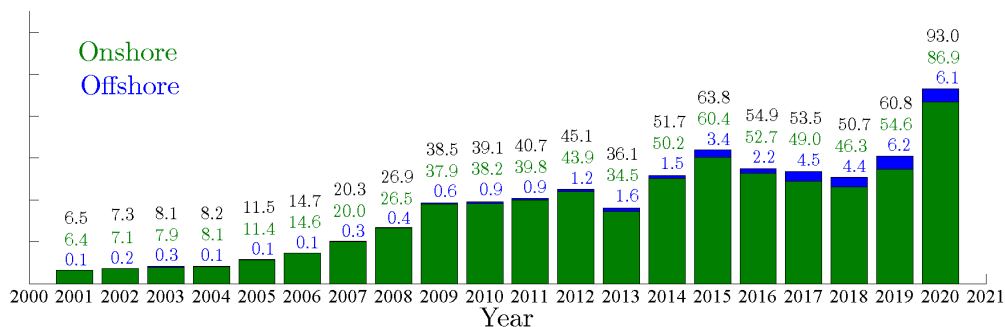
Figure 1.8: Total of new installation of wind power in GW [2].

Figure 1.9 shows the main markets of 2020 which lead the new installation of wind power capacity. In the first place by region, China, Asia Pacific (APAC) is the region

which leads the market installation in 2020. Latin America (LATAM) only contributes to the worldwide installation by 5%. By markets, China is still leading the new installations.
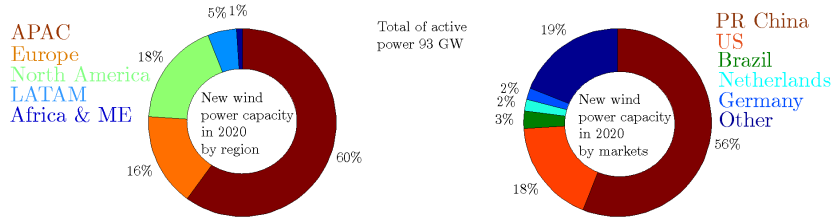
Figure 1.9: New wind power capacity by region and top five markets [2].

Table 1.1 shows the new and total installation of wind power capacity for 2019 and 2020 for the Mexican scenario. It is observed a slowdown between the years shown in the table. According to the Renewable Energy Prospects 2018-2032 of Mexico [3] published by the SENER, the wind energy is the fastest growing renewable energy according its rate of change and installed capacity with an annual growth of 47.6% from 2007 to 2017. Figure 1.10 shows the prospect of wind energy installation from 2018 to 2032; it is evident that for the year of 2020 the commitment of installation wind power capacity has not been achieved. Finally, for the 2032 is expected a total installation of 19,017 MW to fulfill the international commitment of reduce the carbon emissions.

Table 1.1: The market status for Mexico.

Onshore, MW	New inst. 2019	Total inst. 2019	New inst. 2020	Total inst. 2020
Mexico	1,281	6,215	574	6,789
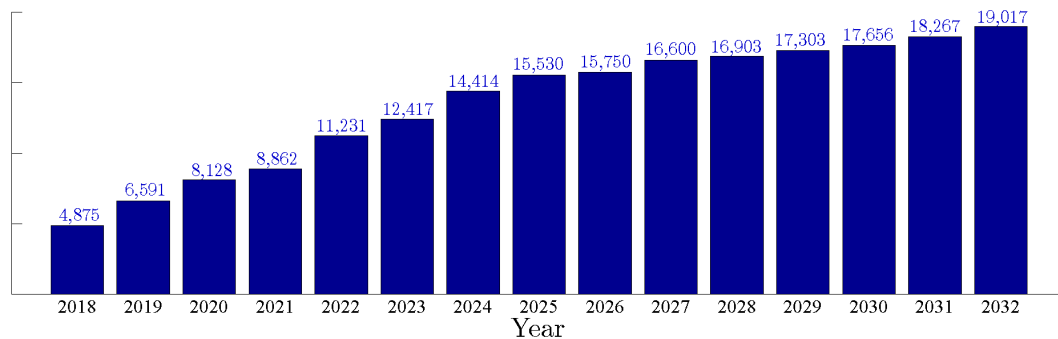
Figure 1.10: Mexican prospect of wind energy from 2018 to 2032 according the SENER, in MW [3].

Figure 1.11 shows the world development of the total installation of wind energy. It can be observed that the onshore wind farms are leading the historic installation while

the offshore installation is starting to take importance in the worldwide market. Finally, an exponential trend can be observed in the installation of WECS. The global trend on installation shows a sustained increase which indicates that wind energy is a promising source for the energy transition. As stated by the Global Wind Energy Council, wind energy will be the main tool to reach a Sustainable Energy Transition for zero carbon emissions.
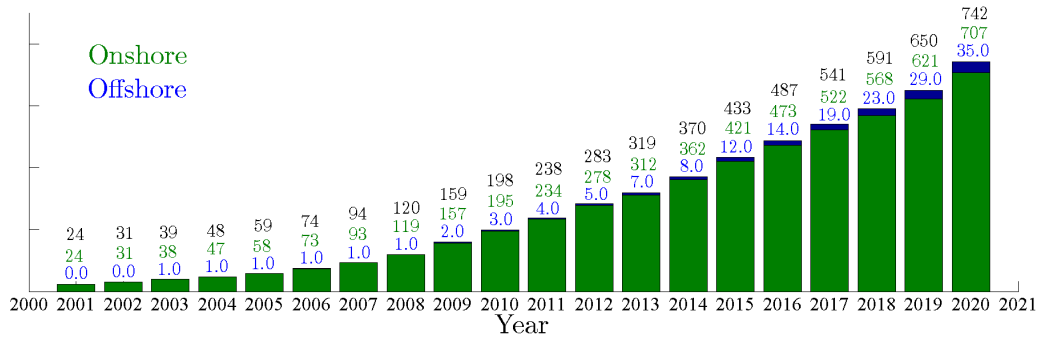
Figure 1.11: Historic development of total installation in GW [2].

1.2.3   Background of Subsynchronous Interactions in WECS

Although subsynchronous interactions are a relatively new phenomenon affecting power systems as described in previous sections, and for traditional power systems (as hydro-electric power plants) SSI is a well-known phenomenon. SSI in WECS is even a newer phenomenon; in 2003 was discussed by the first time the interaction of a series compensated transmission line with a WECS [37], where the DFIG-based WECS showed subsynchronous modes on its induction generator close to the mechanical modes.

Since then, little information was published about SSI, the investigation of this topic started to take importance in the scientific community after a well-documented event occurred in the ERCOT in 2009 [7, 28], which was called as subsynchronous control interaction. It is worth mentioning that, SSI started to be studied in wind farms due to that the phenomenon of SSR was observed in series-compensated wind systems, the published paper have demonstrated that SSI can be observed even if the transmission system is not compensated [1, 24, 38]. In this sense, the interactions among the power converters, controls, synchronous and induction generators, FACTS, HVDC-based systems, and series-compensated with wind systems are also prone in WECS, in comparison with traditional hydro-therm power plans. As a result, new technology in electric power generation brings new challenges to be overcome.

The SSI phenomenon in WECS has been studied with several control schemes or electric topologies. Besides that, one of the first papers dealing with SSI was focused on the explanation of the phenomena, as [39] which describes the phenomena in a series-compensated transmission line giving several study cases where parameters and wind speed are changed

to observe which phenomenon show up. Also, the dynamic simulations and eigenvalue analysis are carried out by PSCAD/EMTDC and MatLab/Simulink, respectively. In the same context, [1] proposes an SSI damping controller to mitigate SSCI, the study is done in a portion of the series-compensated transmission system of the ERCOT system. In the same manner, [1, 39] describes SSI phenomena, but both publications classify the SSI in a different way. Even, recent publications [40] classify SSI and SSR as synonymous terms and encompasses terms differently than [1, 39].

Under the subject of analysis techniques, impedance-models-based analysis has been used for SSI analysis where the Nyquist criteria, Bode plots, and frequency sweep techniques are used; these impedance models have been used for several years for SSI issues in WECS analysis [41, 42]. Other publication attempts to improve common analysis techniques such as frequency scan (impedance modeling), where to estimate the characteristic impedance can take a great amount of time, especially if the system is large; reference [40] proposes a method for injecting a signal with multiple frequencies at one time to optimize the impedance modeling procedure.

In other publications, e.g., Mohammad Amin and Marta Molinas deal with SSI issues in WECS systems, where its publications are mainly focused on the use of impedance modeling technique as [43] (which is similar to [44]) where, based on the impedance model, the stability analysis of VSC-based HVDC systems including its controller dynamics, also the grid impedance parameters is performed; the parameters as control gains are modified to avoid a resonance condition. The same authors use impedance modeling to describe SSCI in type 4-based WECS, where the wind farm interacting with an HVDC-based system and according to the impedance modeling, the general rule observed describes that the bandwidth of the HVDC rectifier (transmission system) must be faster than the VSC-based wind farm to ensure stability; as a result, the bandwidth of the control is modified and a voltage component is injected counter phase with the detected oscillation in order to cancel the effect [45]. A similar study is developed using impedance modeling, but the effect on the power flow is analyzed in the type 4-based WECS with HVDC-based transmission system [46]. Based on the impedance modeling and Nyquist criteria, as well as Bode plots, it is possible to identify the resonance frequencies and it is possible to establish stability boundaries. In the same context, impedance modeling is used to estimate controller parameters [47].

Another approach is based on the eigenvalue analysis which encompasses all the dynamics of the system and in combination with small-signal analysis gives an overall status of the system. The challenge of this approach is that all components of the studied system need to be modeled [38, 1].

On the other hand, the solutions for SSI are selected according the phenomenon of interest. Based on the state of the art review [24], the mitigation of SSR can be done by static-series-compensator FACTS family as GCSC, TCSC, TSSC, and SSSC. For example, [18] and [48] analyze the capabilities of Gate Turn-Off Thyristor-Controlled Series Capacitor (GTO Thyristor-Controlled Series Capacitor or GCSC) to mitigate SSR, the authors

adopt the First IEEE Benchmark Model for the analysis of SSR analysis [49]; the authors achieve to verify that the nature of operation of GCSC can mitigate SSR even without a dedicated controller, in the same way, a simple controller dedicated to SSR issues can improve the stability of the series-compensated system. In the same sense, [48] developed a comparative of two controls schemes, one based on proportional controller and other based on fuzzy controller; the results shown a better enhancement of the system by using fuzzy-based controller to mitigate SSR. As GCSC, thyristor-controlled series capacitor (TCSC), has been used through the years, e.g. recent publication as [50] published in 2020, deals with the alleviation of power systems by the use of TCSC. Similarly, the cases of study developed in [51] shows the possibilities to mitigate IGE phenomenon with TCSC, GCSC, and with a control signal implemented in the grid-side converter controller of a DFIG-based wind farm; as a result, TCSC and GCSC show high flexibility to mitigate IGE phenomenon. Same authors developed similar study, but with a fixed-speed wind turbine generator system [52]. According to the publication, the static-series-compensator FACTS family are used exclusively to solve SSR issues, there are not analysis involving this type of FACTS with SSCI issue or with SSTI. Other approaches take advantage of the DFIG-based WECS topology as the back-to-back converter, where the authors proposes a complementary damping signal to be included in the grid-side-converter controller and rotor-side-converter controller; the main advantage of this scheme is the absence of any FACTS devices [1].

SSTI in WECS is not well documented for WECS [24]. One of the first investigations were conducted with the type 1 wind turbine in 2010, as [53] where the type 1 wind turbine and a HVDC system is investigated to identify the possible interaction between these two systems; it is observed a growing torque after a transient, as a conclusion SSTI is possible in type 1 WECS and HVDC systems. In this context, [54] develop an analysis to find out the origin of subsynchronous oscillations in a WECS connected to a 800 kV HVDC system; it is concluded that the DFIG-based WECS torsional system interacts with the HVDC controllers and as a solution, a supplementary SSTI damping controller is added. Recent publications as [55] deals with the understanding of the new phenomenon known as SSTI, where the authors proposes an approach of stability analysis based on admittance model; the IGE and SSTI phenomena are characterized for a DFIG-based WECS, the proposed methodology find the frequency location of the probable interaction.

SSCI is a recent phenomenon, but in WECS is newer issues. This phenomenon is due to the interaction of the power converter of the wind farm with a series-compensated transmission line; it means that, only type 3 and type 4 WECS are prone to SSCI. There is little information regarding SSCI. One of the firsts investigations is presented in [29] where the authors deal with the interaction of type 3 WECS and series-compensated transmission line; after a fault disturbance SSCI show up and a strategy control is applied to mitigate the phenomenon. Some times this phenomenon is misunderstood, for example in 2003 [37] the authors deals with the issues of integration of large wind farms in the utility grids with two configuration, HVDC systems and series-compensated transmission line; despite

the authors indicating that the system is under a likely induction generator effect, there is not enough information to support such affirmation. In this context, in [56] the author deals with two approaches to ensure accuracy when evaluating SSCI through a proposed frequency scan. Recent publication proposes complex solution, as [57, 58] that propose fractional sliding mode control which improve the system damping modifying the control parameters of the system.

1.3 Problem Definition

Conforming to Section 1.2.3, the controller tuning of the VSC of type 3 is one of the most critical stages that can assist the system in case of a disturbance; as a result, a considerable amount of publications deals with the retuning process to improve the damping characteristic of the system under SSI issues [59]. This retuning process is based on the modal analysis techniques.

Besides, SSI problems in WECS are a new set of phenomena that need to be studied and understood in detail. In this context, it was described that even in recent publications, some authors classify SSR, SSTI, and SSCI indistinctly and encompass the definition of these terms in a distinct manner. Or, as it was described in some publications, there is not enough information to identify the phenomenon which produces SSO.

The solutions to SSI problems are focused on two main subjects, to implement a controlling stage in the grid-side converter or rotor-side converter controller to mitigate the phenomenon and the implementation of FACTS. As reported by the review of FACTS, battery energy storage systems are one of the best equipment with multiple advantages instability and power control, but in mitigation problems of SSR is barely used.

1.4 Objectives

Considering the problem definition, this Thesis is focused on the following objectives.

General Objective:

- To analyze a DFIG-based wind farm with a series compensated transmission line to improve its behavior under an SSR condition.

Particular Objectives:

- To explain in detail the model of the DFIG-based wind farm and to perform dynamic simulations.
- To propose a procedure for tuning the back-to-back converter for a DFIG-based WECS.

- To propose a procedure to identify the origin of the SSR by the discrimination of IGE, TI, or TA phenomena.
- To propose an identification process for the main modes involved in the SSR phenomenon.
- To develop a complete block diagram for the GSC and RSC controllers.
- To propose the modal impedance technique as a tool to analyze SSR problems.
- To analyze the capabilities of the BESS and to propose a control strategy to mitigate subsynchronous oscillations.

1.5   Contribution of Thesis Work

The main contribution of this Thesis is the overall analysis of the wind energy conversion system connected with a series compensated transmission line. The analysis is based on the implemented strategies to avoid a subsynchronous resonance condition.

In this context, another contribution is that a procedure to determine the origin of a subsynchronous resonance condition and the modes involved in a subsynchronous resonance condition are proposed [60].

Besides, this Thesis contributes with a complete methodology to tuning the back-to-back converter with the benefit that is focused on the WECS, which improves its stability under a subsynchronous resonance condition.

Another contribution is based on the integration and analysis of a BESS to mitigate a subsynchronous resonance condition through two approaches. The first is based on the implementation of an active power compensation control, which achieves to maintain a constant profile of active power delivered to the network. The second is based on a proposed mitigation scheme, which compensates for the subsynchronous component which produces subsynchronous resonance.

1.6   Hypothesis

It is possible to avoid the subsynchronous resonance condition of a series-compensated transmission line connected with a wind energy conversion system through the improvement of the gains of its back-to-back converter and the integration of a battery energy storage system.

1.7   List of Publications

- R. Moreno-Sánchez, C. A. Núñez-Gutiérrez, N. Visairo-Cruz, J. Hernández-Ramírez and J. Segundo-Ramírez, "Understanding the Origin of SSR in Series-Compensated DFIG-Based Wind Farms: Analysis Techniques and Tuning," in IEEE Access, vol. 9, pp. 117660-117672, 2021, doi: 10.1109/ACCESS.2021.3104171.

Chapter 2

Modeling of DFIG-based Wind Farm and Integration

2.1 Introduction

This chapter is devoted to explaining, in detail, the mathematical models involved in this Thesis, as well as to showing the performance of each model via simulation. The mathematical models are mainly simulated using the editor of MatLab, and the nonlinear differential equations are solved using the ordinary differential equations solver of MatLab. The validation is done through extensive PSCAD simulations. The mathematical models and their integration are validated, as well.

2.2 System Description

The base system of the study consists of different mathematical models and several state variables. The study system is a modified First Benchmark model for computer simulation of subsynchronous resonance [49]. The wind power system is based on type 3 wind turbines or DFIG-based wind farms. In this Thesis, the induction generator is connected radially to the series-compensated transmission line as it is shown in Figure 2.1. From the left to the right the elements shown in Figure 2.1 are:

- The wind speed, which is modeled in this Thesis.
- The blades, which represent the turbine.
- The drive train, which is represented by the two-mass model, where subscript ωt means wind turbine side and the subscript m means motor or generator side.
- The doubly-fed induction generator, with the single-cage model is implemented.
- The back-to-back converter connects the rotor side with the stator side; the average model is implemented.

- The filter and transmission line elements are modeled as their resistance, inductance, or capacitance equivalents.
- The infinite bus is represented by voltage source.

The mathematical models are explained in the following sections, and its validation is performed by a dynamic simulation.
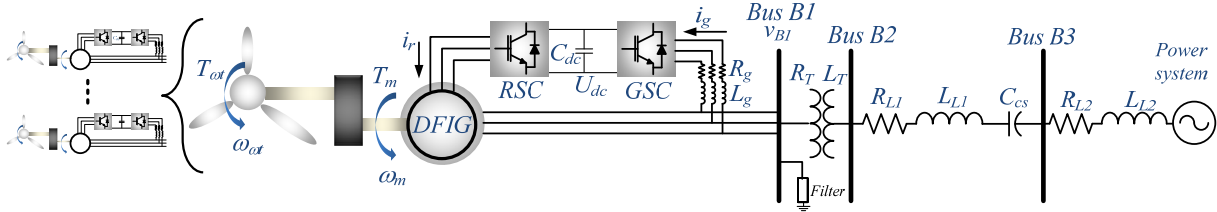
Figure 2.1: Schematic diagram of the DFIG-base wind farm.

2.2.1 Wind Speed Model

The measured wind speed approach is the most accurate model to use in simulations. However, there is not always a possibility to extract a wind speed profile. In consequence, the wind speed model approach used in this Thesis is based on [30] and encompasses the following components:

$$v_w(t) = v_{wa} + v_{wr}(t) + v_{wg}(t) + v_{wt}(t) \tag{2.1}$$

where:

- v_{wa} is the average value of the wind speed, in m/s.
- $v_{wr}(t)$ is the ramp component, in m/s.
- $v_{wg}(t)$ is the gust component, in m/s.
- $v_{wt}(t)$ is the turbulence component m/s.

The component $v_w(t)$ of (2.1) encompasses all the components above described. The wind speed shown in (2.1) can simulate a real profile of wind speed. The average value of the wind speed, v_{wa}, is equal to a constant and is usually selected as the nominal value of the wind turbine. The remaining three components are calculated as follow. The ramp component is characterized by three elements as follows:

$$\begin{aligned} t < T_{sr}, \quad &\text{for} \quad v_{wr}(t) = 0; \\ T_{sr} \le t \le T_{er}, \quad &\text{for} \quad v_{wr}(t) = \hat{A}_r \frac{t - T_{sr}}{T_{er} - T_{sr}}; \\ T_{er} < t, \quad &\text{for} \quad v_{wr}(t) = 0; \end{aligned} \tag{2.2}$$

where:

t is the time in seconds.

T_{sr} is the starting time of the wind speed ramp in seconds.

T_{er} is the end time of the wind speed ramp in seconds.

$\hat{A}_r$ is the amplitude of the wind speed ramp in m/s.

The wind speed gust is characterized by the following three elements:

$$
\begin{aligned}
t < T_{sg}, &\quad \text{for} \quad v_{wg}(t) = 0; \\
T_{sg} \le t \le T_{eg}, &\quad \text{for} \quad v_{wg}(t) = \frac{\hat{A}_g}{2}\left\{1 - cos\left[2\pi\left(\frac{t - T_{sg}}{T_{eg} - T_{sg}}\right)\right]\right\}; \\
T_{eg} < t, &\quad \text{for} \quad v_{wg}(t) = 0;
\end{aligned}
\tag{2.3}
$$

where:

T_{sg} is the starting time of the wind speed gust in seconds.

T_{eg} is the end time of the wind speed gust in seconds.

$\hat{A}_g$ is the amplitude of the wind speed gust in m/s.

The turbulence component is described according [61] as follows:

$$
v_{wt}(t) = 2\sum_{i=1}^{n}\sqrt{S_{wt}\Delta w}\,cos\,(w_i t + \phi_i), t < 0
\tag{2.4}
$$

where:

$w_i = (i - \frac{1}{2})\Delta w$.

ϕ_i is a random variable with uniform probability density on the interval 0 a 2π.

The function S_{wt} is a spectral density function defined by:

$$
S_{wt} = \frac{2K_N F^2 |w_i|}{\pi^2 \left[1 + (Fw_i/\mu\pi)^2\right]^{4/3}}
\tag{2.5}
$$

where:

K_N is the surface drag coefficient equal to 0.004.

F is the turbulence scale equal to 2000 ft.

μ is the mean speed at reference height in ft/s.

The values of $n = 50$ and $\Delta w = 0.5 - 2.0$ rad/s provides results of excellent accuracy compared against real measurements. [61].

2.2.2   Wind Turbine

The power extraction of the WECS depends on the wind availability, the following algebraic equation gives the relation between wind speed and mechanical power [30].

$$
P_{wt} = 0.5\rho A_{wt} C_p(\Lambda, \beta) v_w^3
\tag{2.6}
$$

where P_{wt} is the power extracted from the wind in watts; ρ is the air density in kg/m^2; A_{wt} is the area covered by the wind turbine in m^2; C_p is the power coefficient and represents the kinetic energy (aerodynamic of the blades) extracted from the wind (this is known as Betz's limit); Λ is the tip speed ratio ($\Lambda = \omega_{\omega t}R/v_w$), and represents the ratio between the blade tip speed (m/s) and the wind speed (m/s); β is the pitch angle, in degrees and v_w is the wind speed in m/s.

According to the turbine, the power coefficient, C_p, can be computed using the following approximation:

$$C_p(\Lambda, \beta) = c_1 \left(\frac{c_2}{\Lambda_i} - c_3\beta - c_4\beta^{c_5} - c_6 \right) exp \left(\frac{-c_7}{\Lambda_i} \right) \tag{2.7}$$

where

$$\Lambda_i = \left[\frac{1}{\Lambda + c_8\beta} - \frac{c_9}{\beta^3 + 1} \right]^{-1} \tag{2.8}$$

Equations (2.7) and (2.8) represent the structure of the wind turbine (WT), i.e., the output-power curve of the turbine is computed by a numerical approximation. The constants c_1 to c_9 are used to determine the type of the WT. The values for the constants are shown in Table 2.1 [30].

Table 2.1: Approximation of power curves.

Turbine	c_1	c_2	c_3	c_4	c_5	c_6	c_7	c_8	c_9
Heier (1989)	0.5	116	0.4	0	–	5	21	0.08	0.035
Constant-speed wind turbine	0.44	125	0	0	0	6.94	16.5	0	-0.002
Variable-speed wind turbine	0.73	151	0.58	0.002	2.14	13.2	18.4	-0.02	-0.003

Other approximation of the power coefficient can be found in the literature, but according the manufacturers, those curves are very similar, so it is not necessary to use different approximation for constant-speed or variable-speed wind turbine [30].

2.2.3 Drive Train

The model of the drive train for WECS is very important due to the correct representation of their behavior during and after voltage drops, short circuits analysis is essential for its assessment. This is because of the low-speed shaft of the wind turbines is relatively softer than the typical steam turbine shaft in conventional power plants. It is well documented that the two-mass model can represent properly the behavior of the drive train system for WECS. The dynamic equations are expressed as follows:

$$\frac{d\omega_g}{dt} = \frac{1}{2H_g}\left(T_m - F\omega_g - T_e\right) \tag{2.9}$$

$$\frac{d\gamma}{dt} = \omega_{mb}\left(\omega_{wt} - \omega_g\right) \tag{2.10}$$

$$\frac{d\omega_{wt}}{dt} = \frac{1}{2H_{wt}}\left(T_{wt} - T_m\right) \tag{2.11}$$

where ω_g and ω_{wt} are the generator and wind turbine mechanical speeds, respectively, in *pu* while ω_{mb} is the base-mechanical frequency in hertz; H_g and H_{wt} are the inertia constants of the generator and wind turbine, respectively, in *s*; γ is the angular displacement between the two ends of the shaft, in degrees; T_e is the electrical torque while T_m is the shaft torque, and T_{wt} is the wind turbine torque in *pu*, which are defined as follows:

$$T_e = L_m(i_{ds}i_{qr} - i_{qs}i_{dr}) \tag{2.12}$$

$$T_m = K_{tg}\gamma + D_{sh}\omega_{mb}(\omega_{wt} - \omega_g) \tag{2.13}$$

$$T_{wt} = P_{wt}/\omega_{wt} \tag{2.14}$$

where L_m is the mutual inductance, the term i represents the induction generator currents explained in the next subsection, K_{tg} is the shaft stiffness constant, D_{sh} is the mutual damping and F is the friction factor or mechanical damping; all in *pu*.

2.2.4 Squirrel Cage Induction Generator

The nonlinear differential equations of the squirrel cage induction generator can be described by its flux linkages [30] or by its currents [62]. In this Thesis, the dynamic model of the SCIG is obtained from its currents equation in the arbitrary reference frame [63]. The set of differential equations of the stator and rotor circuits, with stator and rotor currents as state variables can be given in a $d-q$ reference frame rotating at synchronous speed are described as follow:

$$\frac{1}{\omega_b}\begin{bmatrix}\dfrac{di_{qs}}{dt}\\[2mm]\dfrac{di_{ds}}{dt}\\[2mm]\dfrac{di_{qr}}{dt}\\[2mm]\dfrac{di_{dr}}{dt}\end{bmatrix} = \begin{bmatrix}L_s & 0 & L_m & 0\\0 & L_s & 0 & L_m\\L_m & 0 & L_r & 0\\0 & L_m & 0 & L_r\end{bmatrix}^{-1}\begin{bmatrix}v_{qs} - R_s i_{qs} - \omega_s\psi_{ds}\\v_{ds} - R_s i_{ds} + \omega_s\psi_{qs}\\v_{qr} - R_r i_{qr} - (\omega_s - \omega_r)\psi_{dr}\\v_{dr} - R_r i_{dr} + (\omega_s - \omega_r)\psi_{qr}\end{bmatrix} \tag{2.15}$$

where ω_s is the rotatory reference frame or stator-voltage speed, ω_b is the base speed, both in *rad/s*, v is the stator or rotor voltage, i is the stator or rotor currents, R is the stator or rotor resistance, ψ is the stator or rotor flux, the subscripts s and r represent the

stator and rotor respectively, ω_r is the electrical rotor speed, the direct and quadrature axis expressed with d and q. The inductance matrix with $L_s = L_{ls} + L_m$ and $L_r = L_{lr} + L_m$, where L_m is the mutual inductance, L_{lr} and L_{ls} are the rotor and stator leakage inductance, respectively. Except where is indicated, all in *pu*

2.2.5   Pitch Control

The pitch angle controller is focused on the control of the aerodynamic efficiency of the wind turbine (mechanical power). The PAC is activated only when the wind speed is higher than the nominal speed of the turbine. When the wind speed is higher than the turbine rated speed, the maximum power point tracking algorithm is required. The pitch angle, β, is set according the reference mechanical power. In this sense, the servo is modeled as follows:

$$\frac{d\beta}{dt} = \frac{1}{T_\beta}(\beta_{ref} - \beta) \tag{2.16}$$

where T_β is the time constant of the pitch servo, β_{ref} is the reference angle, and β is the angle of the blades. The maximum rate of change of the pitch angle is in the order of 3–10 degrees per second, depending on the size of the wind turbine. The pitch angle β_{ref} is kept zero when the wind speed is below to the rated value, otherwise, a PI control is applied to get the pitch angle β_{ref}.

$$\beta_{ref} = K_{P\beta}(P_{wt} - P_{ref}) + x_\beta \tag{2.17}$$
$$\dot{x}_\beta = K_{I\beta}(P_{wt} - P_{ref})$$

where $K_{P\beta}$ is the proportional gain for the pitch angle control, P_{wt} is the mechanical power extracted from the blades, P_{ref} is the reference power, $K_{P\beta}$ is the integral gain for the pitch angle control, x_β and $\dot{x}_\beta$ are auxiliary equations.

2.2.6   DC-link Capacitor

The DC-link of the back-to-back converter from the DFIG is modeled conforming to the Figure 2.2.
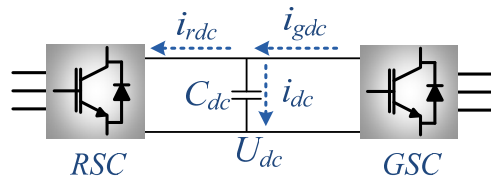
Figure 2.2: Schematic of the DC bus of the back-to-back converter

Accordingly, the equation which describes the energy balance of the DC-link capacitor

is expressed as follows:

$$\frac{C_{dc}}{\omega_b}\frac{dU_{dc}}{dt} = i_{dc} \tag{2.18}$$

where U_{dc} is the DC-link voltage, the current through out the capacitor is $i_{dc} = i_{gdc} - i_{rdc}$, where i_{gdc} is the DC current from the GSC and i_{rdc} is the DC current from de RSC.

2.2.7 Voltage-Source Converter

The VSC modeling procedure is based on the average model described in [64]. The GSC, shown in Figure 2.3, is used as study case, where the electric circuit for the VSC is depicted.
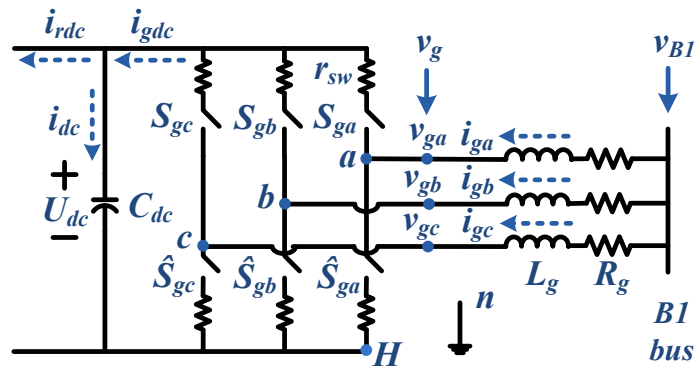
Figure 2.3: Electric circuit for the GSC.

The three branches are indicated by its corresponding phase, a, b and c; the voltages v_{gx} (with $x = a, b, c$ and g indicating GSC state variables) are expressed in phase-ground values, and the currents i_{gx} are the values per phase. r_{sw} is the switch on-state resistance and includes conduction losses. The bidirectional switching functions are identified by S_{gx} and $\hat{S}_{gx}$ which can be either on or off (1 or 0, states of the switch). Based upon the VSC operation principle, S_x and $\hat{S}_x$ are complementary, i.e.

$$S_{gx} + \hat{S}_{gx} = 1 \tag{2.19}$$

Thus, it is required an expression relating the abc voltages to the DC-link voltage. For each phase ($x = a, b, c$) the next expression is valid at any time:

$$v_{gx} = v_{xH} + v_{Hn} \tag{2.20}$$

when S_{gx} is on, $S_{gx} = 1$ and $\hat{S}_{gx} = 0$, then:

$$v_{xH} = r_{sw}i_{gx} + U_{dc} \tag{2.21}$$

when S_{gx} is off, $S_{gx} = 0$ and $\hat{S}_{gx} = 1$, then:

$$v_{xH} = r_{sw}i_{gx} \tag{2.22}$$

In general, an expression which defines the voltages v_{xH} is:

$$v_{xH} = r_{sw}i_{gx} + U_{dc}S_{gx} \tag{2.23}$$

Considering a balanced system, $v_{ga} + v_{gb} + v_{gc} = 0$, and substituting (2.23) for each phase into (2.20), the expression for v_{Hn} is obtained:

$$v_{Hn} = \frac{-U_{dc}(S_{ga} + S_{gb} + S_{gc})}{3} \tag{2.24}$$

Substituting Equations (2.23) and (2.24) into (2.20) and making some algebraic manipulation, the expression for phase a which links the abc voltages with DC-link voltage is:

$$v_{ga} = i_{ga}r_{sw} + U_{dc}\left(S_{ga} - \frac{1}{3}\sum_{x=a,b,c} S_{gx}\right) \tag{2.25}$$

The expressions for b and c phases are similar as (2.25). Now, for two-level PWM scheme, the switching function S_{gx} can be defined according the Figure 2.4.
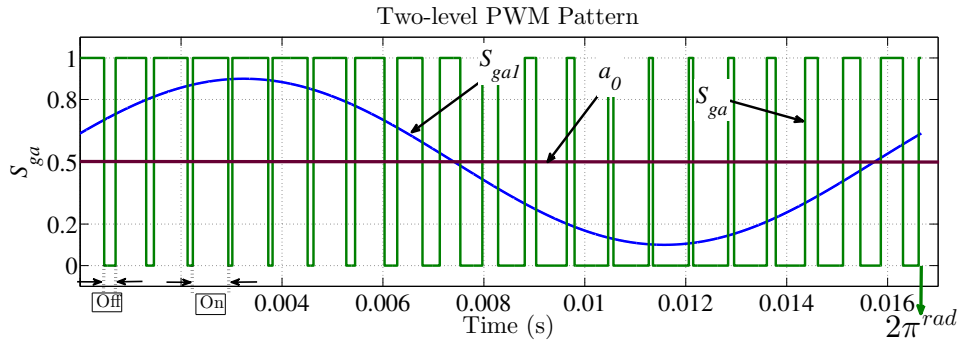
Figure 2.4: Phase a of the GSC.

Figure 2.4 shows a generalized PWM pattern for S_{ga}. The generalized patterns for b and c phases are identical but with its appropriated phase shift. Since the switching function S_{ga} is a periodic function of time, Fourier Series theory can be used to describe S_{ga}. S_{ga1} is the fundamental component and a_0 is the mean value of S_{ga}. Due to the interest is obtain the average VSC model, it is required a mathematical expression for S_{ga1}, conforming to Figure 2.4 the expression is

$$S_{ga1} = \frac{m_{Ag}}{2}cos(\omega t - \delta_{Eg}) + \frac{1}{2} \tag{2.26}$$

S_{gb1} and S_{gc1} for b and c phases are identical but with appropriated phase shift.

The control signals are m_{Ag}, δ_{Eg}, and ω are the modulation index, phase-angle, and the frequency, respectively. Then, for phase a the mathematical model which governs the behavior of the voltage at the VSC terminal can be found substituting S_{ga1}, S_{gb1} and S_{gc1} into (2.25), for the average model $S_{gx} \rightarrow S_{gx1}$:

$$v_{ga} = i_{ga}r_{sw} + U_{dc}\frac{m_{Ag}}{2}cos(\omega t - \delta_{Eg}) \tag{2.27}$$

Similar expressions of (2.27) for b and c phases are also deduced. For the average model, the GSC DC-current is:

$$i_{gdc} = i_{ga}S_{gb1} + i_{gb}S_{gb1} + i_{gc}S_{gc1} \tag{2.28}$$

Similar analysis gives similar equation for RSC.

2.2.8 Grid-Side-Converter Controller

The GSCC [62] is usually controlled by a vector-control scheme oriented along the stator voltage [34, 62]. Typical PI controllers are used for regulating the DC-link voltage and reactive power; the reactive power control through GSC is out of the scope of this Thesis, then $i^{\varepsilon}_{qg\_ref} = 0$. The superscript ε in Figure 2.5 denotes the orientation of reference frame. The stator-voltage oriented reference frame allows the independent control of active and reactive power flowing from the stator side through the GSC to the DC-link.

Figure 2.5: Schematic of the grid-side-converter controller.

Conforming to Figure 2.3, the voltage balance across the inductance branches is:

$$v_{B1} = v_g + R_g i_g + \frac{L_g}{\omega_b}\frac{di_g}{dt} \tag{2.29}$$

where R_g and L_g are the GSC resistance and inductance, respectively. Using the Park theory [65], Equation (2.29) is transformed into dq stator-voltage oriented reference frame

as follows:

$$\frac{L_g}{\omega_b}\frac{d}{dt}\begin{bmatrix} i^\varepsilon_{dg} \\ i^\varepsilon_{qg} \end{bmatrix} = \begin{bmatrix} v^\varepsilon_{dB1} \\ v^\varepsilon_{qB1} \end{bmatrix} - \begin{bmatrix} v^\varepsilon_{dg} \\ v^\varepsilon_{qg} \end{bmatrix} - R_g\begin{bmatrix} i^\varepsilon_{dg} \\ i^\varepsilon_{qg} \end{bmatrix} - \omega_s L_g\begin{bmatrix} -i^\varepsilon_{qg} \\ +i^\varepsilon_{dg} \end{bmatrix} \tag{2.30}$$

Equation (2.30) has coupled terms, to eliminate the coupled terms an equation can be synthesized by inspection and using the stator-voltage oriented reference frame, the reference voltages with compensation terms described in *dq* frame are:

$$\begin{bmatrix} v^{\varepsilon*}_{dg} \\ v^{\varepsilon*}_{qg} \end{bmatrix} = \begin{bmatrix} v^\varepsilon_{dB1} \\ v^\varepsilon_{qB1} \end{bmatrix} + \omega_s L_g\begin{bmatrix} +i^\varepsilon_{qg} \\ -i^\varepsilon_{dg} \end{bmatrix} - \begin{bmatrix} v^{\varepsilon\prime}_{dg} \\ v^{\varepsilon\prime}_{qg} \end{bmatrix} \tag{2.31}$$

where the voltages $v^{\varepsilon*}_{dg}$ and $v^{\varepsilon*}_{qg}$ are the reference voltage and $v^{\varepsilon\prime}_{dg}$ and $v^{\varepsilon\prime}_{qg}$ are the control signals. In accordance with the control scheme depicted in Figure 2.5, the equations with respect to the GSCC are described as follows:

$$\begin{aligned} i^\varepsilon_{dg\_ref} &= K_{Pudc}(U_{dc\_ref} - U_{dc}) + x_{udc} \\ \dot{x}_{udc} &= K_{Iudc}(U_{dc\_ref} - U_{dc}) \\ v^{\varepsilon\prime}_{dg} &= K_{Pidg}(i^\varepsilon_{dg\_ref} - i^\varepsilon_{dg}) + x_{idg} \\ \dot{x}_{idg} &= K_{Iidg}(i^\varepsilon_{dg\_ref} - i^\varepsilon_{dg}) \end{aligned} \tag{2.32}$$

The equations for $q - axis$ are:

$$\begin{aligned} v^{\varepsilon\prime}_{qg} &= K_{Pidg}(i^\varepsilon_{qg\_ref} - i^\varepsilon_{qg}) + x_{iqg} \\ \dot{x}_{iqg} &= K_{Iidg}(i^\varepsilon_{qg\_ref} - i^\varepsilon_{qg}) \end{aligned} \tag{2.33}$$

The stator-voltage oriented reference frame can be calculated by means the stator voltages as $\theta^\varepsilon = atan2(v_{qs}/v_{ds})$. Alternatively, θ^ε can be calculated by a system based on a phase-locked loop connected in bus B1 [34], described in Section 2.2.10.

2.2.9   Rotor-Side-Converter Controller

The RSCC [62] is usually controlled by stator-flux oriented reference frame [34, 62, 66]. The stator-flux vector control allows decoupling the electromagnetic torque and the rotor excitation current. Figure 2.6 shows the RSCC, the superscript φ denotes the variable reference frame. The typical PI controllers are used for regulation in both, rotor speed and stator voltage.

The voltage across de rotor circuit can be defined making some mathematical development of the induction model shown in (2.15). In this sense, the dynamic behavior of the rotor currents can be described as:

$$\frac{di_{dr}}{dt} = -\omega_b(v_{ds} - R_s i_{ds} + \omega_f \psi_{qs})L_m/L_r L_s \alpha + (v_{dr} - R_r i_{dr} + \omega_{slip}\psi_{qr})/L_r \alpha \tag{2.34}$$

Figure 2.6: Schematic rotor-side-converter control

$$\frac{di_{qr}}{dt} = -\omega_b(v_{qs} - R_s i_{qs} - \omega_f \psi_{ds})L_m/L_r L_s \alpha + (v_{qr} - R_r i_{qr} - \omega_{slip}\psi_{dr})/L_r \alpha \qquad (2.35)$$

in steady state $v_{qs} = R_s i_{qs} + \omega_f \psi_{ds}$ and $v_{ds} = R_s i_{ds} - \omega_f \psi_{qs}$ [65]. Making some algebraic manipulations with the Equations (2.34) and (2.35), the voltage balance across the RSC and the rotor circuit of the SCIG in the stator-flux oriented reference frame is:

$$\frac{\alpha L_r}{\omega_b}\frac{d}{dt}\begin{bmatrix} i_{dr}^{\varphi} \\ i_{qr}^{\phi} \end{bmatrix} = \begin{bmatrix} v_{dr}^{\varphi} \\ v_{qr}^{\varphi} \end{bmatrix} - R_r\begin{bmatrix} i_{dr}^{\varphi} \\ i_{qr}^{\varphi} \end{bmatrix} - \omega_{slip}\begin{bmatrix} -\psi_{qr}^{\varphi} \\ \psi_{dr}^{\varphi} \end{bmatrix} \qquad (2.36)$$

where $\omega_{slip} = \omega_s - \omega_r$ and $\alpha = 1 - L_m^2/L_r L_s$. Due to the stator-flux orientation the next terms can be written as [66], $\psi_{dr}^{\varphi} = \frac{L_m}{L_s}\Psi_s + \alpha L_r i_{dr}^{\varphi}$, $\psi_{qr}^{\varphi} = \alpha L_r i_{qr}^{\varphi}$, and $T_e = -\frac{L_m}{L_s}\Psi_s i_{qr}^{\varphi}$.

Equation (2.36) has coupled terms, to eliminate the coupled terms an equation can be synthesized by inspection and considering the stator-flux oriented reference frame, the reference voltages with compensation terms described in *dq* frame are:

$$\begin{bmatrix} v_{dr}^{\varphi*} \\ v_{qr}^{\varphi*} \end{bmatrix} = \omega_{slip}\begin{bmatrix} -\psi_{qr}^{\varphi} \\ \psi_{dr}^{\varphi} \end{bmatrix} + \begin{bmatrix} v_{dr}^{\varphi\prime} \\ v_{qr}^{\varphi\prime} \end{bmatrix} \qquad (2.37)$$

where the voltages $v_{dr}^{\varphi*}$ and $v_{qr}^{\varphi*}$ are the rotor reference voltage, $v_{dr}^{\varphi\prime}$ and $v_{qr}^{\varphi\prime}$ are the control signals. In accordance with the control scheme shown in Figure 2.6, the equations with respect to the RSCC are described as follows:

$$\begin{aligned}
i_{dr\_ref}^{\varphi} &= K_{Pus}(U_{s\_ref} - U_s) + x_{us} \\
\dot{x}_{us} &= K_{Ius}(U_{s\_ref} - U_s) \\
v_{dr}^{\varphi\prime} &= K_{Pidr}(i_{dr\_ref}^{\varphi} - i_{dr}^{\varphi}) + x_{idr} \\
\dot{x}_{idr} &= K_{Iidr}(i_{dr\_ref}^{\varphi} - i_{dr}^{\varphi})
\end{aligned} \qquad (2.38)$$

The equations for $q - axis$ are:

$$
\begin{aligned}
i^{\varphi}_{qr\_ref} &= \frac{-L_s}{L_m \Psi_s} \left(K_{P\omega}(\omega_{ref} - \omega_r) + x_\omega \right) \\
\dot{x}_\omega &= K_{I\omega}(\omega_{ref} - \omega_r) \\
v^{\varphi\prime}_{qr} &= Kp_{iqr} \left(i^{\varphi}_{qr\_ref} - i^{\varphi}_{qr} \right) + x_{iqr} \\
\dot{x}_{iqr} &= K_{Iiqr} \left(i^{\varphi}_{qr\_ref} - i^{\varphi}_{qr} \right)
\end{aligned}
\tag{2.39}
$$

The stator-flux oriented reference frame angle is calculated with the system configuration, i.e., if the infinite bus is assumed at stator terminals the calculation of the angle θ^φ can be simplified [1, 34, 62, 66]. For the correct decoupling, in this Thesis the reference frame angle is calculated using the stator flux convention $\theta_{ph} = atan(\psi_{qs}/\psi_{ds})$ then the reference frame angle is calculated as:

$$
\theta^\varphi = \theta_{ph} - \theta_r
\tag{2.40}
$$

where θ_r is the rotor electrical angle of the induction machine. In some cases, a filter is applied to implement Equation (2.40) avoiding the drift produced by low-frequency components in the stator voltage and current [34].

2.2.10 Phase-Locked Loop

The PLL is modeled for a three phase system [67]. The PLL tracks the frequency and phase for a sinusoidal three-phase signal by using an internal oscillator. The simplified scheme of the PLL used to calculate θ^ε is shown in Figure 2.7.
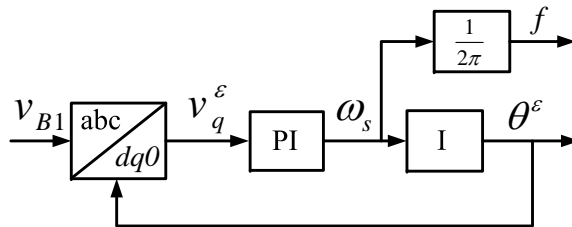
Figure 2.7: Simplified scheme of the phase-locked loop.

The three phase signal is converted to a $dq0$ rotating frame, the quadrature axis of the transformation is used as reference. A PID or PI controller can be used to keep the phase difference to 0 by acting on a controller oscillator. In general, the output of the PI controller corresponds to the angular velocity, if it is required this signal is filtered, then this signal can be converted on the frequency in Hz, finally the phase can be calculated by a integral controller, as shown in Figure 2.7.

The angular frequency can be computed by:

$$\omega_s = K_{Ppll}v_q^\varepsilon + \int K_{Ipll2}v_q^\varepsilon dt \tag{2.41}$$

Making $\omega_I = \int K_{Ipll2}v_q^\varepsilon dt$, an expression for the angular velocity on bus B1 is synthesized as follows:

$$\omega_s = K_{Ppll}v_q^\varepsilon + \omega_I \tag{2.42}$$

Conforming to Figure 2.7, the auxiliary angular frequency can be computed by:

$$\frac{d\omega_I}{dt} = K_{Ipll2}v_q^\varepsilon \tag{2.43}$$

Finally, the phase is computed by:

$$\frac{d\theta^\varepsilon}{dt} = K_{Ipll}\omega_s \tag{2.44}$$

The proportional and integral gains are set in this Thesis as $K_{Ppll} = 180$, $K_{Ipll2} = 3200$, and $K_{Ipll} = 1$. Due to θ^ε increase proportionally with time, in some occasions a change-of-variable technique is required.

2.2.11   Battery Energy Storage System

The BESS is modeled as an equivalent circuit developed by analyzing experimental test data [68, 69, 70], and this equivalent circuit is used frequently to study systems based on batteries integrated to a power system [71, 72, 73, 74, 75, 76]. The BESS is controlled by the well-known control scheme reported in several publications as [75, 76, 77, 78]; where the task of the control is meanly focused on compensate or adsorb intermittent energy from renewable sources connected to a microgrid or a power system. Figure 2.8 shows the schematic of the BESS.
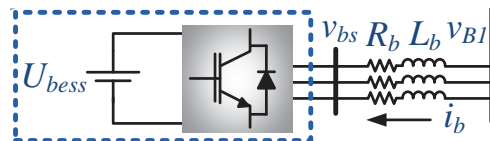
Figure 2.8: The schematic of the VSC and the BESS.

Figure 2.9 shows the equivalent circuit of the battery. The BESS scheme control is shown in Figure 2.10. The control law and the equations for BESS are obtained developing the same procedure described at Section 2.2.8, as it is described as follows.

The voltage balance across the BESS can be described based on Figure 2.8, the voltage
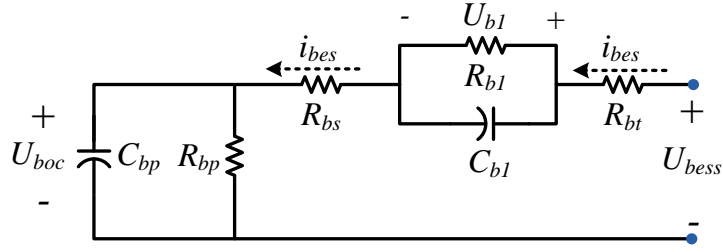
Figure 2.9: Equivalent circuit of the battery.

balance across the inductance is:

$$v_{B1} = v_{bs} + R_b i_b + \frac{L_b}{\omega_b} \frac{di_b}{dt} \tag{2.45}$$

where R_b and L_b are the BESS resistance and inductance, respectively. Using the Park theory [65], Equation (2.45) is transformed into dq synchronously-oriented reference frame as follows:

$$\frac{L_b}{\omega_b} \frac{d}{dt} \begin{bmatrix} i_{db} \\ i_{qb} \end{bmatrix} = \begin{bmatrix} v_{dB1} \\ v_{qB1} \end{bmatrix} - \begin{bmatrix} v_{db} \\ v_{qb} \end{bmatrix} - R_b \begin{bmatrix} i_{db} \\ i_{qb} \end{bmatrix} - \omega_b L_b \begin{bmatrix} -i_{qb} \\ +i_{db} \end{bmatrix} \tag{2.46}$$

Equation (2.46) has coupled terms, as the previous cases for the GSC and RSC an equation can be synthesized, considering the synchronously-oriented reference frame, the reference voltages with compensation terms described in dq frame are:

$$\begin{bmatrix} v_{db}^* \\ v_{qb}^* \end{bmatrix} = \begin{bmatrix} v_{dB1} \\ v_{qB1} \end{bmatrix} + \omega_b L_b \begin{bmatrix} +i_{qb} \\ -i_{db} \end{bmatrix} - \begin{bmatrix} v_{db}' \\ v_{qb}' \end{bmatrix} \tag{2.47}$$

where the voltages v_{db}^* and v_{qb}^* are the reference voltage and v_{db}' and v_{qb}' are the control signals. In accordance with the control scheme shown in Figure 2.10, the equations with respect to the BESS are described as follows:

$$
\begin{aligned}
i_{db\_ref} &= K_{Pp}(P_{ref} - P_{bess} - P_{dfig}) + x_{Pbs} \\
\dot{x}_{Pbs} &= K_{Ip}(P_{ref} - P_{bess} - P_{dfig}) \\
v_{db}' &= K_{Pidb}(i_{db\_ref} - i_{db}) + x_{idb} \\
\dot{x}_{idb} &= K_{Iidb}(i_{db\_ref} - i_{db})
\end{aligned}
\tag{2.48}
$$

The equations for $q - axis$ are:

$$
\begin{aligned}
i_{dq\_ref} &= K_{Pq}(Q_{ref} - Q_{bess} - Q_{dfig}) + x_{Pqs} \\
\dot{x}_{Pqs} &= K_{Iq}(Q_{ref} - Q_{bess} - Q_{dfig}) \\
v'_{qb} &= K_{Piqb}(i_{qb\_ref} - i_{qb}) + x_{iqb} \\
\dot{x}_{iqb} &= K_{Iiqb}(i_{qb\_ref} - i_{qb})
\end{aligned}
\tag{2.49}
$$

The synchronously-oriented reference frame is adopted for this model, in this model the pu system is adopted, as well.
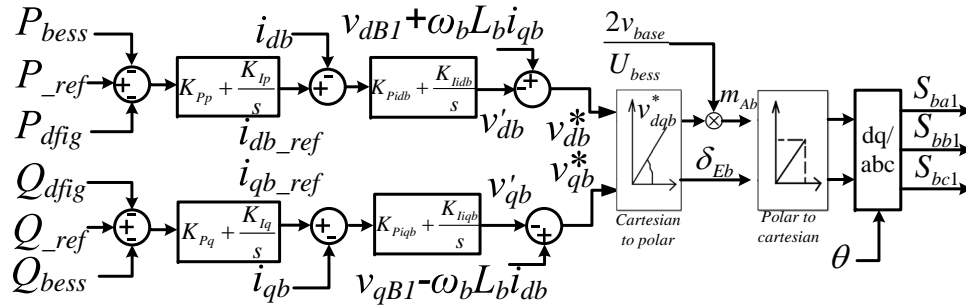
Figure 2.10: BESS scheme control.

2.2.12   Transmission Line

The transmission line is modeled using the series impedance model, shown in Figure 2.1. The differential equations are written in pu and dq system with synchronously-oriented reference frame as follows:

$$
\frac{di_{dB1}}{dt} = \omega_b(v_{dso} - v_{dB1} - v_{dcs} - R_{tot}i_{dB1} + \omega_b L_{tot}i_{qB1})/L_{tot}
\tag{2.50}
$$

$$
\frac{di_{qB1}}{dt} = \omega_b(v_{qso} - v_{qB1} - v_{qcs} - R_{tot}i_{qB1} - \omega_b L_{tot}i_{dB1})/L_{tot}
\tag{2.51}
$$

where v_{dso} and v_{qso} are the dq voltages of the power system; v_{dcs} and v_{qcs} are the voltages of the series compensation of the transmission line; i_{dB1} and i_{qB1} are the currents of the transmission line; $R_{tot} = R_T + R_{L1} + R_{L2}$ is the total resistance of the transmission line and $L_{tot} = L_T + L_{L1} + L_{L2}$ is the total inductance of the transmission line.

2.2.13   Series Compensation

The series compensation is modeled as a capacitor in pu in dq with synchronously-oriented reference frame as follows:

$$\frac{dv_{dcs}}{dt} = \omega_b(i_{dB1} + \omega_b C_{cs} v_{qcs})/C_{cs} \tag{2.52}$$

$$\frac{dv_{qcs}}{dt} = \omega_b(i_{qB1} - \omega_b C_{cs} v_{dcs})/C_{cs} \tag{2.53}$$

where C_{cs} is the series capacitance.

2.3 Dynamic Simulation and Validation of the Complete System

The entire system shown in Figure 2.1 is simulated in ODES of MatLab. There are several reasons which justify the use of ODES for simulating. In this sense, the advantages to simulate a system using ODES are described following:

- The simulation time required to simulate in ODES is less than the same system in Simulink.
- The parameters can be modified easily and there is access to all the state variables.
- The linearization of the system can be done easily numerically.
- The ODES can be selected according the requirements of the system, i.e., the time step is selected small or large according to the system requirements.

In this context, the disadvantage to simulate a system in ODES can be summarized as follows:

- I t is required programming skills and knowledge of the MatLab environment.
- The system requires to establish a initial condition coherent to physical scenario (real scenario).

The entire system simulated in this Thesis is a modified scheme of the First Benchmark for Computer Simulation of SSR [49]. The system shown in Figure 2.1 is simulated in ODES and PSCAD, the validation is done through the comparison of the state variables in different scenarios.

First, the system under study is simulated with the following asumptions:

- All the dynamic equations are simulated in *pu* system.
- The wind speed is set as constant.
- The GSCC and RSCC are disable at the starting condition of the simulation.
- To avoid extra control effort, the controllers of the controlled variables are activated sequentially, i.e., the DC-link voltage is activated first, then the stator voltage is activated, and finally the rotor speed controller is activated.
- The initial rotor-speed of the turbine side and generator side is equal to 1 *pu*.
- The initial condition of the dc-link voltage is equal to 1 *pu*.

- The entire system is modeled in **dq** reference frame.
- The average model of the VSCs is used.

The initial conditions of the state variables are set as shown in Section C.1. After a second that the simulation starts, the rotor speed and the stator terminal voltage controllers are activated. This transient, produced by the integration of the controller, is used to validate the system. The following figures depict the main state variables from the simulation of the ODES and PSCAD.

Figures 2.11 and 2.12 show the stator and rotor currents of the induction generator. Figure 2.13 shows the mechanical rotor speed of the induction generator. Figure 2.14 shows the dc voltage in the DC-link of the back-to-back converter. Figure 2.15 shows the rms voltage from the bus B1. The figures show that the evolution of the states variables of ODES and PSCAD almost overlap each other. It can be concluded that the ODES and PSCAD systems behave similarly, then the system shown in Figure 2.1 modeled in ODES of MatLab is valid to develop the studies shown below.
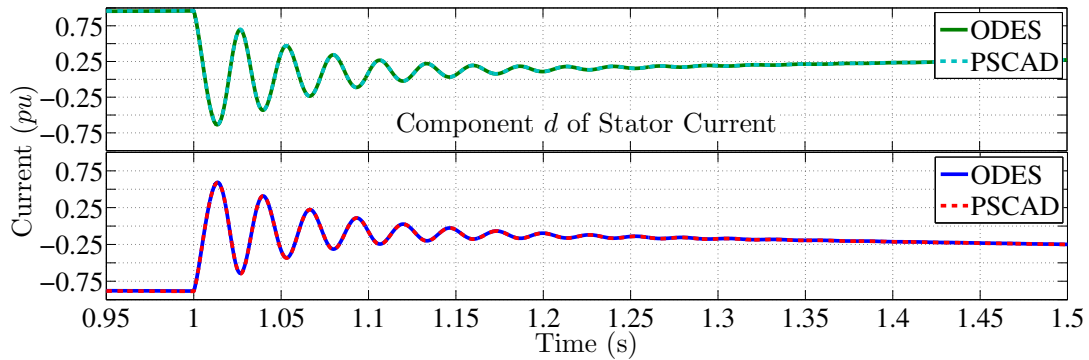
Figure 2.11: Induction generator component *d* of the stator and rotor currents.
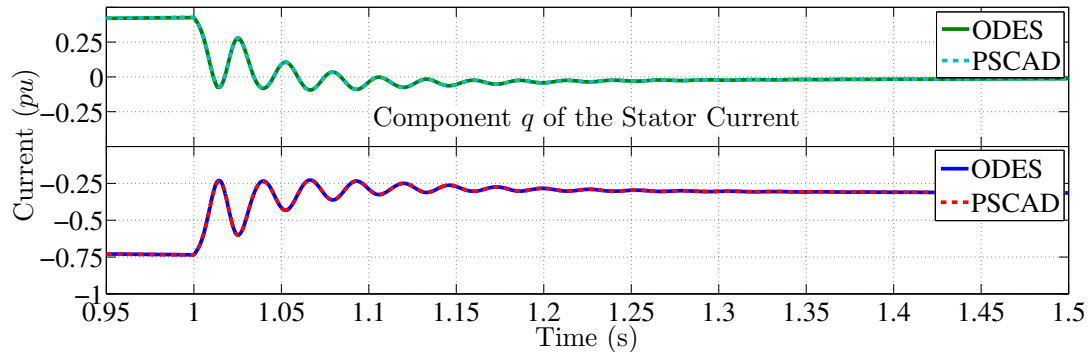
Figure 2.12: Induction generator component *q* of the stator and rotor currents.
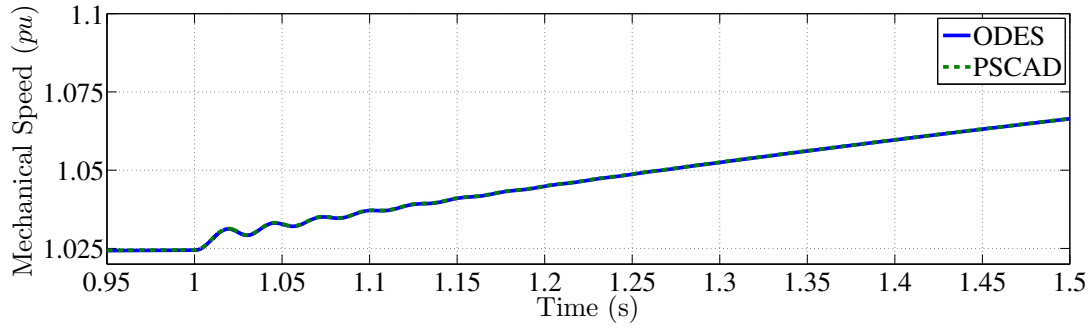
Figure 2.13: Induction generator mechanical rotor speed in *pu*.
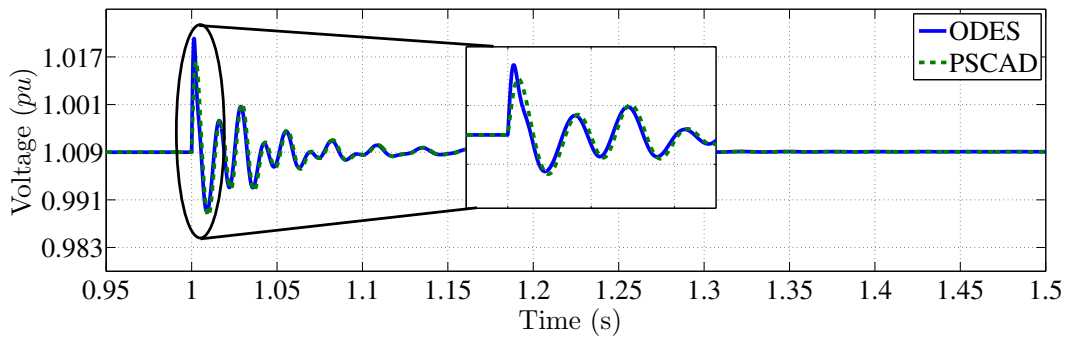
Figure 2.14: Back-to-back converter DC-link voltage.
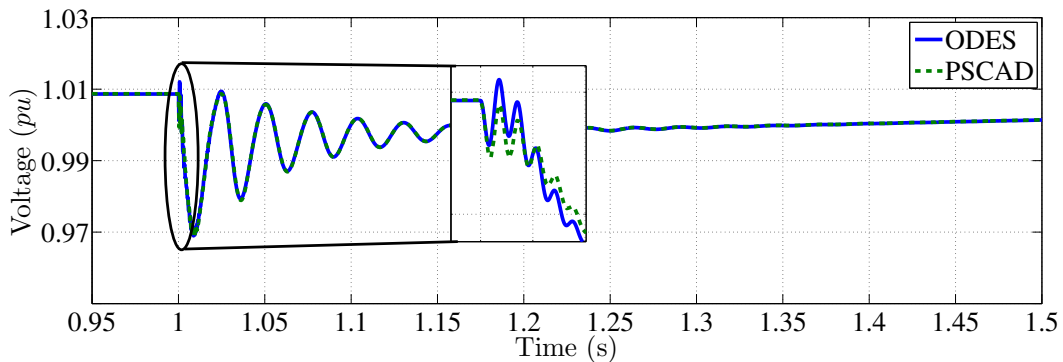
Figure 2.15: Root-mean-square voltage of the bus B1 in *pu*, positive sequence.

2.4   Chapter Discussion

This chapter presents the background of the mathematical models used in the study of SSR in WECS-based wind farms. In this context, the dynamic equations, state variables, base values, and a detailed explanation of each model were given. The mathematical models are expressed in *per unit* system, this convention is the best solution for simulation in ODES to avoid issues related to the difference between magnitudes of the several units.

The mathematical models related to the electrical system are simulated in its *dq* frame, its models in *abc* frame can be used, but the *dq* convention converges to a constant in steady-state, which is required for the analysis developed in the following sections.

All simulations displayed in this Thesis are processed through MatLab due to its availability of all state variables and the function to compute the eigenvalue analysis. PSCAD is mainly used to validate the ODES.

Chapter 3

Tuning and Analysis Techniques for SSR in DFIG-based Wind Farm

3.1 Introduction

In this chapter, it is proposed a methodology for tuning GSCC and the RSCC. Besides, three analysis techniques are implemented to characterize the subsynchronous resonance in a DFIG-based wind farm; the advantages and disadvantages are highlighted. Finally, a discrimination procedure and identification procedure are developed to determine the source of the SSR.

3.2 Background of Tuning Methods

The new installation of WECS, as reported by [31, 34], is toward VSC-based technologies as type 3 or type 4 wind farms. In this respect, the controllers are an essential part of the proper operation of the wind farms. It is difficult to find in the state of the art a recommended methodology for tuning controls of a back-to-back converter based on DFIG-systems; it is common to report the gains used in a previous publication, however with a change of the reported topology, the controls tend to fail. This section is focused on the tuning methods that can be applied to the back-to-back converter of DFIG systems.

The back-to-back converter controllers consist of the following elements: two controllers (shown in Figures 2.5 and 2.6), each one with two stages in *dq* reference frame: inner current controller (inner loop) and outer controller (outer loop). In this section, the tuning process is described for each loop and several methodologies are explained to select the suitable technique to be used according the WECS.

The two general blocks diagram for inner and outer loops are shown in Figure 3.1 and 3.2, respectively. Where I represents the current to be controlled and x is the state variable to be controlled. The components in the inner current controller are: PI controller, time

39

delay from the PWM converter, and the system. The components in the outer controller are: PI controller, the simplified transfer function of the closed-loop current controller, and the system, in this case, it is described by the state variables to be controlled (DC-link voltage, rotor speed, or stator voltage).
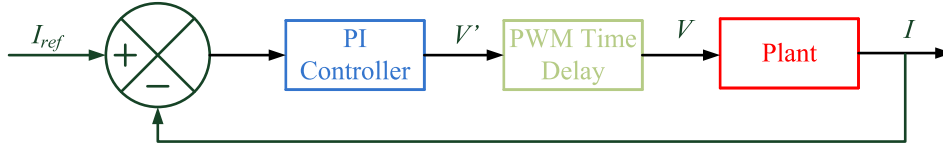
Figure 3.1: General block diagram for the inner current controller.
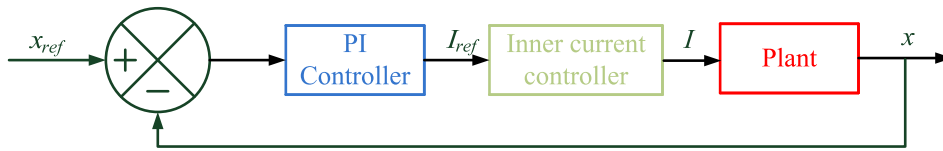
Figure 3.2: General block diagram for the outer controller.

A complete tuning procedure for the back-to-back converter is provided in this chapter. The controller tuning methods for VSC-HVDC systems [79], as well other methods are proposed to be used in VSC of DFIG-based wind farms.

3.3 Tuning of Grid-Side-Converter Controller

The aim of the GSCC topology is to control the DC-link voltage through the d component. The q component for reactive power control is disabled (i.e., $i^{\varepsilon}_{qg\_ref} = 0$). In this sense, Figure 3.3 shows a simplified scheme of the GSCC (shown in Section 2.2.8), the simplified scheme is used to explain the parts and loops for the tuning process.
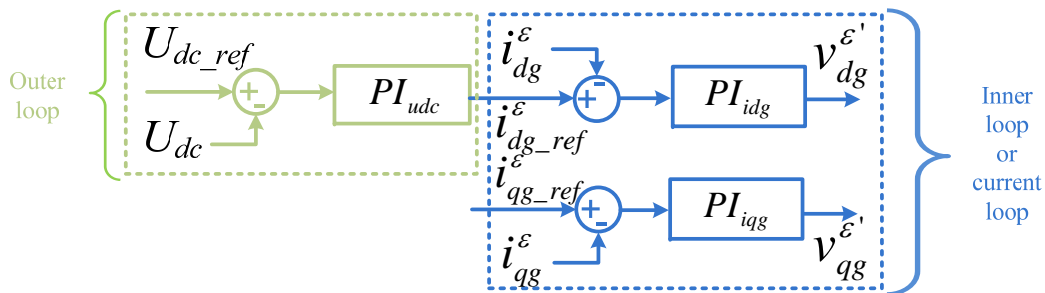
Figure 3.3: Simplified scheme of the outer and inner controllers for the grid-side converter.

Figure 3.3 shows three closed loops; this controller scheme is sometimes referred as cascade topology, due to there is a PI controller followed by other PI controller. The two loops shown in blue are for the current controller, for the d and the q components.

There is one outer loop; in this case, GSC is focused on controlling the DC-link voltage through the component d of inner controller of the back-to-back converter. In this sense, this section is focused on the gain tuning process of these three loops.

3.3.1 Inner Current Controller

Considering the structural similitude, the tuning criterion of a VSC-HVDC system is used for the VSC of DFIG-based WF. The inner current controller is tuned based on the *modulus optimum tuning criterion* described in [79]. In this context, in a cascade control, the inner loop achieves a fast response by canceling the dominant time constant; this process is called zero-pole cancellation.

The transfer functions required for the inner current controller block diagram are shown in Figure 3.4, where the PI controller, PWM time delay approximation, and the plant are considered.

First, the PI controller shown in the block diagram of the Figure 2.5 can be written as follows:

$$K_{pig} + \frac{K_{Iig}}{s} = K_{Pig} \left(\frac{T_{Iig}s + 1}{T_{Iig}s} \right) \tag{3.1}$$

The time delay in the control process associated with the PWM and the digital implementation can be neglected if the rate of change of the controller signal is slower than the PWM commutation and sampled period. The PWM time delay is modeled by an approximation represented by a first-order lag transfer function which delays the input reference voltage $(v_{xg}^{\varepsilon\prime})$ to the output voltage of the converter (v_{xg}^{ε}). The delay is related to the switching frequency, defined as follows:

$$G_{PWM} = \frac{1}{T_a s + 1} \tag{3.2}$$

where $T_a = 1/(2f_{switching})$. The time delay is considering the Padé simplification shown in Appendix B.1.

Developing the tuning criterion given in [79], substituting (2.31) in (2.30), the following transfer function can be obtained applying the Laplace transform:

$$\frac{I_{xg}^{\varepsilon}}{V_{xg}^{\varepsilon}} = \frac{1}{R_g} \frac{1}{\tau_{ig}s + 1} \tag{3.3}$$

where $x = d, q$ and $\tau_{ig} = \dfrac{L_g}{\omega_b R_g}$, all in pu.

Finally, the GSCC block diagram for inner current control is shown in Figure 3.4.

It can be observed in Figure 3.4 that if $T_{Iig} = \tau_{ig}$, the zero-pole cancellation is achieved.
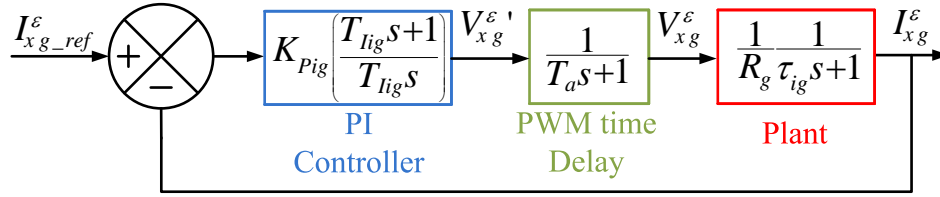
Figure 3.4: GSCC block diagram for the inner current controller.

Then, the reduced open-loop and closed-loop transfer functions of Figure 3.4 are:

$$G_{ig,OL} = \frac{K_{Pig}}{R_g \tau_{ig} T_a s^2 + \tau_{ig} R_g s} \tag{3.4}$$

$$G_{ig,CL} = \frac{K_{Pig}}{R_g \tau_{ig} T_a s^2 + \tau_{ig} R_g s + K_{Pig}} \tag{3.5}$$

respectively. Equation (3.5) can be rewritten as a second-order transfer function in the following form:

$$G_{ig,CL} = \frac{\frac{K_{Pig}}{R_g \tau_{ig} T_a}}{s^2 + \frac{1}{T_a} s + \frac{K_{Pig}}{R_g \tau_{ig} T_a}} \tag{3.6}$$

As stated by (3.6), the undamped natural frequency is $\omega_n = \sqrt{\frac{K_{Pig}}{R_g \tau_{ig} T_a}}$ and the damping factor is $\xi = \frac{1}{2}\sqrt{\tau_{ig} R_g / K_{Pig} T_a}$. Evaluating the condition $|G_{ig,CL}| = 1$ in Equation (3.5), the proportional gain can be found as follows:

$$K_{Pig} = \frac{\tau_{ig} R_g}{2 T_a} \tag{3.7}$$

The open-loop Bode diagram of (3.4) is shown in Figure 3.5. It can be seen that the phase margin corresponds to 65° with a frequency of 4,550 rad/s and the gain margin is infinite, then the open-loop trajectory for the current controller is stable.

The outer controller requires the current-controller transfer function, in this regard, a simplification of (3.6) for zero-pole cancellation is developed. Substituting (3.7) in (3.6) yields $G_{ig,CL1} = \frac{1}{2T_a^2 s^2 + 2T_a s + 1}$. This criterion requires a first-order transfer function to achieve zero-pole cancellation, in this sense, (3.8) is proposed due to the error of the response for a unit-step input between $G_{ig,CL1}$ and $G_{ig,CL2}$ is about zero, this is achieve considering $T_{eq} = 2T_a$ [79]; its demonstration is shown in B.2.

$$G_{ig,CL1} \approx G_{ig,CL2} = \frac{1}{T_{eq} s + 1} \tag{3.8}$$
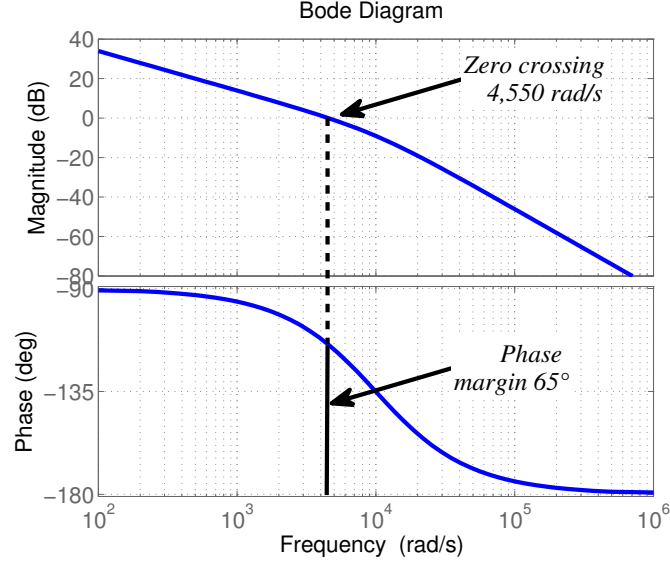
Figure 3.5: Open-loop Bode plot of inner current controller.

3.3.2 Outer Controller

Based on the general block for the outer controller (Figure 3.2), it is required three transfer functions; the PI controller, transfer function of the inner current controller, and the plant. The PI controller, for the outer controller conforming to Figure 2.5, can be rewritten as follows:

$$K_{Pudc} + \frac{K_{Iudc}}{s} = K_{Pudc}\left(\frac{T_{Iudc}s + 1}{T_{Iudc}s}\right) \tag{3.9}$$

The simplification described in (3.8) is used for the outer controller. An auxiliary equation is required to obtain the transfer function of the plant. In accordance with the reference frame ε is along the d−axis of the voltage v_{dg}^{ε} in the bus B1 and the active power in the AC side of the GSC is calculated using $P_{gsc} = v_{dg}^{\varepsilon}i_{dg}^{\varepsilon}$, the power in the DC side of the GSC is calculated as $P_{gdc} = U_{dc}i_{gdc}$, and the power balance in the AC and DC sides meet the following condition $P_{gsc} = P_{gdc}$. According to the above, the Equation (2.18) can be written as follows:

$$\frac{C_{dc}}{\omega_b}\frac{dU_{dc}}{dt} = \frac{v_{dg}^{\varepsilon}}{U_{dc}}i_{dg}^{\varepsilon} - i_{rdc} \tag{3.10}$$

To perform a linear stability analysis it is necessary to linearize (3.10). The linearization is done around steady state, where the values of the equilibrium point are U_{dc_ref}, $V_{dg,0}^{\varepsilon}$ and $I_{dg,0}^{\varepsilon}$, then, the linearization of (3.10) is:

$$\frac{C_{dc}}{\omega_b}\frac{d\Delta U_{dc}}{dt} = \frac{V_{dg,0}^{\varepsilon}}{U_{dc\_ref}}\Delta i_{dg}^{\varepsilon} + \frac{I_{dg,0}^{\varepsilon}}{U_{dc\_ref}}\Delta v_{dg}^{\varepsilon} + \frac{V_{dg,0}^{\varepsilon}}{\Delta U_{dc\_ref}^2}I_{dg,0}^{\varepsilon} - \Delta i_{rdc} \tag{3.11}$$

The input of interest in (3.11) is i_{dg}^{ε}, as a consequence, it can be simplified as:

$$\frac{C_{dc}}{\omega_b}\frac{d\Delta U_{dc}}{dt} = \frac{V_{dg,0}^{\varepsilon}}{U_{dc\_ref}}\Delta i_{dg}^{\varepsilon} - \Delta i_{rdc} \tag{3.12}$$

where Δi_{rdc} is a disturbance signal. The Laplace transform is applied to (3.12), the term Δ is omitted to simplify the block diagram. Finally, the block diagram of the outer controller is shown in Figure 3.6. The reference [79] shows the implementation of feed-forward term in the block diagram, for the tuning criteria the feed-forward term is not included in the Figure 3.6.
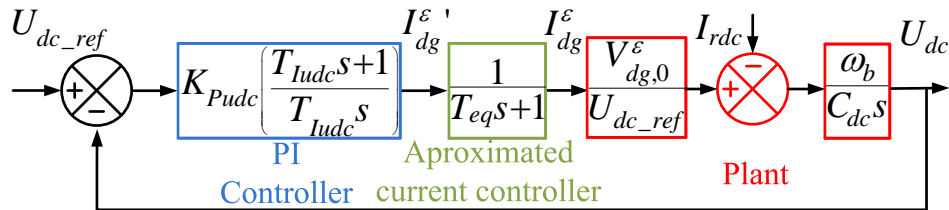
Figure 3.6: Block diagram for outer loop of DC-link voltage.

The open-loop transfer function of the GSCC outer controller without the feed-forward and disturbance input is given by:

$$G_{udc,OL} = K_{Pudc}\left(\frac{T_{Iudc}s + 1}{T_{Iudc}s}\right)\left(\frac{1}{T_{eq}s + 1}\right)\left(\frac{V_{dg,0}}{U_{dc\_ref}}\right)\left(\frac{\omega_b}{C_{dc}s}\right) \tag{3.13}$$

The open-loop transfer function consists of two pole at origin becoming the system marginally stable, in this case, a pole shift does not changes the situation significantly. In this scenario, the *symmetrical optimum tuning criteria* described in [80], can be used. The main idea of this method is that the frequency response of a system, from an input, is forced to be close as possible to the low frequencies of interest, unlike the *modulus optimum tuning criteria* which force the frequency response of the system to that high frequencies. This method has good disturbance rejection, also the method maximizes the phase margin; it is developed as follows.

The equilibrium points can be summarized as $K = V_{dg,0}/U_{dc\_ref}$ and the constants as $T_c = C_{dc}/\omega_b$. Equation (3.13) with the constants K and T_c can be rewritten as:

$$G_{udc,OL}(s) = K_{Pudc}\left(\frac{T_{Iudc}s + 1}{T_{Iudc}s}\right)\left(\frac{K}{T_{eq}s + 1}\right)\left(\frac{1}{T_c s}\right) \tag{3.14}$$

The terms of the above transfer function are rearranged and the frequency terms are change with $s \to j\omega$ as:

$$G_{udc,OL}(j\omega) = \left(\frac{K_{Pudc}K}{T_c T_{Iudc}(j\omega)^2}\right)\left(\frac{T_{Iudc}(j\omega) + 1}{T_{eq}(j\omega) + 1}\right) \tag{3.15}$$

The Nyquist criteria of stability are:

$$|G_{udc,OL}(j\omega)| = 1 \tag{3.16}$$

and

$$\angle G_{udc,OL}(j\omega) = -180 + \Phi_M \tag{3.17}$$

where Φ_M is the phase margin. Then, the angle condition from the open loop of the outer controller is:

$$\angle G_{udc,OL}(j\omega) = -180 + \tan^{-1}(\omega T_{Iudc}) - \tan^{-1}(\omega T_{eq}) = 180 + \phi \tag{3.18}$$

The angle ϕ is positive for all the values of ω. Differentiation this angle with respect to ω can give the maximum value of phase margin. The value of T_{Iudc} should be designed to be small, especially when ϕ approaches Φ_M, otherwise, the response to the disturbance becomes slow. In this sense, the maximization condition $\frac{d\phi}{d\omega} = 0$, the angle is maximum when $\omega_d = \frac{1}{\sqrt{T_{Iudc}T_{eq}}}$. Hence the phase margin is:

$$\Phi_M = \tan^{-1}\sqrt{\frac{T_{Iudc}}{T_{eq}}} - \tan\sqrt{\frac{T_{eq}}{T_{Iudc}}} \tag{3.19}$$

This condition gives the tuning criterion for the time constant of the controller as:

$$T_{Iudc} = T_{eq}\left(\frac{1 + \sin\Phi_M}{1 - \sin\Phi_M}\right) \tag{3.20}$$

The resulting open-loop frequency characteristic will have a maximum phase of Φ_M at the crossover frequency of ω_d, symmetric about $\frac{1}{T_{Iudc}}$ and $\frac{1}{T_{eq}}$. Then, by the symmetric property, it can also written:

$$T_{Iudc} = a^2 T_{eq} \tag{3.21}$$

where a is the symmetrical distance between $1/T_{Iudc}$ to ω_d, and $1/T_{eq}$ to ω_d; in this analysis $a = 6$. Now, from the magnitude condition, the tuning for the gain of controllers can be found as follows:

$$|G_{udc,OL}(j\omega)| = \frac{K_{Pudc}K}{\omega_d^2 T_{Iudc}T_c}\sqrt{\frac{(\omega_d T_{Iudc})^2 + 1}{(\omega_d T_{eq})^2 + 1}} = 1 \tag{3.22}$$

Then, the proportional gain is obtained as follows:

$$K_{Pudc} = \frac{T_c}{K\sqrt{T_{Iudc}T_{eq}}} \tag{3.23}$$

The complete development of this criterion is shown in Appendix B.3. Then, the

open-loop transfer function using the terms T_{Iudc} and K_{Pudc} is described as follow:

$$G_{udc.OL} = \left(\frac{1}{a^3 T_{eq}^2 s^2}\right)\left(\frac{a^2 T_{eq}s + 1}{T_{eq}s + 1}\right) \tag{3.24}$$

The closed-loop transfer function is given by:

$$G_{udc.CL} = \frac{a^2 T_{eq}s + 1}{a^3 T_{eq}^3 s^3 + a^3 T_{eq}^2 s^2 + a^2 T_{eq}s + 1} \tag{3.25}$$

Figure 3.7 shows the frequency response of the open-loop transfer function. It can be noted the phase margin is about 71° with a frequency 830 rad/s and the gain margin is infinite which means that the system is stable.
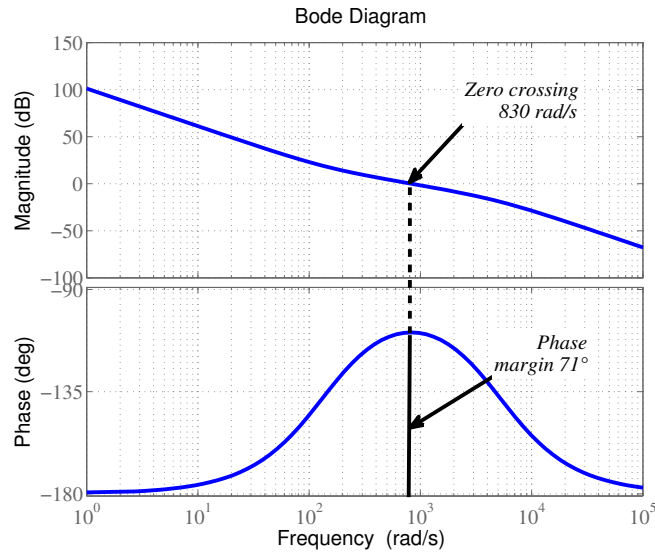
Figure 3.7: Open loop Bode plot of the outer controller for DC-link voltage.

Finally, the closed-loop time response of the inner current controller and the outer controller (Equations (3.5) and (3.25)) due to a unit step function as input are depicted in Figure 3.8. It can be observed the fast response of the inner current loop in comparison with the outer loop.

3.4 Tuning of Rotor-Side-Converter Controller

In this Thesis, the aim of the RSCC topology is to control the stator voltage and the rotor speed. The d component is used to control the stator voltage, while the q component is used to control the rotor speed. In this context, Figure 3.9 shows a simplified scheme of the RSCC (the complete scheme is explained in Section 2.2.9); the simplified scheme is used to explain the parts and loops for the tuning process for the RSCC.
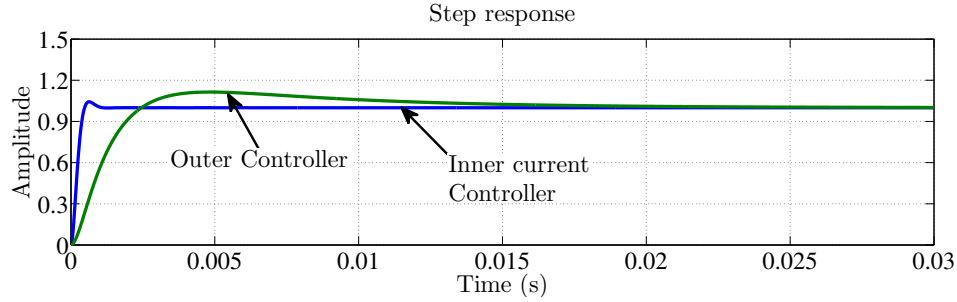
Figure 3.8: Unit step response of the inner current controller versus the outer controller.
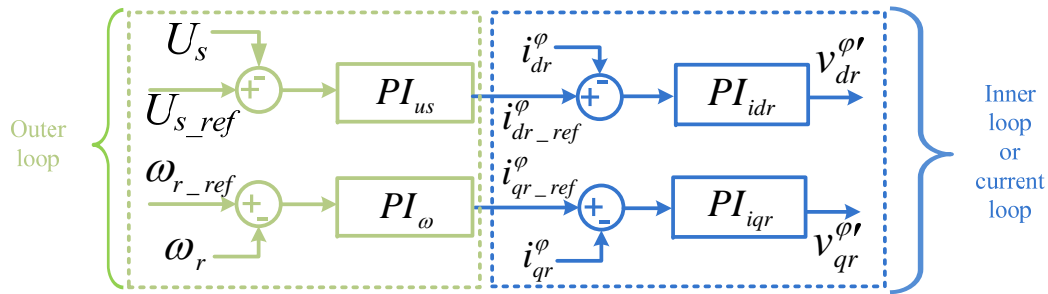
Figure 3.9: Simplified scheme of the outer and inner controllers for the rotor-side converter.

Figure 3.9 shows four loops in cascade. Two inner loops for current control in dq reference frame and two outer loops focus in control the rotor speed of the SCIG through the q component of current and the other one focuses in control the voltage of stator terminals through the d component of current. These controllers are independents and in cascade.

In perspective, the DFIG-based wind farms converters can control various state variables besides active and reactive powers. The DFIG converters can control state variables related to mechanical components as, the rotor speed, torque, stator voltage and, so on, of the induction machine. The tuning process for controlling active and reactive power has been approached in the literature [79, 59], then, in this section the tuning process is analyzed for controlling the rotor speed and the voltage on stator terminals of the induction machine.

3.4.1 Inner Current Controller

The tuning process for the inner current controller of the RSCC can be done by applying the same technique as the above, presented in the Section 3.3.1 where the Bode plots will be the same as Figure 3.5. Besides, the aim of this chapter is focused on present several techniques with which the controller of the DFIG-based back-to-back converter can be tuned; in this section, one extra procedure is performed for tuning the inner current controller. The tuning process for the inner current controller is developed for the d and q axis. The block diagram is made up of PI controller, PWM time delay approximation

and the plant.

First, the PI controller shown in the block diagram in Figure 2.6 is written as:

$$K_{Pir} + \frac{K_{Iir}}{s} = K_{Iir}\left(\frac{K_{Pir}/K_{Iir}s + 1}{s}\right) \tag{3.26}$$

Equation (3.26) for inner current controller is written for d and q axis. Using Equations (2.36) and (2.37), with analytical manipulation, the transfer function of the plant can be obtained as follows:

$$\frac{I_{xr}^{\varphi}}{V_{xr}^{\varphi}} = \frac{1}{\alpha L_r/\omega_b\ s + R_r} = \frac{1/R_r}{\alpha L_r/\omega_b R_r\ s + 1} \tag{3.27}$$

Equation (3.27) is also written for d and q axis. This criterion is based on the control of half-bride converter [81], the block of the transfer function of the PWM time delay approximation is neglected. In this sense, the transfer function block diagram for inner current controller for the RSC is shown in Figure 3.10.
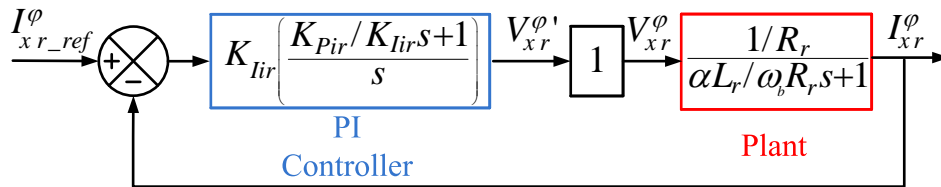
Figure 3.10: RSCC block diagram for inner current controller.

The open-loop transfer function of Figure 3.10 shows a pole at $s = -\omega_b R_r/\alpha L_r$, typically this pole is fairly close to the origin and corresponds to a slow natural response. This transfer function also shows a pole at $s = 0$ which produce a marginally stable system. To improve the open-loop frequency response it is developed the following methodology for DFIG-based VSC.

The criterion proposes the reduction of the block diagram of the inner current controller to a first order plant [81]. Now, based on Figure 3.10 the zero of the control and the pole of the plant can be matched as follows $(K_{Pir}/K_{Iir})s + 1 = (\alpha L_r/\omega_b R_r)s + 1$ in this sense, the closed-loop transfer function of Figure 3.10, in pu, is described by:

$$\frac{I_{xr}^{\varphi}}{I_{xr\_ref}^{\varphi}} = G_{ir,CL} = \frac{1}{\frac{R_r}{K_{Iir}}s + 1} \tag{3.28}$$

The time constant can be defined as $\tau_{ir} = R_r/K_{Iir}$. Based on [81], the rotor time constant for RSC can be assumed to be 0.1 seconds. The rotor time constant (τ_{ir}) should be small for a fast current-control response, but adequately large to be the inner-current-controller bandwidth uncoupled from the outer controller. On the other hand, due to the

zero/pole cancellation, the proportional gain, in pu, is described by:

$$K_{Pir} = \frac{\alpha L_r}{\omega_b R_r} K_{Iir} \tag{3.29}$$

It can be noted that the time constant τ_{ir} can be selected in accordance with the system requirements, as well as, the d and q components can be tuned independently or using the technique that best fit to the requirements of the controllers.

Figure 3.11 shows the frequency response of the open-loop transfer function. It can be noted the phase margin is 90° with a frequency of 10.5 rad/s and the gain margin is infinite which means that the system is stable.
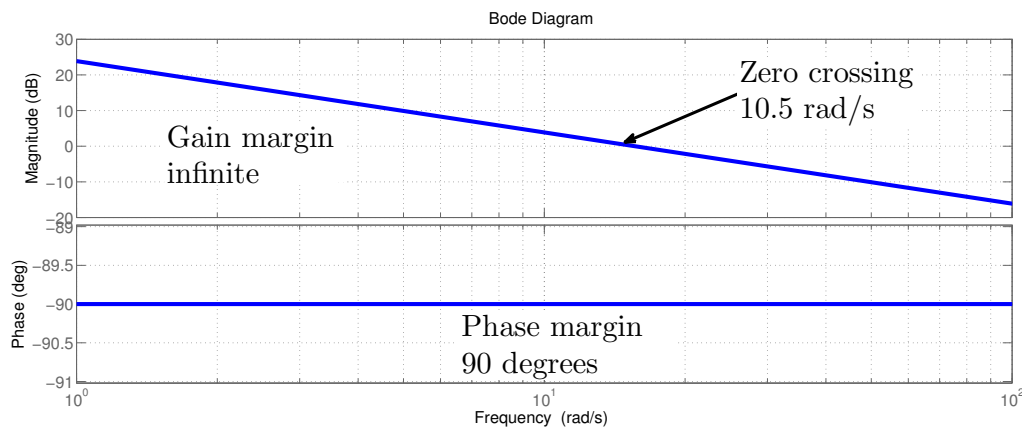
Figure 3.11: Open loop Bode plot of the outer controller for dc-link voltage.

3.4.2   Outer Controller

The outer loop of the RSCC controls the rotor speed and the voltage across the stator terminals of the induction machine. The *symmetrical optimum tuning criteria* can be used as applied in Section 3.3.2. If this criterion is used, the frequency and time response will be the same as above, but in this section, the other two criteria for tuning the outer controller for RSC are performed. The control loop for the rotor speed is tuned according to the step response criteria and the control loop for the voltage across the stator terminals is tuned with the pole location criteria.

Step Response for Rotor Speed (Outer Loop)

The Ziegler–Nichols step response is the most reported method for tuning PID controls since it was proposed [82], and after 60 years of his proposal, there are methodologies for control tuning based on it [83]. This reveals the usefulness of the method. In spite of the drawbacks of the method [83], it can be used for tuning the RSCC. The challenges associated to obtain a transfer function of the RSC can be overcome with this method.

The step-by-step method to tune the RSCC is focused on the S-shape reaction curve, in this sense, if the initial condition of rotor speed of the induction machine is zero, the rotor speed response will resemble an S-shape. In this context, the next steps are followed:

- With zero initial condition and the RSC in open loop, the system shown in Figure 2.1 is simulated until the rotor speed reaches its steady state.
- The transient rotor speed will resemble a S-shape reaction curve.
- The parameters K, T and L are measured from the S-shaped response as it is shown in Figure 3.12.
- Table 3.1 shows the gains for PI control.
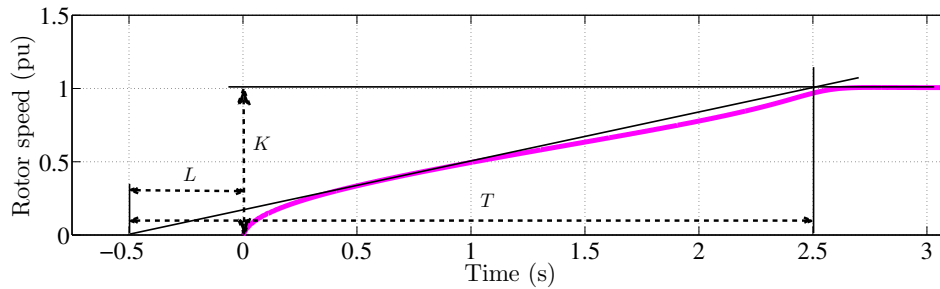
Figure 3.12: Rotor speed of the induction machine, without rotor control.

The results for $T_{I\omega}$ and $K_{P\omega}$ are shown in Table 3.1, where $R = K/T$. Despite of this methodology has been used over many years, it has not been used for tuning RSCC.

Table 3.1: Controller tuning rules for rotor speed controller loop.

Controller	$K_{P\omega}$	$T_{I\omega}$	$T_{D\omega}$
Formulation	0.9/RL	L/0.3	0
Value	5.3731	1.6667	0

Conforming to Figure 2.5, the outer loop is in cascade with the q component of the current loop. Besides, the integral gain is calculated as $K_{I\omega} = \frac{1}{T_{I\omega}}$.

Pole Location for Stator Terminals Voltage (Outer Loop)

The challenge of tuning the outer loop for the voltage across the stator terminals is to find out an expression for the plant. Conforming to Figure 3.2, it is evident that a mathematical expression which relates the rotor current (i_{dr}) with the rms voltage across the stator terminals (U_s) is required. The rms voltage across the stator terminals can be approximated to v_{ds}, namely $U_s \approx v_{ds}$. In steady-state an expression can be synthesized from the induction model (Equation (2.15)) as follows:

$$\frac{di_{dr}}{dt} = -\omega_b(v_{ds} - R_s i_{ds} + \omega_s \psi_{qs})L_m/L_r L_s \alpha + \omega_b(v_{dr} - R_r i_{dr} + \omega_{slip}\psi_{qr})/L_r \alpha \qquad (3.30)$$

In accordance with the criterion explained in Section 3.3.2, in this case, the equilibrium points are $V_{ds,0}^{\varphi}$ and $I_{dr,0}^{\varphi}$, the linear equation which relates the input with the output without the disturbance and feed-forward terms is written as follows:

$$\frac{\Delta V_{ds}}{\Delta I_{dr}} = \frac{(L_r^2 L_s \alpha^2 + \omega_b L_r L_s \alpha R_r)s}{-\omega_b L_m L_r \alpha} \tag{3.31}$$

Conforming to the general block diagram shown in Figure 3.2 of the outer controller, the block diagram for stator terminal voltage is shown in Figure 3.13.
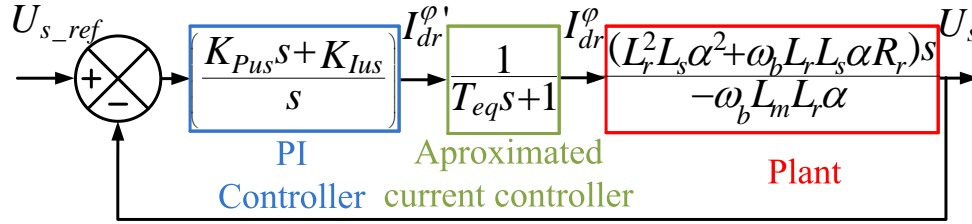
Figure 3.13: RSCC block diagram for outer controller.

The closed-loop transfer function of Figure 3.13 can be reduced in a first order system as it is shown in (3.32). As reported by (3.32), the constraints are set to assure the localization of the pole at the left side of the $s-$plane. In this sense, the proportional and integral gains are computed according to (3.33) and its values are $K_{Ius} > 18.2351$ and $K_{Pus} > 0.0112$.

$$Gus, CL = \frac{(L_r^2 L_s \alpha^2 + \omega_b L_r L_s \alpha R_r)K_{Pus}s + (L_r^2 L_s \alpha^2 + \omega_b L_r L_s \alpha R_r)K_{Ius}}{((L_r^2 L_s \alpha^2 + \omega_b L_r L_s \alpha R_r)K_{Pus} - T_{eq}\omega_b L_m L_r \alpha)s + (L_r^2 L_s \alpha^2 + \omega_b L_r L_s \alpha R_r)K_{Ius} - \omega_b L_m L_r \alpha} \tag{3.32}$$

$$K_{Ius} > \frac{\omega_b L_m L_r \alpha}{L_r^2 L_s \alpha^2 + \omega_b L_r L_s \alpha R_r} \quad \text{and} \quad K_{Pus} > \frac{T_{eq}\omega_b L_m L_r \alpha}{L_r^2 L_s \alpha^2 + \omega_b L_r L_s \alpha R_r} \tag{3.33}$$

Figure 3.14 shows the frequency response of the open-loop transfer function. It can be noted the phase margin is -65° (425°) with a frequency 11.5 rad/s and the gain margin is infinite which means that the system is stable.

3.4.3   Dynamic Performance of the System: Gains Test

The complete system shown in Figure 2.1 is studied. Besides, the proposed methodology to calculate the gains of the GSCC and RSCC are compared against the ones reported in the literature as [84, 85, 86]. This comparison is conducted with quasi-stationary changes in the series compensation (capacitance C_{cs}) to produce SSR.
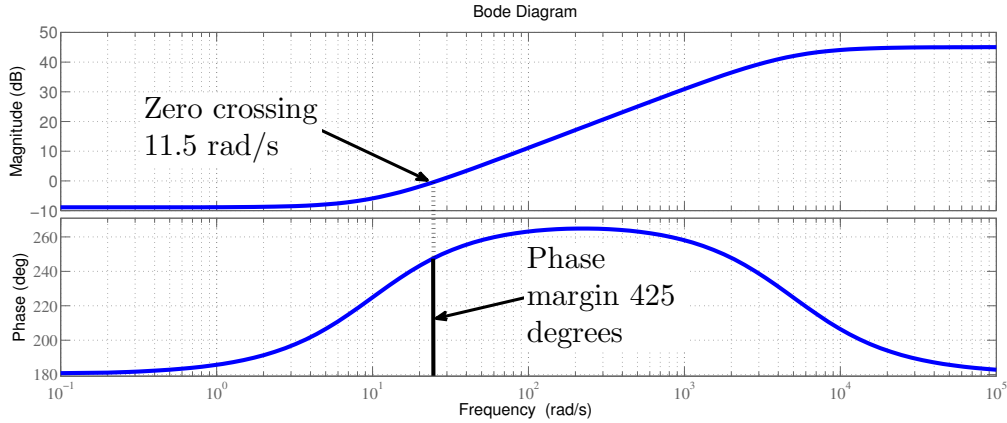
Figure 3.14: Open loop Bode plot of the outer controller for DC-link voltage.

Table 3.2 shows the gains calculated through the proposed tuning methodology and the gains recommended in the literature. Thus, the reference [84] recommends control parameters values for wind turbines between 1.67 MVA to 4.0 MVA. The simulation is performed using this recommendation and the parameters described in the model of the type 3 wind turbine analyzed in [85, 86].

Table 3.2: Gains used in the GSCC and RSCC.

Gains	Literature	Calculated	Gains	Literature	Calculated
K_{Pudc}	8	4.033	T_{Ius}	0.05	100
T_{Iudc}	2.5×10^{-3}	7.2289×10^{-3}	K_{Pidr}	0.01	0.0087397
K_{Pidg}	0.83	3.962958	T_{Iidr}	4	0.1
T_{Iidg}	0.2	0.265258	$K_{P\omega}$	5.3731	5.3731
K_{Piqg}	0.83	3.962958	$T_{I\omega}$	1.6667	1.6667
T_{Iiqg}	0.2	0.265258	K_{Piqr}	0.05	0.0087397
K_{Pus}	2	0.1	T_{Iiqr}	0.02	1×10^{-1}

The evaluation of the system is performed with these two set of gains and the analysis is conducted by simulating the system with series compensation of 10% as initial condition, when the system reaches the steady-state at 100 seconds, the series compensation is changed to 70%, and then to 71% at 105 seconds. These compensation levels are selected to excite the SSR of the system. Figure 3.15 shows the comparison of the DC-link voltage; the blue line (solid line) is the solution computed with the gains given by the literature, while the green line (dash line) corresponds to the solution computed with the gains of the methodology shown in previous section.

The dynamic simulation results shown in Figure 3.15 can be summarized as follows:

- In the case with the gains from literature, the level of series compensation required to observe SSR is at 71%.
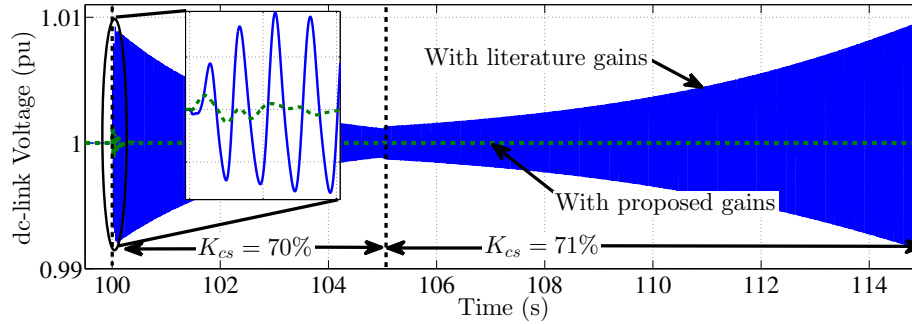
Figure 3.15: Comparison of DC-link voltage of the calculated versus literature gains.

- The proposed methodology for gains calculation shows an enhancement on the dynamic behavior of the system, such that the SSR event is overcome, as shown in the dynamic simulation.
- Conforming to these results, the mitigation of the SSR can be achieved by retuning the gains of the RSCC and GSCC. In this sense, if the solution to mitigate SSR is based on the implementation of a FACTS device, the origin of the SSR must be understood to propose a solution or equipment.

3.5 Analysis Techniques for SSR

In this Section, the basic theory of the analysis techniques to study resonance phenomenon used in this Thesis is presented. The analysis techniques are frequency scan, modal impedance, and small-signal-stability analysis. An example is performed to show the properties of each technique.

3.5.1 Frequency Scan

The frequency scanning technique is a basic technique to analyze the potential of a certain frequency in a mechanical-electrical system to produce resonance. Different analysis techniques have emerged based on frequency scanning techniques. The most common techniques are listed below [24, 27, 43].

1. Reactance scan.
2. Voltage and current injection.
3. Impedance model.
4. Modal impedance.

The frequency scanning technique involves the determination of the driving point impedance over the frequency range of interest. Most of the analysis for SSR issues includes eigenvalue analysis, but in some scenarios where the analyzed system includes

more than twenty buses, the eigenvalue studies are not suitable due to the amount of information [4, 24]. In this scenario, frequency scanning studies are able to analyze systems over 100 to 150 buses [4]. The frequency scanning technique will not identify by itself the resonance frequency or the critical frequency, but as a whole, with eigenvalue studies, the effort and requirements for identifying the frequency subjected to produce SSR will be reduced.

In accordance with the above, it is introduced an example of the use of a typical frequency scan. Figure 3.16 shows a simple three-buses circuit, where the system is composed of inductors and capacitors; the resistance is neglected to amplify the results. There are two easy and common ways to perform the frequency scan, one is computing an equivalent impedance from the bus of interest and the second is injecting a current of several frequencies in the bus of interest. In this case, the equivalent impedance is analytically computed for each bus.
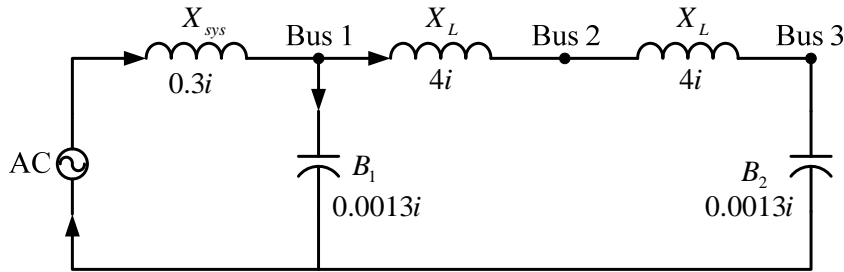
Figure 3.16: Three-bus test system.

Where X_{sys} is the reactance of the system, X_L is the line reactance, B_1 and B_2 are the susceptance and those can be transformed as $X_c = 1/B_{1-2}$. The quantities in Figure 3.16 are in *pu* frequency based on the fundamental frequency and it is equal to an harmonic number. Using superposition theory and Thévenin theorem, the resonance frequency due to each capacitor and due to the two capacitors can be found easily. The approximated resonance frequencies, using the Equation $f_{res} = \sqrt{MVAr_{sc}/MVAr_c} = \sqrt{X_c/X_{sc}}$ (where $MVAr_{sc}$ are the short circuit reactive MVA and $MVAr_c$ are the capacitance reactive MVA). The resonance because of the capacitor from bus B1 is computed considering the capacitor on bus B3 as open-circuited, and vice versa to compute the resonance on bus B3. The resonance frequencies are computed as follows:

$$f_{res1} = \sqrt{\frac{796.23}{0.3}} = 50.64 \, pu$$

$$f_{res3} = \sqrt{\frac{796.23}{8.3}} = 9.63 \, pu$$

In this sense, the resonance frequency due to the capacitor in bus 1 is approximately

50.64 *pu* and the resonance frequency due to the capacitor in bus 3 is approximately 9.63 *pu* In this example, the frequency scan is computed for the bus 1, bus 2, and bus 3. The equivalent equations for each bus are summarized as follows:

$$jX(\omega)_{B1} \;=\; \frac{(jX(\omega)_{eq1})(2jX(\omega)_L - jX(\omega)_c)}{jX(\omega)_{eq1} + 2jX(\omega)_L - jX(\omega)_c} \tag{3.34}$$

$$jX(\omega)_{B2} \;=\; \frac{\left(jX(\omega)_{eq1} + jX(\omega)_L\right)\left(jX(\omega)_L - jX(\omega)_c\right)}{jX(\omega)_{eq1} + j2X(\omega)_L - jX(\omega)_c} \tag{3.35}$$

$$jX(\omega)_{B3} \;=\; \frac{\left(jX(\omega)_{eq1} + 2jX(\omega)_L\right)\left(-jX(\omega)_c\right)}{jX(\omega)_{eq1} + 2jX(\omega)_L - jX(\omega)_c} \tag{3.36}$$

where:

$$jX(\omega)_{eq1} = \left(\frac{(jX(\omega)_{sys})(-jX(\omega)_c)}{jX(\omega)_{sys} - jX(\omega)_c}\right) \tag{3.37}$$

where ω is the frequency sweep vector. The frequency scan for the equivalents reactance $jX(\omega)_{B1}$, $jX(\omega)_{B2}$, and $jX(\omega)_{B3}$ is performed through MatLab. Figure 3.17 shows the frequency scan of the three buses (all in *pu*). The results reveal that the resonance phenomenon can be observed in the three buses, more precisely the parallel resonance is observed at a frequency of 9.61 *pu* and 51.61 *pu*, also, it is observed points of series resonance (out of the interest of this analysis) in bus 2.
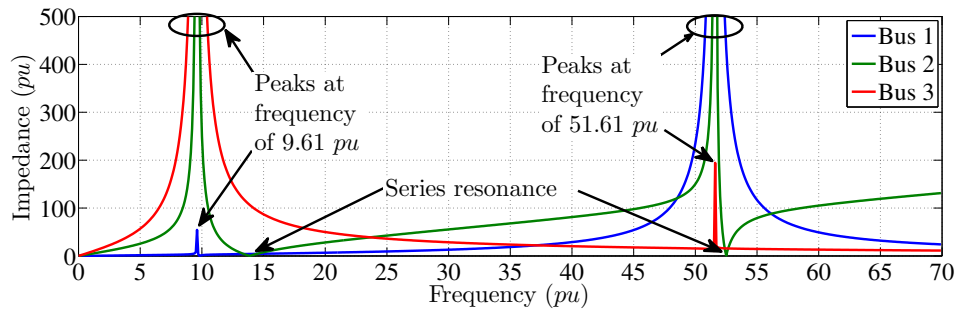
Figure 3.17: Frequency scan from the three-bus test system.

In conclusion, the methods based on frequency scanning techniques can be easily applied and the driving points impedance can be located easily, but to identify the capacitor that origins the resonance in large systems with several sources of resonance can be an impossible task.

3.5.2 Modal Impedance

Despite the disadvantages of the frequency scanning techniques, the modal impedance technique can solve some of the disadvantages shown in the previous section. The formu-

lation of this method is developed in [87].

In accordance with the above-explained, an example is performed using the circuit shown in Figure 3.16. The network admittance matrix is required for such purposes. In this sense, Figure 3.18 shows the respective single-line diagram of the three-bus system.
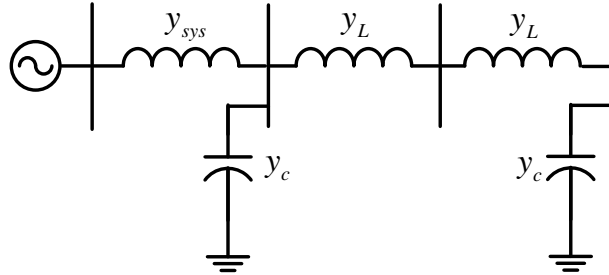
Figure 3.18: Single-line diagram of the three-bus test system [4].

The elements of the node admittance matrix are:

$$Y_{11} = y_{sys} + y_L + y_c \qquad Y_{12} = -y_L \qquad Y_{13} = 0$$
$$Y_{21} = -y_L \qquad Y_{22} = y_L + y_L \qquad Y_{23} = -y_L$$
$$Y_{31} = 0 \qquad Y_{32} = -y_L \qquad Y_{33} = y_L + y_c$$

where $y_{sys} = 1/jX_{sys}$, $y_L = 1/jX_L$, and $y_c = 1/-jX_c$.

Figure 3.19 shows the modal impedance of the three-bus test system shown in the above section. It is shown the modal impedance versus frequency (both in *pu*). Unlike of the typical frequency scanning technique, modal impedance can identify the bus which is the source of the resonance. In this sense, it is shown that the resonance frequency in mode 1 is 51.61 *pu*. There is no resonance frequency in mode 2, while the resonance frequency due to Mode 3 is 9.61 *pu*. It is also shown that the series resonance observed on Figure 3.17 is also discriminated.
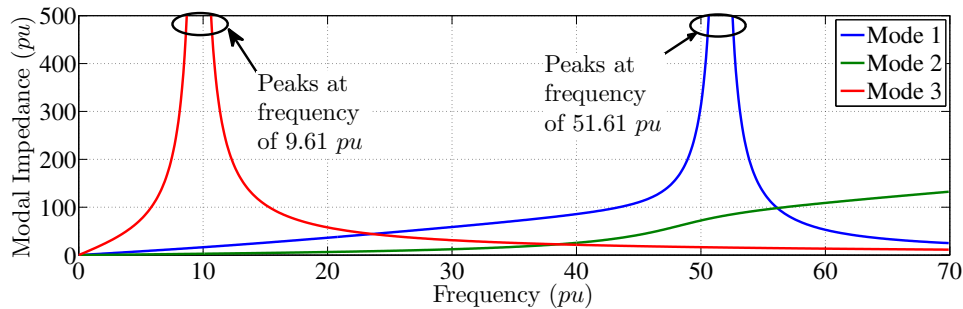
Figure 3.19: Modal impedance from the three-bus test system.

As reported by [87], the critical right eigenvector has the potential to characterize the location excitability of the critical mode and the critical left eigenvector can represent the

location observability of the critical mode. In this example, the critical modal impedance of, Z_1 is found at the frequency of 51.61 pu and for Z_3 is found at 9.61 pu. In this context, it is possible to combine the excitability and observability into a single index according to the selective modal analysis [88], then, the participation factor can be defined as:

$$PF_{bm} = L_{bm}T_{mb} \tag{3.38}$$

where b is the bus number and m is the mode number. The highest participation factor indicates the bus of the source of resonance of a specific mode.

Table 3.3: Results of modal analysis from the three-bus test system.

| Mode →			Mode 3 (9.61pu)	Mode 1 (51.61pu)
Critical eigenvalue →			$0.00021\angle -10.8°$	$0.00015\angle -10.43°$
Critical eigenvectors	T	Bus 1	$T_{31} = 0.0332\angle 0.6°$	$T_{11} = 0.9002\angle -0.31°$
		Bus 2	$T_{32} = 0.4605\angle 0.15°$	$T_{12} = 0.4344\angle 0.51°$
		Bus 3	$T_{33} = 0.8870\angle -0.11°$	$T_{13} = 0.0338\angle -179.38°$
	L	Bus 1	$L_{13} = 0.0332\angle 0.68°$	$L_{11} = 0.9001\angle 0°$
		Bus 2	$L_{23} = 0.4605\angle 0.26°$	$L_{21} = 0.4343\angle 0.82°$
		Bus 3	$L_{33} = 0.8870\angle 0°$	$L_{31} = 0.0338\angle -179.07°$
Participation factor (magnitude)		Bus 1	$PF_{13} = 0.0011$	$\mathbf{PF_{11} = 0.8103}$
		Bus 2	$PF_{23} = 0.2121$	$PF_{21} = 0.1887$
		Bus 3	$\mathbf{PF_{33} = 0.7868}$	$PF_{31} = 0.0011$

The participation factors in bold in Table 3.3 are the critical ones which indicate that the critical mode 1 has its source of resonance in bus 1, while the critical mode 3 has its source of resonance in bus 3.

In conclusion, modal impedance technique can be used to identify the resonance frequency in a specific bus; the properties of **observability** and **excitability** of the critical mode can be found in the modal impedance technique [87]. In this Thesis, the advantages of modal impedance technique are proposed to be used for SSR issue.

3.5.3 Small-Signal-Stability Analysis

Small-signal stability or small-disturbance stability as reported by [65] is the ability of the power system to maintain synchronism under small disturbance. Such disturbances occur continually on the system because of small vibrations in loads and generators. The disturbances are considered sufficiently small for linearization of systems equations to be permissible for purposes of analysis. The instability that may result can be of two forms: (i) steady increase in rotor angle due to lack of sufficient synchronization torque, or (ii) rotor oscillations of increasing amplitude due to lack of sufficient damping torque. The nature of the system response to small disturbance depends on a number of facts including the initial condition, the transmission system strength, and the type of generator excitation

controls used. For a general connected radially line to a large power system, in the absence of automatic voltage regulators (i.e., with constant field voltage) the instability is due to a lack of sufficient synchronizing torque. This results in instability through a non-oscillatory mode. With continuously acting voltage regulators, the small-disturbance stability problem is one of ensuring sufficient damping of system oscillations. Instability is normally through oscillations of increasing amplitude [65].

In this Thesis, the tools of SSSA are used, in this sense as reported by [65], the concepts are required to develop the proposed methodologies and analysis.

3.6   Discrimination and Identification Process for SSR

In this section, a procedure is proposed to determine the causes of how a series-compensated transmission line can produce SSR in a DFIG-based wind farm. Through an analytical procedure and according to the definition of IGE, TI, and TA, the behavior observed in the simulation is compared with the definitions to know which of them is the cause of SSR. In this regard, according to the equivalent circuit of the DFIG described in [89], the average model of the VSCs [81], and the DPI technique [90], the steady-state equivalent circuit can be considered as shown in Figure 3.20, based on it, modal impedance [87] and driving point impedance [40] are computed for SSR characterization. Then, the eigenproperties are assessed as the eigenvalues of the entire system to make a relationship between the results of SSSA and the steady-state analysis.
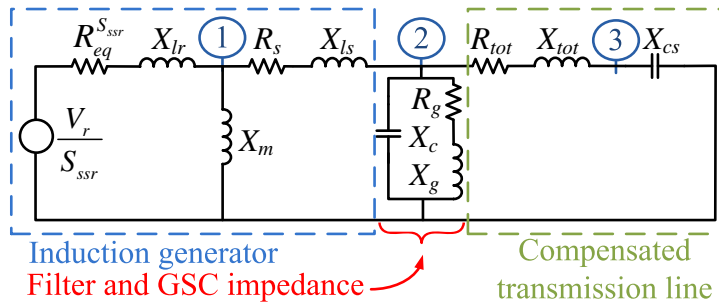
Figure 3.20: Steady-state equivalent circuit of the system shown in Section 2.2.

In this sense, the equivalent circuit is analyzed to show the procedure to determine the origin of SSR phenomenon produced by IGE, TI or TA. The SSR phenomenon is not affected by power electronic or its controllers due to this is a purely mechanical-electrical phenomenon [5, 6, 11].

For example, since IGE is purely electrical phenomenon, it is required only the equivalent circuit. For a steady-state condition, the resistance $R_{eq}^{S_{ssr}}$ can be calculated and using MI or DPI techniques in the equivalent circuit in Figure 3.20 the phenomenon can be evaluated; if the magnitude of $R_{eq}^{S_{ssr}}$ exceeds the sum of the stator and network resistance, SSR is produced by IGE.

TI can be evaluated if it is assumed that the mechanical natural frequency (f_n) is rendered to the stator terminal of the induction generator as signal of component f_{en}, using the equivalent circuit of Figure 3.20 and the DPI or MI techniques, the network natural frequency (f_{er}) for a sweep of the reactance X_{cs} can be calculated, if for any value of X_{cs} there is a match in the frequencies f_{en} and f_{er}, SSR is produced by TI.

TA can be evaluated if it is assumed that a subsynchronous frequency (f_{er}) is excited in the network side, then it is induced a component of frequency f_m in the stator terminals of the induction generator and if a mechanical or electromechanical frequency matches with the induced frequency f_m, SSR is produced by TA.

In the above context, the task is focused to assure adequately the causes and effects of the measured harmonic, in this sense the steady-state techniques and SSSA technique are used as a complement to each other.

3.6.1 The steady-state analysis techniques for SSR

From Figure 3.20, X_{lr} and X_{ls} are the rotor and stator leakage reactance; R_s is the stator resistance; X_m is the mutual reactance; V_r is the rotor voltage; R_g and X_g are the resistance and reactance of GSC; the total resistance of the system is $R_{tot} = R_{line} + R_T$; the total reactance of the system is $X_{tot} = X_{line} + X_T$; the series compensation is $X_{cs} = K_{cs}X_{line}$.

The first step of the investigation is to seek out the resonance frequency because of the series compensation, as the first instance, it can be done by Equation (1.1), $f_{er} = f_o\sqrt{\dfrac{X_C}{X_{tot}}}$, which will give a small deviation due to that, this equation does not consider the reactance of the parallel branches. But this equation gives a close approximation of the SSR frequency of the network.

DPI can be evaluated with the complete steady-state circuit. One common procedure is based on the injection of a voltage or current at several frequencies in a concerning bus to know the impedance response at a specific frequency [4]. Another method is to obtain an analytic expression of the equivalent impedance in each bus, due to the small size of the equivalent circuit in this study, an analytic expression of the impedance at bus 3 (bus of the series compensation) is obtained as follows:

$$Z_{bus3} = \frac{Z(\omega)_{eq3}Z(\omega)_{cs}}{Z_{eq3} + Z_{cs}} \tag{3.39}$$

with $Z(\omega)_{cs} = -jX(\omega)_{cs}$, $Z(\omega)_{eq3} = (Z(\omega)_{eq1} + jX(\omega)_{ls})Z(\omega)_{cp}/(Z(\omega)_{eq1} + jX(\omega)_{ls} + Z(\omega)_{cp}) + X(\omega)_{tot}$, $Z(\omega)_{eq1} = (jX(\omega)_{lr})(jX(\omega)_m)/(jX(\omega)_{lr} + jX(\omega)_m)$, and $Z(\omega)_{cp} = (jX(\omega)_g)(-jX(\omega)_c)/(jX(\omega)_g - jX(\omega)_c)$; the term X_c as the filter reactance. The resistances are neglected to observe only the effect of the reactance.

MI is commonly used for resonance analysis above the synchronous frequency [87]. In this research, MI is used for SSR analysis in DFIG-based WFs. The main benefit of this technique is the discrimination of several sources of resonance, as explained in [87]; further

simulations show that the discrimination property is preserved for the SSR case.

Figure 3.21 shows the natural frequency of the network (f_{er}) and the induced frequency (f_m) versus series compensation. The magenta line shows the compensation level at which the system starts the resonance condition, described in Section 3.4.3. The green line (dash line) shows the behavior for the DPI and MI, the results applying the Equation (1.1) are shown in the blue line (solid line). Conforming to Equation (1.1), f_{er} = 42.9 Hz in consequence f_m = 17.1 Hz. But, according DPI and MI f_{er} = 16.51 Hz in consequence f_m = 43.49 Hz. The data interpretation, in this case, shows that DPI and MI deliver similar results, while the error can be larger using (1.1); this is confirmed by modal analysis.
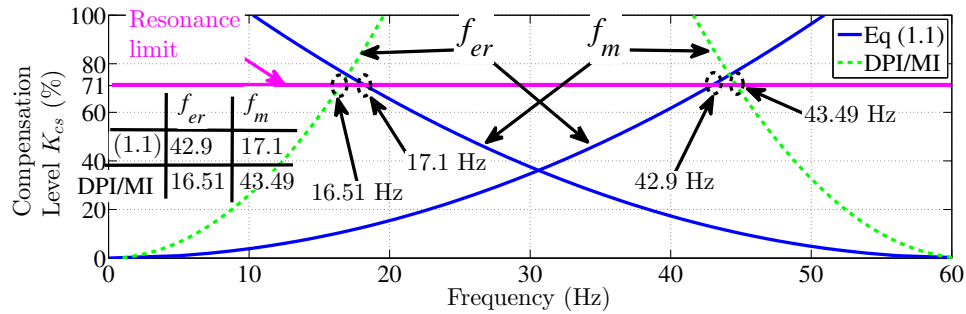
Figure 3.21: Natural frequency and induced frequency versus series compensation level of Equation (1.1), DPI and MI.

The main difference concerning DPI and MI is depicted in Figure 3.22, where the equivalent impedance from bus 3 versus frequency is shown. The blue line (solid line) represents the DPI and the green line (dash line) represents the MI. The figure is split in two, for subsynchronous and supersynchronous frequency levels. The peak in the range of subsynchronous frequency can be matched with the frequency of f_{er} = 16.51 Hz on Figure 3.21, which represents the resonance frequency of the electrical network, in consequence, the peak shown in the subsynchronous range in Figure 3.22 is due to the series compensation. Because there are only two capacitors in the equivalent circuit, the peak in the range of supersynchronous frequency is due to the passive filter at 1437 Hz.
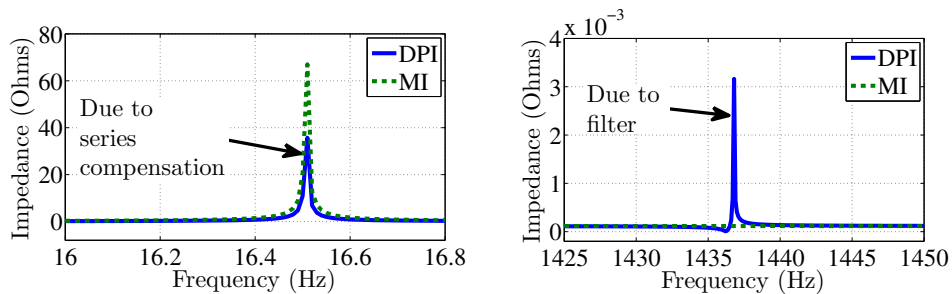
Figure 3.22: Impedance versus frequency of DPI and MI from bus 3 at different frequency ranges, with a compensation level of 71%.

MI technique shows only one peak corresponding to the effect of the series capacitor, while DPI shows the effect of the two capacitors. As a result, in a complex system where several series-compensated transmission lines are installed, the use of MI as an analysis technique will allow discriminating the effect of each series-capacitor in the system.

3.6.2   Small-Signal Stability Analysis for SSR

Small-signal stability is widely used for stability studies [65, 91]. In this section, the linearization of the complete system, as well as the eigenvalue and eigenvectors are calculated by means of *fsolve* function of MatLab. The identification of each mode is described with the MI technique and the eigenvalue analysis. Using the MI technique and Equation (1.6), the induced subsynchronous and supersynchronous frequencies (f_m) are computed as shown in Figure 3.23.
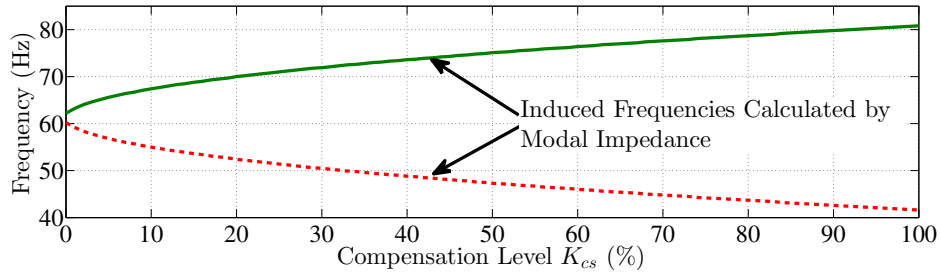
Figure 3.23: Induced frequency versus series-compensation level computed by MI.

According to the modal analysis, Figure 3.24 shows the main modes at their respective frequency versus compensation level. First, in Figure 3.24 the induced modes can be identified due to their frequency behavior through the compensation level is similar to the Figure 3.23. Besides, the mode due to the filter in Figure 3.24 can be identified due to its frequency behavior is close to the supersynchronous frequency computed by MI technique and shown in Figure 3.22; the resonance frequency of the electrical system due to the filter is around of 1438.5 Hz, conforming to modal analysis.

The identification of the mechanical mode is required. The shaft train model is based on the two-mass model, the torsional mode is one and its frequency can be calculated in the steady-state condition as follows [92]:

$$\omega_n = \sqrt{\frac{K_{tg}(H_g + H_{wt})\omega_{mb}}{2H_g H_{wt}}} \tag{3.40}$$

As stated by (3.40), the mechanical mode is identified in Figure 3.24. The supersynchronous modes are not shown in this analysis due to they are not involved in SSR, but those can be associated with the controllers.
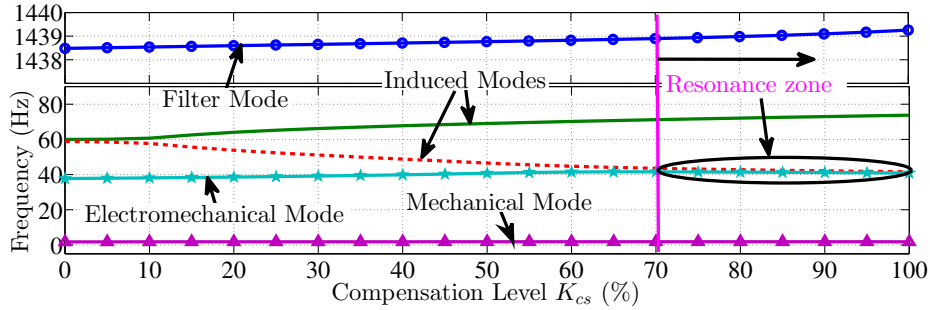
Figure 3.24: Imaginary part of the main modes versus compensation level.

The SSR definition [11] indicates that if two modes (in this case electromechanical and electrical) are close enough, the system can oscillate indefinitely. In this regard, as the compensation level increases, the subsynchronous induced mode is getting close to the electromechanical mode, producing the resonance zone. Conforming to Figure 3.24, the subsynchronous induced mode at compensation level of 71% shows a frequency of 43.56 Hz, while the electromechanical mode at the same compensation level shows a frequency of 41.56 Hz, the difference of 2 Hz is called *frequency gap of SSR*; a frequency gap of SSR equal or lower than 2 Hz produce SSR.

It can be observed that the induced component (f_m) for the MI technique is 43.49 Hz, which is too close to the computed ones using modal analysis with the frequency of 43.56 Hz. The conclusion is that MI technique can be used to calculate the SSR frequency for the case when a disturbance induces a frequency to the generator; which corresponds to the TA phenomenon.

Figure 3.25 shows the same modes as above, in this case, the real part of the modes is shown. The resonance zone is shown after the series compensation of 70% and the real part of the electromechanical mode changes to positive in K_{cs} = 71%, which makes the system unstable.
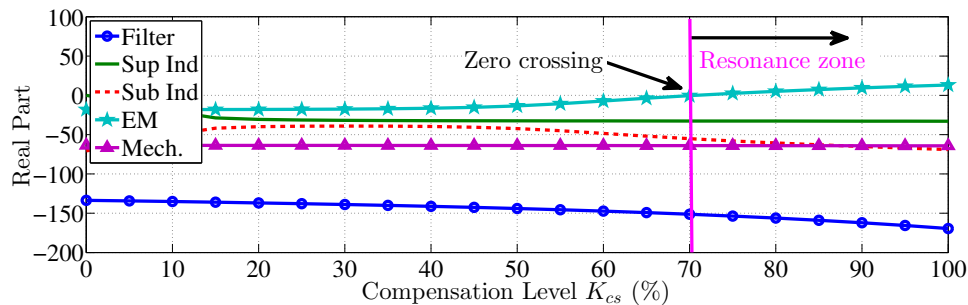
Figure 3.25: Real part of the main modes versus compensation level.

3.6.3 Discrimination Criteria and Comments

The procedure to discriminate the phenomena that can produce SSR is finally described as follows:

1. Implement the modal impedance technique presented in Section 3.5.2.
2. Perform the small-signal-stability analysis presented in Section 3.5.3.
3. By using the results of the small-signal analysis, determine the frequencies associated to these eigenvalues. Compare these frequencies with those obtained in the step 1. The matching frequencies will be the interest frequencies related to the SSR.
4. If $R_{eq}^{S_{ssr}} < R_{tot}$ is fulfilled, then IGE is discriminated. SSS analysis is not required.
5. If the frequency f_{en} (1.5) rendered to the network is not close to the frequency f_{er} (1.1), TI is discriminated.
6. If an induced current component in the generator of frequency f_m (1.6) is not close to any frequency associated to the turbine-generator modes, TA is discriminated.

In this research, IGE is discriminated due to the condition $R_{eq}^{S_{ssr}} < R_{tot}$ is fulfilled, otherwise, MI technique would show a zero crossing in the impedance versus frequency plot, as Figure 3.22. TI is discriminated due to the frequency of the voltage component rendered to the system in the condition of SSR (compensation of 71%), according Equations (1.5) and (3.40), is f_{en} = 58.23 Hz, which is not close to the subsynchronous frequency f_{er} = 16.51 Hz in the electrical system, shown in Figure 3.21, green-dash line.

The precise interpretation of the analysis indicates that, due to series compensation of 71%, current components of frequency around f_m = 43.56 Hz (conforming to Figure 3.24) are induced in the generator which is close to the electromechanical mode, in this case with a frequency of 41.56 Hz, which match with the definition of TA, therefore SSR arises in the transmission system.

In accordance with the criteria of phenomena discrimination performed in this research, in a complex system with several sources of resonance (as capacitors in series or parallel), it is possible to know precisely the buses that are prone to producing SSR.

3.7 Chapter Discussion

VSCs are used for several purposes and configurations. In WECS, the type 3 configuration has challenges related to controlling the state variables of interest. In this Thesis, VSCs of type 3 configuration is aimed to control the voltage of the DC-link, the voltage of the stator terminals of the induction generator, and the rotor speed of the induction machine; there are other state variables or parameter objectives as active power and reactive power, currents, and so on, that can be controlled. In the scenarios presented in this Thesis, the controller parameters are related to the induction machine, so the electrical and mechanical elements are related to the control block. This leads to the challenge to find a transfer function that relates the mechanical with the electrical elements. In this context, the

methodologies presented to give an excellent option for tuning the GSCC and RSCC. The results show excellent performance with the computed gains in a subsynchronous resonance condition. In some scenarios, the transfer function required for the tuning process is avoided and the gains are computed by dynamic simulations. Besides, the proposed transfer function for the voltage control of stator terminals can be used to apply the desired methodology for tuning.

The quantity of the analysis techniques to characterize SSR available in the literature is varied, as the ones implemented in this Thesis or impedance model, bifurcation, and so on. In this context, to make a comparison with the other techniques is out of the scope of this Thesis. The main objective of the selected techniques is to combine the goodness of a technique that can be applied easily with another technique that takes more effort to be applied. The combination of both gives an overall understanding of the problem.

Finally, before applying a solution to mitigate the SSR issues, it is required to know the process and phenomenon that generate the subsynchronous resonance. The discrimination and identification process, shown in the last section, can apply to any scenario where a steady-state equivalent circuit can be obtained.

Chapter 4

Modal Analysis with BESS Integration for SSR in DFIG-based Wind Farm

4.1 Introduction

In this section, a BESS is analyzed as a solution to overcome the SSR problems without changing the gains of the controllers of the back-to-back converter analyzed in the previous section, the model of the BESS remains as indicated in Section 2.2.11. In this chapter, it is explained the extra advantages due to the power management capabilities of the BESS. In this sense, the participation factors and eigenvalue sensitivity are explained in the use of a DFIG-based wind system, and the participation of each element of the system in the process of SSR issue is explained; based on the PFs and ES, an extra solution is applied to improve the characteristics of the stability of the entire system.

It has been demonstrated that BESS contributes to improving the power management on power systems or microgrids, and can be used for different purposes. Among the most common are peak shaving and load frequency control [71, 93]. The turbo-generator system connected to a double transmission line (second benchmark [94]) is analyzed in [72] to examine the dynamic behavior of the BESS, where the eigenvalue analysis is used to demonstrate the additional damping provided by the BESS. The stability of a stand-alone microgrid operating with a diesel generator is improved by the application of the BESS, where the improvement is shown with the root locus from the characteristic equation of the transfer function [78]. The integration of the BESS into a flexible AC transmission system (FACTS) has been analyzed, the integration of a BESS with a StatCom is analyzed in [9, 77, 95, 96], the results show that the StatCom/BESS exhibits increased flexibility over the traditional StatCom with improved damping capabilities, power management, and voltage control.

BESS integration in DFIG-based wind farms has been analyzed for various scenarios; in [97], the BESS is used to control the low voltage and the power fluctuation on a microgrid. The BESS is connected in the DC-link, which further strengthens the controllability of the

grid-side converter and rotor-side converter. However, connecting a BESS in each back-to-back converter for a complete DFIG-based wind farm is neither cheap nor practical; such study is developed with time-domain simulations [97]. A similar topology is presented in [78], where the study case includes a hybrid system, DFIG, and a diesel generator; the proposed control regulates the loading of the diesel generator to achieve low-specific fuel consumption. The study is also developed with time-domain simulations.

In general, the BESS integration for wind power generation is focused on power management and microgrid stability with hybrid systems, where the time-domain simulation is mostly used as the main analysis tool [71, 78, 97]. In this way, this section is focused on studying the BESS integration to mitigate the SSR in the grid by using the modal impedance and small-signal analysis to characterize the system quantitatively and qualitatively, based on the modes associated with SSR are handled to improve the stability of the system.

The BESS controller and the models involved in this section are explained in Section 2.2.11 and 4.2.

4.2   System Description and Model Validation

The system under study is based on the IEEE First Benchmark Model network for subsynchronous resonance, [94] as shown in Figure 4.1. The complete system without BESS, the parameters, the gains for GSC and RSC controllers, and the models are explained in detail in the previous chapters. The operation of the BESS is based on power management, namely, the BESS storages energy when the wind speed exceeds the rated wind speed of the wind energy conversion system; on the other hand, the BESS delivers energy to the grid when the wind speed is lower than the rated wind speed of the WECS. In that scenario, when the battery is 100% charged, the pitch control is set to deliver the rated power. When the wind speed is less than the rated value, the pitch control is deactivated, and the BESS delivers energy to the grid. Considering the aforementioned, the following assumptions are established: 1) the wind speed is set in such a way to deliver 1 *pu* of mechanical power, 2) the BESS begins with 100% charge, and 3) the battery delivers only active power to the network.
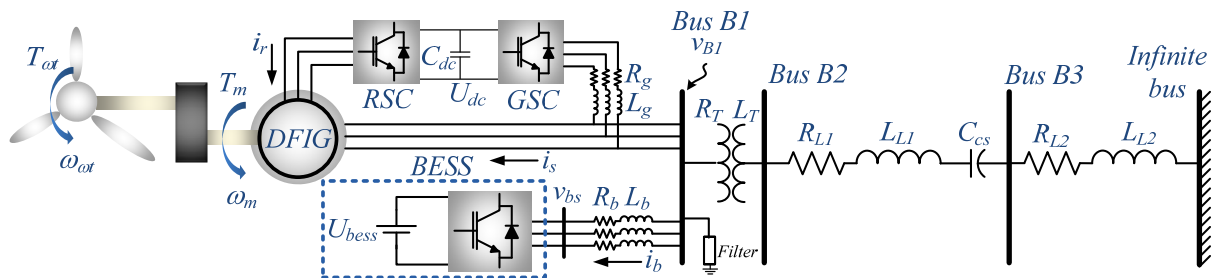

Figure 4.1: Schematic diagram of the DFIG wind turbine with BESS integration.

The series capacitive compensation (C_{cs}) is varied in the percentage of the transmission line reactance. As stated by [9], the degree of series compensation is usually in the 25% to 75% range, but the compensation is often limited to less than 30% due to subsynchronous concerns. In this regard, as several references [1, 92, 98], in this research, the series compensation level is varied from 0 to 100% for analysis purposes.

Controlled state variables as DC-link voltage and rotor speed are depicted in Figure 4.2. The stator and rotor currents in the *dq* frame are depicted in Figure 4.3. In the section one, the RSC controller is activated (which produces the transient), controlling the voltage in bus B1 and the rotor speed. Both figures show the comparison of ODES simulation versus the PSCAD simulation. It can be observed that the evolution of the state variables through the time is almost the same; this validates the ODES.
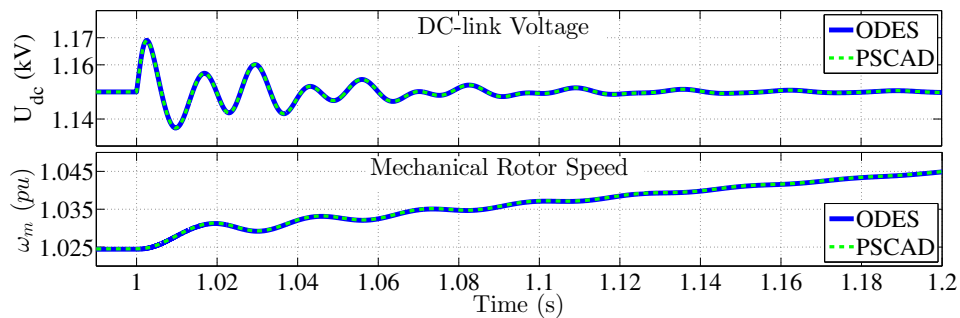
Figure 4.2: DC-link voltage (U_{dc}) and mechanical rotor speed (ω_m), ODES versus PSCAD simulation.
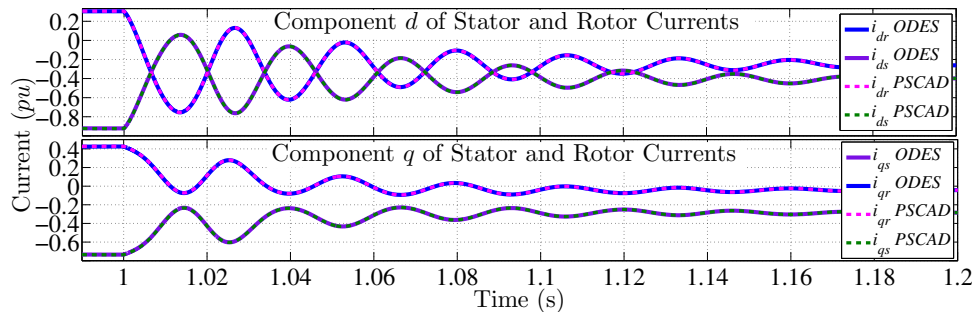
Figure 4.3: Stator current (i_s) and rotor current (i_r) in *dq* frame, ODES versus PSCAD simulation.

The linearization is validated against the nonlinear system. Once the system reaches the steady state, a small disturbance of 1% of its steady-state value is set at 100 seconds, (i.e., the steady-state mechanical rotor speed of the induction generator is 1.02 *pu*, for a small disturbance the rotor speed is changed to 1.0302 *pu* at 100 seconds). Figure 4.4 shows DC-link voltage and the rotor speed, and Figure 4.5 shows the stator and rotor currents of the induction machine in *dq* frame. It can be observed that after the small disturbance both systems, linear system and nonlinear system (ODES), have similar dynamics. In

this sense, the linear system can represent the nonlinear system around the linearization operating point.
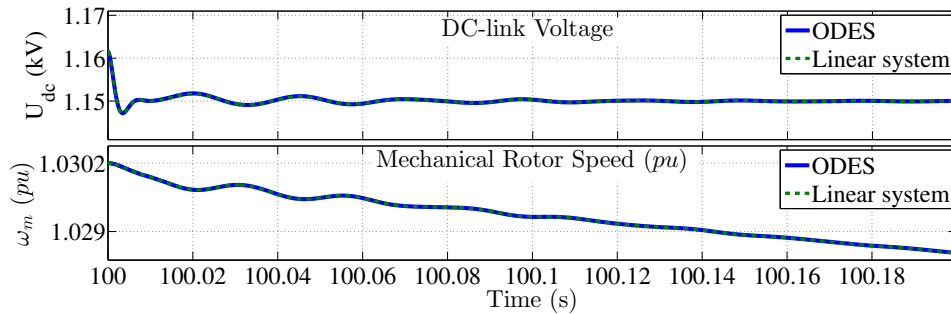
Figure 4.4: DC-link voltage and mechanical rotor speed, linear and nonlinear system.
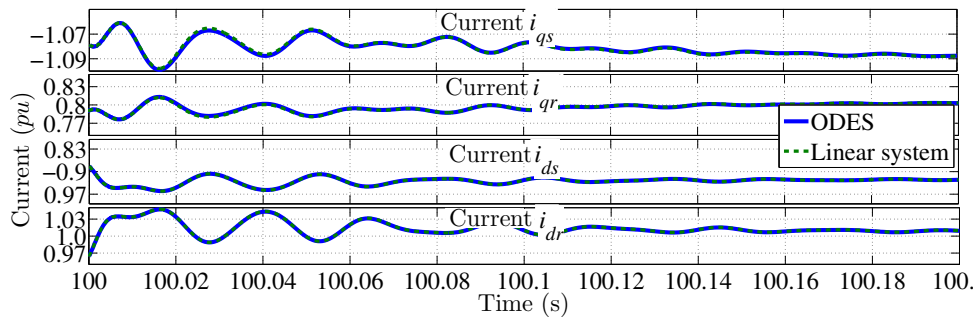
Figure 4.5: Stator current (i_s) and rotor currents (i_r) in dq frame, linear and nonlinear system.

4.3 Dynamic Performance of the System

Dynamic simulation is a helpful tool to show the system behavior qualitatively. Using this tool, the scenario where SSR occurs is shown, the subsynchronous frequency of resonance is investigated as well. Different cases are set to perform the analysis, these cases are called: Base Case, Case A, and Case B. The Base Case is set as follows: with the BESS disabled, the system with series-compensation of 10% is simulated until it reaches the steady state, then a compensation equal to 70% is set. The Case A is assuming the compensation commuting from 10% to 71%, in this case, SSR shows up. The Case B is assuming the compensation commuting from 10% to 71%, with the BESS connected, in this case, the damping action of the BESS is shown. Figure 4.6 shows the dynamic simulation of the cases explained above.

The three cases explained above are simulated, the back-to-back voltage (U_{dc}), electric torque, RMS bus voltage at B1, and active power are plotted in Figures 4.6a, 4.6b, 4.6c, and 4.6d, respectively. The three cases are plotted in each subfigure, and the evolution
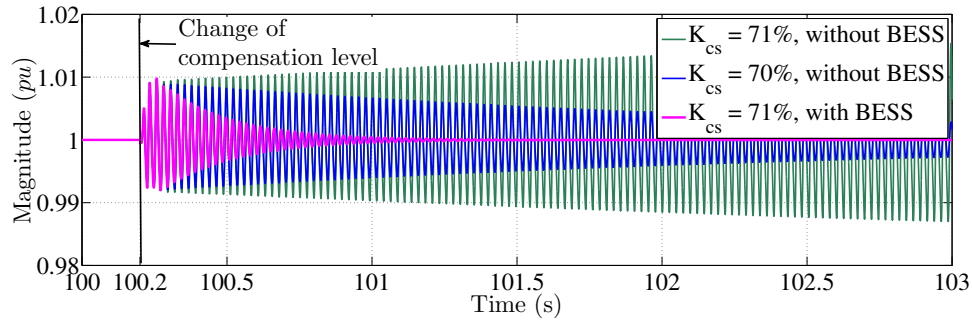
(a) Back-to-Back DC Voltage
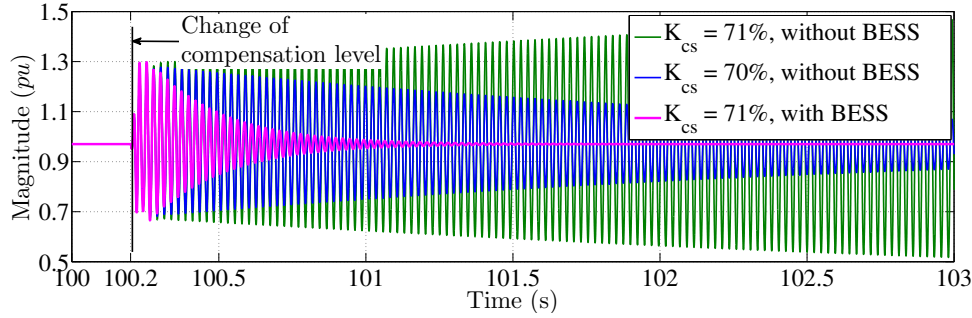
(b) Electric Torque
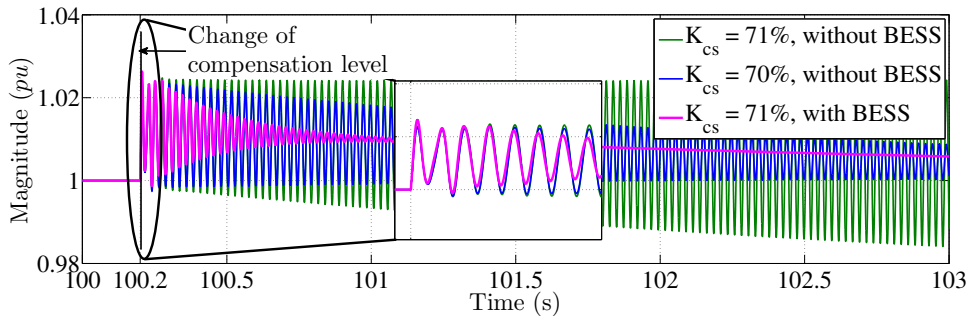
(c) RMS Voltage of bus B1
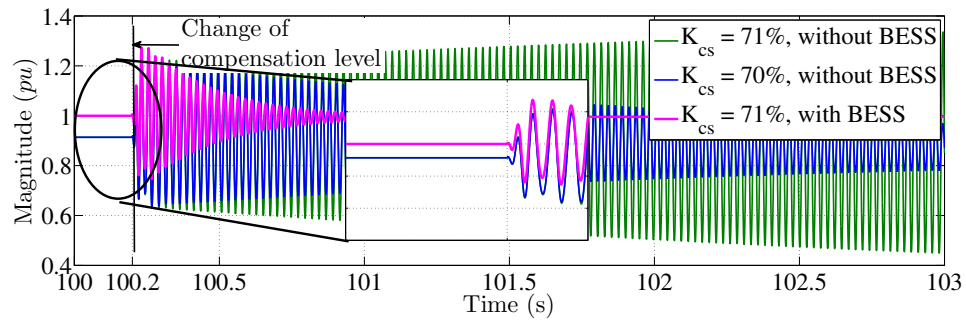
(d) Active Power Delivered to Network

Figure 4.6: Performance comparison of the Base Case, SSO and BESS-action cases. *Compensation limit* is used as framework, simulations through ODES.

of the states variable is similar for each case. Firstly, for a compensation level less than the *compensation limit* (70%), without the BESS and under a small disturbance (made by

a change of series compensation limit), the system is subject to a damped SSO, and the system remains stable after certain time; the quantitative aspect (as damping ratio, oscillation frequency, among others) are described in Section 4.5. Second, a series-compensation level above the *compensation limit* without BESS, 71% for this case, and the system is subject to a small disturbance, the system becomes unstable. Thirdly, a compensation level of 71%, with the BESS connected to bus B1 and under a small disturbance, the system remains stable after a small disturbance.

Figure 4.7 shows the FFT of the electric torque with a subsynchronous dominant component of 41.7 Hz, this means that the SSR phenomenon is due to a frequency around 41.7 Hz. Conforming to the equivalent circuit and the modal impedance technique, in the following section the origin of this subsynchronous component is investigated.
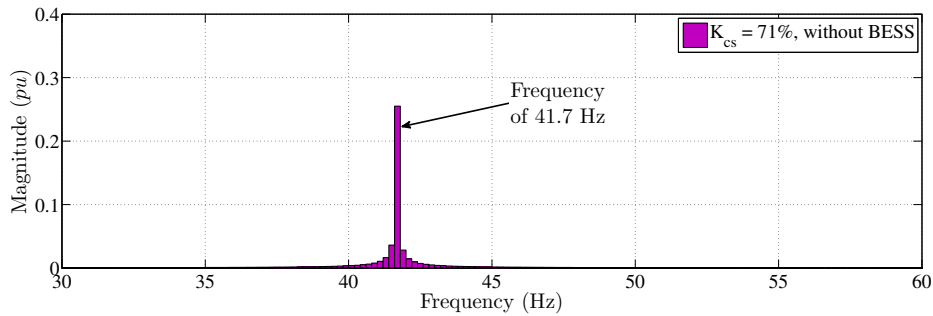
Figure 4.7: Frequency response of the electric torque with compensation of 71%, without BESS, from Figure 4.6b.

4.4 Steady-State Analysis

Figure 4.8 shows the steady-state equivalent circuit of the system under study. X_{lr} and X_{ls} are the rotor and stator leakage reactance. R_r and R_s are the rotor and stator resistances. X_m is the mutual reactance. V_r is the rotor voltage. R_g and X_g (with $X_g = \omega_b L_g$) are the resistance and reactance of GSC, respectively. R_b and X_b (with $X_b = \omega_b L_b$) are the resistance and reactance of the BESS, respectively. The total resistance of the system is $R_{tot} = R_{L1} + R_{L2} + R_T$. The total reactance of the system is $X_{tot} = X_{line} + X_T$. The series compensation is $X_{cs} = K_{cs} X_{line}$.

The steady-state circuit is used to find out the subsynchronous frequencies generated at bus 3 with different series compensation levels. Different techniques can be used for such purpose, for example, the Equation (1.1) can be used, but due to the parallel branches, this equation can not be applied directly. The typical frequency scan (frequency sweep or driving point impedance) could lead to misinterpretation of data due to the effect of the two capacitors can be observed on all the buses. In accordance with the results in the above section, the MI technique can be used to calculate the subsynchronous resonance
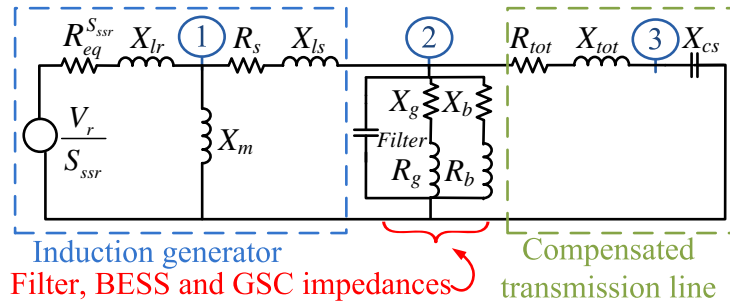
Figure 4.8: Steady-state equivalent circuit of the system.

frequency isolating the effect of each capacitor; the effects of the filter located in bus 2 can be discriminated, showing only the effect caused by the series compensation in the bus 3.

Figure 4.9 shows the natural frequency of the electrical system (f_{er}) and the induced component (f_m) versus series-compensation level of the bus 3 computed by MI technique. Dynamic simulation (performed in Section 4.3) shows that, without the BESS, the SSR is observed with a compensation level larger than 70% (resonance zone). Based on dynamic simulations, the magenta line represents the zone where the SSR can be observed. There are two curves, the solid curve (blue) represents the natural frequency (f_{er}) of the electrical system and the dot curve (green) represents the induced component into the induction generator at frequency f_m. As shown in the previous section, if a turbo-generator mode matches with the induced frequency, the SSR would be caused by the TA phenomenon. In the following sections, the SSSA is performed to find out the behavior of the turbine-generator modes through the sweep of the series-compensation level.
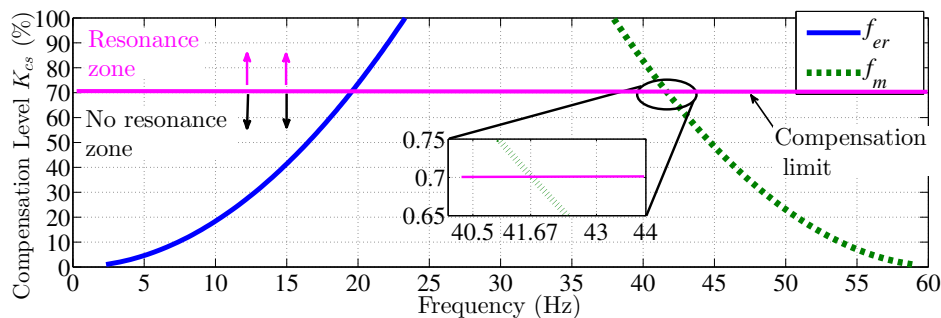
Figure 4.9: Subsynchronous resonance frequency versus series compensation level.

4.5 Small-Signal-Stability Analysis

4.5.1 Small-Signal System

The set of n first order nonlinear ordinary differential equations described in Section 2.2 is linearized in the form:

$$\Delta \dot{x} = A \Delta x \qquad (4.1)$$

where $\Delta \dot{x}$ is the linearized system, Δx linearized state-variable vector, $A = J(X_0) = \frac{\partial f}{\partial x}\big|_{x=X_0}$, with f as the set of differential equations. The small-signal system is build up using MatLab function *fsolve*.

4.5.2 Eigenvalue Analysis and Participation Factors

The linearized equations of the entire system are used to calculate the eigenvalues, and the participation factors analysis is conducted to identify how each state variable contributes in each mode.

The critical eigenvalues are determined as the ones which becomes unstable to the system. Table 4.1 shows the characteristics of the most critical eigenvalues (12 and 13) to profoundly investigate the origin and causes of the observed phenomenon and quantify the BESS support on the stability enhancement, the next analysis is explained. Firstly, the behavior of the dynamic simulation of the three cases explained in the previous sections are reproduced in Table 4.1, the qualitative characteristic of each case is shown. The real part of the eigenvalues shown in the column σ represents the decaying mode for negative, while for positive value represents oscillatory instability. The column f (Hz) shows the oscillation frequency in hertz. The column ζ represents the damping ratio. Finally, in Table 4.1, the Limit Case is added to show the compensation limit of the cases with BESS. Beyond this compensation, the system becomes unstable.

Table 4.1: Modes 12/13, without BESS versus with the BESS. Base Case, system without BESS and $K_{cs} = 10\%$, after steady-state $K_{cs} = 70\%$. Case A, without BESS and $K_{cs} = 71\%$. Case B, with BESS and $K_{cs} = 10\%$, 70%, and 71%. Limit case, with BESS until instability.

		σ	f (Hz)	ζ	D. State/PF
Base	10%	-18.12	38.14	7.538×10^{-3}	Δi_{dr} 7.31
Case	70%	-0.1696	41.68	6.477×10^{-4}	Δi_{dr} 9.03
Case A	71%	0.4385	41.67	-1.675×10^{-3}	Δi_{dr} 8.81
	10%	-19.75	38.26	8.187×10^{-2}	Δi_{dr} 7.50
Case B	70%	-4.701	41.76	1.791×10^{-2}	Δi_{dr} 10.6
	71%	-4.038	41.76	1.539×10^{-2}	Δi_{dr} 10.3
Limit	77.7%	-0.01894	41.67	7.234×10^{-5}	Δi_{dr} 8.59
Case	77.8%	0.03604	41.67	-1.376×10^{-4}	Δi_{dr} 8.57

According to the Table 4.1, in Base Case the system remains stable until 70% of series-compensation with $\sigma = -0.1696$ rad/s, and an oscillation frequency of 41.68 Hz. In Case A, with compensation of 71%, the system becomes unstable with $\sigma = 0.4385$ rad/s and the oscillation frequency of 41.67 Hz; this frequency is approximately the same than the analysis performed by MI and dynamic simulation. The Case B incorporates the BESS to the system. It is shown the same series-compensation levels than the Base Case and Case A. It can be seen that for 10% of series-compensation, σ is improved from -18.12 to -19.75; for 70% of series-compensation level, σ is improved from -0.1695 to -4.701, while for 71% of series-compensation level, σ is improved from 0.4385 to -4.038. In the three scenarios the damped effect of the BESS is confirmed.

In the ζ column, the same damping effects can be observed, where an oscillatory instability is represented by a negative value of $-1.675e^{-3}$. On the other hand, the frequency in the Case B is shifted (compared with the Base Case and Case A) slightly, but enough to avoid the resonance zone.

The last column, dominant state variable and participation factor (D. State/PF), shows the state variable with highest participation factor (dimensionless value, not normalized) in the mode, which corresponds to the component d of the rotor current.

The Limit Case, in Table 4.1, shows the compensation limit of the BESS of 77.7%. The real part of the eigenvalue ($\sigma = -0.01894$) is close to zero, its frequency of oscillation is 41.67 Hz, as the Case A, and the damping ratio is close to zero. For a series-compensation level of 77.8% the systems become unstable even with BESS integration.

Conforming to the previous explanation, the modes which produces SSR are the modes 12/13. In this sense and according the PF, the state variables associated with SSR belong to the rotor current of the induction generator. Figure 4.10 shows the matrix of the participation factors and in it can be observed the group of state variables associated to the critical mode 12/13 and the state variables 4 to 7, pointed out in the figure, belong to the induction generator model, as a result, the group of participation factors can be associated to SSR can be identified.

Figure 4.11 shows the evolution of the main modes with a sweep of the series-compensation level from 0% to 100%. The comparison is made with and without the BESS; the modes traced in each subfigure correspond to the modes involved in SSR. The identification process for each mode is explained in Section 3.6 of this investigation. Modes 8/9 and 10/11 are the modes corresponding to the induced modes by the series compensation calculated by small-signal analysis. Modes 12/13 correspond to the electromechanical mode. Modes 16/17 correspond to purely mechanical mode and it is constant in the four cases with $\lambda_{16/17} = -63.9 \pm j11.7$.

Figure 4.11a shows the variation of the eigenvalues frequency concerning of the compensation level without the BESS. The interaction occurs when subsynchronous induced mode falls and is close to the electromechanical mode. It should be noted that the modes called *SupSR Elec Mode* and *SSR Elec Mode* are calculated using MI analysis; modes 8/9 and 10/11 are equivalent respectively, but these are calculated using small-signal analysis.
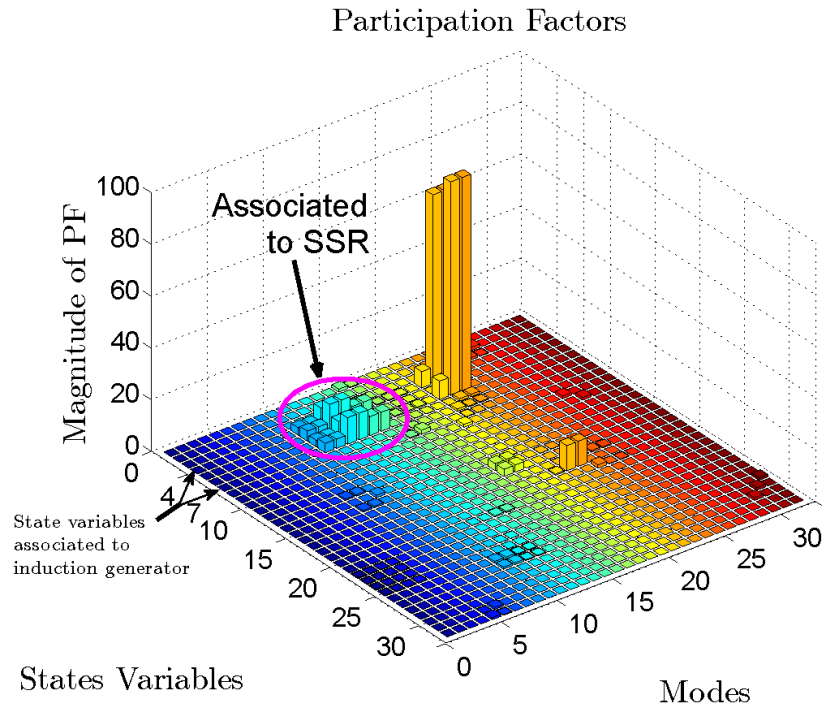
Figure 4.10: Participation factors matrix for Base Case with 10% of compensation.

In this sense, after the compensation level of 71%, the electromechanical mode and modes 10/11 are close enough to produce SSR, and they keep getting closer.

Figure 4.11b shows the variation of the eigenvalues real part versus the compensation level without BESS. According to the participation factors, the dominant state is pointed out in each trace. In this sense, the stator currents are the dominant states in the induced modes; this is consistent because the SSR phenomenon is induced through the stator-rotor windings. On the other hand, the electromechanical mode changes its real part from negative to positive in approximately 70% of the compensation level; its dominant state variable is the rotor current.

Figure 4.11c shows the frequency of the same modes as Figure 4.11a computed by small-signal analysis, but with the BESS integration; there is a slight change in the imaginary part of the eigenvalues due to the BESS action indicated by the resonance zone which is reduced (vertical red line). Figure 4.11d shows the real part plotted with respect to the compensation level with BESS. The damping improvement can be observed in the real part of the electromechanical mode, where its real part changes from negative to positive on 77.7% of compensation level, this is an increase of 7.7% of series-compensation level for the system becomes unstable.

Figure 4.12 shows only the modes 10/11 and 12/13 involved in SSR phenomenon. The imaginary part shows the frequency change of the same modes for the two cases, with and without BESS. The dotted line corresponds to the induced mode 10/11 (subsynchronous
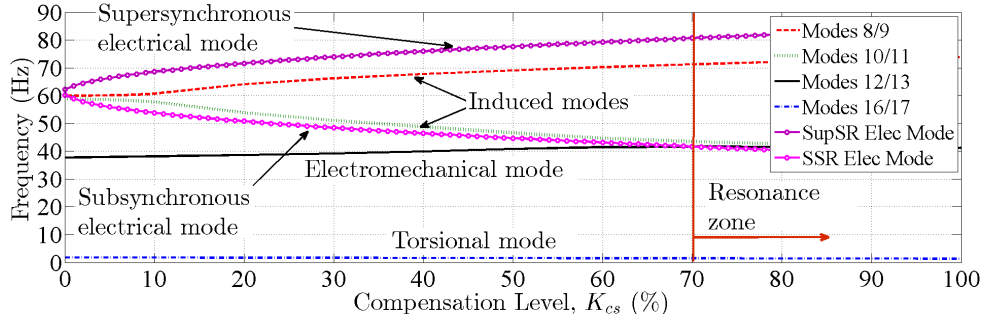
(a) Variation of the frequency for the main eigenvalues without BESS.
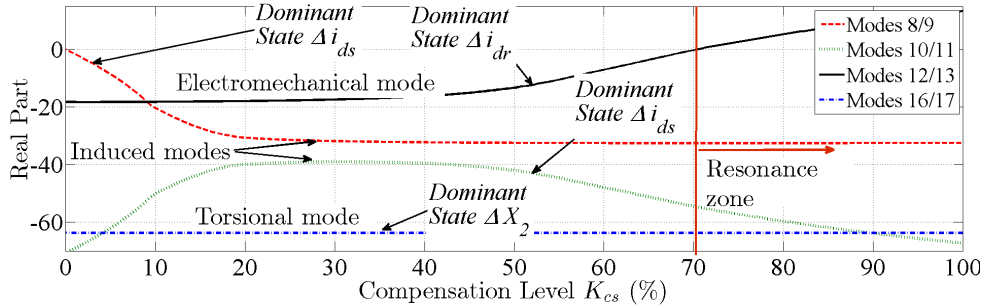
(b) Variation of the real part for the main eigenvalues without BESS.
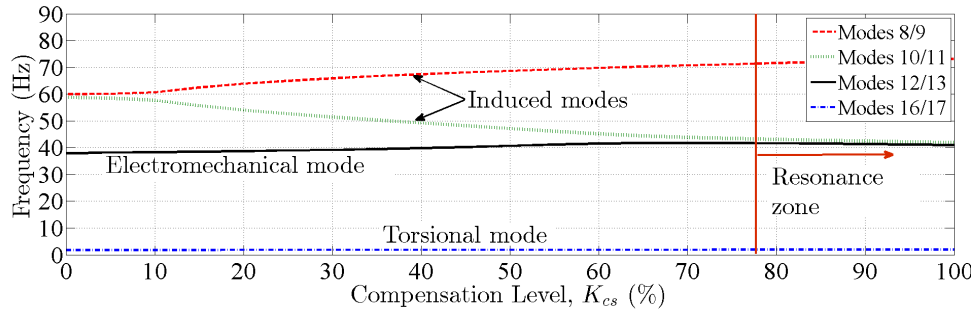
(c) Variation of the frequency for the main eigenvalues with BESS.
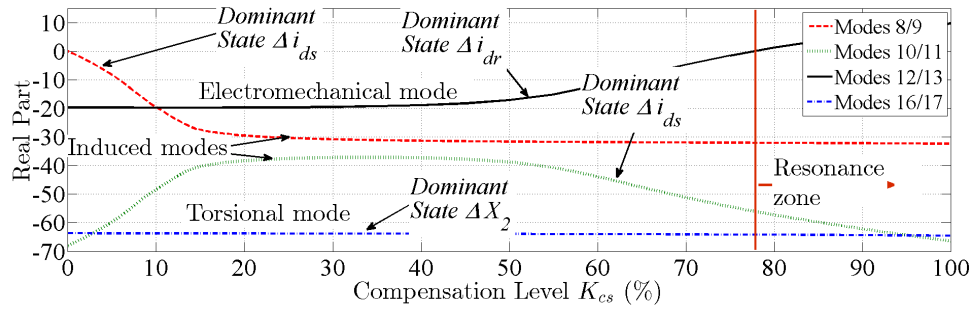
(d) Variation of the real part for the main eigenvalues with BESS.

Figure 4.11: Variation of the real part and frequency of the main eigenvalues with respect to the percentage of series compensation, without and with BESS.

induced mode) with BESS, and the solid line is the same mode, but without BESS. It can be seen that the frequency change because of the BESS is 0.4 Hz. The modes 12/13

(electromechanical mode) for the imaginary part do not show a relevant modification. The above means, for a slight frequency change, the system increases the compensation level by 7.7% respect to the case without BESS.
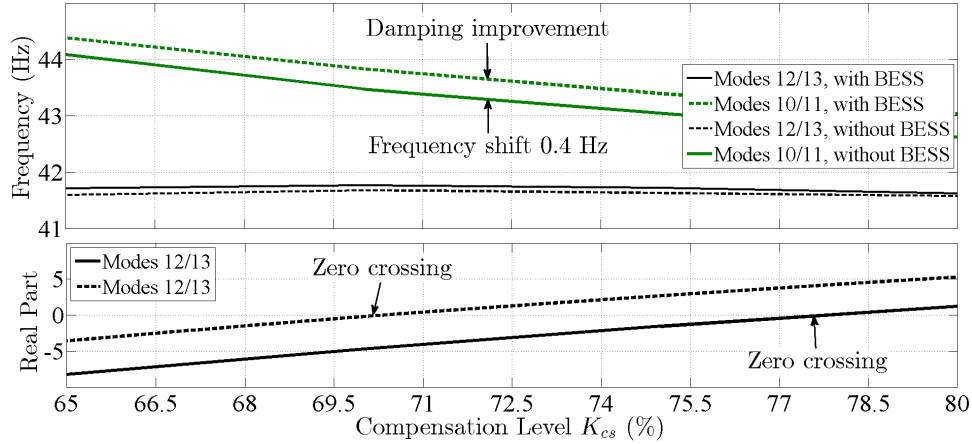
Figure 4.12: Modes involving SSR, with BESS and without BESS.

Table 4.2 shows the relation between modes and participation factors (in percentage). The modes shown in this table are the ones involved in SSR. It is shown the case with a compensation level of 10% with and without BESS. Contrasting the case with BESS, and the case without BESS, the modes show similar participation of the states, e.g., modes 12/13 show the same state variables with a similar percentage of participation. According to above and Table 4.2, modes 8/9 are mainly associated with the induction generator and the series capacitor voltage. Modes 10/11 are mostly associated with the state variables of the induction generator. Modes 12/13 are mostly associated with the induction generator; the component d of the rotor and component d of the stator participate with almost 80% of the mode in both cases. Modes 16/17 are mainly associated with the induction generator and electrical filter for the RSC. Once knowing the contribution of the state variables into the main modes involving SSR, the sensitivity analysis is required to give a quantitative analysis of which parameter should be modified to improve the stability.

4.5.3 Eigenvalue Sensitivity

Eigenvalue sensitivity, defined as the rate of change and direction of eigenvalue movement in the s-plane due to the variation in system parameters, it is an efficient tool for designing the control system [62].

As stated by [65], the mathematical definition of eigenvalue sensitivity is:

$$\frac{\partial \lambda_i}{\partial a_{k,j}} = \psi_{i,k} \phi_{j,i} \tag{4.2}$$

Table 4.2: Modes and participation factors, with $K_{cs} = 10\%$, with and without BESS.

| Modes | *PF* | Participation Factors | |
		Case without BESS (%)	Case with BESS (%)
$\lambda_{8/9}$	Δi_{qs}	19.9	19.8
	Δi_{ds}	26.6	26.8
	Δi_{qr}	17.8	17.7
	Δi_{dr}	24.8	24.9
	ΔV_{dcs}	5.1	5.1
	ΔV_{qcs}	5.1	5.2
$\lambda_{10/11}$	Δi_{qs}	20.2	20.1
	Δi_{ds}	30.4	30.5
	Δi_{qr}	18.2	18.1
	Δi_{dr}	28.7	28.8
$\lambda_{12/13}$	Δi_{qs}	8.9	8.6
	Δi_{ds}	38.2	38.5
	Δi_{qr}	8.3	8.1
	Δi_{dr}	41.4	41.6
$\lambda_{16/17}$	Δi_{qs}	5.5	5.6
	Δi_{ds}	1.4	1.6
	Δi_{qr}	6.9	7.1
	Δi_{dr}	1.5	1.8
	ΔX_1	41.4	40.1
	ΔX_2	42.4	42.0

where i is the eigenvalue of interest, k and j are the row and column of the Jacobian matrix, and a is the element of the Jacobian matrix. Thus the sensitivity is defined as the product of the left and the right eigenvector. An easy expression for (4.2) can be defined to better manage the eigenvalue sensitivity: $S^i_{k,j} = \psi_{i,k} \phi_{j,i}$. Where S is the sensitivity matrix.

To achieve improvement of damping characteristic of the system due to adverse consequences of series compensation, it is required to enhance the critical eigenvalue moving the eigenvalue to the left side in the $s-$plane. According to the above results, the critical eigenvalues that produce SSR are $\lambda_{12/13}$. In this case, the sensitivity matrix $S^{12/13}$ is computed but only the higher sensitivity value and its relation with the linearized state of the Jacobian matrix ($A = J(X_0) = \frac{\partial f}{\partial x} |_{x=X_0}$) is analyzed.

Case B with compensation of 10% is used to calculate the sensitivity matrix $S^{12/13}$ for the eigenvalue $\lambda_{12/13}$. Figure 4.13 shows the complete sensitivity matrix. In this case the maximum eigenvalue sensitivity is found in row 7 and column 7, $S^{12/13}_{7,7}$. The Equation (4.2) can be re-expressed as follows:

$$\frac{\Delta \lambda_{12/13}}{\Delta a_{7,7}} \approx S^{12/13}_{7,7} \tag{4.3}$$

Then, a general expression can be used to estimate the movement of the eigenvalue $\lambda_{12/13}$ toward right or left side in the s-plane depending on the parameter variation. Taking $\Delta a_{7,7} \approx a_{7,7}^n - a_{7,7}^0$, where $a_{7,7}^0$ is the corresponding value of $a_{7,7}$ of the Jacobian matrix for Case B with 10% of compensation and $a_{7,7}^n$ is the expected value of $a_{7,7}$. Similar consideration is made for $\lambda_{12/13}$. In this sense, from Equation (4.3) the following equation is obtained:

$$\lambda_{12/13}^n \approx \lambda_{12/13}^0 + S_{7,7}^{12/13}(a_{7,7}^n - a_{7,7}^0) \tag{4.4}$$

For this particular case, it is desired that $\lambda_{12/13}^n$ shift toward left side of s-plane. With $\lambda_{12/13}^0 = -19.749 \pm j240.408$ and $S_{7,7}^{12/13} = 7.474 + j0.6155$, the parameter $a_{7,7}$ of the A matrix is a real number. In this sense, the result of $(a_{7,7}^n - a_{7,7}^0)$ must be negative. Conforming to the mathematical model of the induction generator, the corresponding partial derivative of the term $a_{7,7}$ of the A matrix is:

$$a_{7,7} = D\left(R_r L_s - L_s \frac{\partial v_{dr}}{\partial i_{dr}}\right) \tag{4.5}$$

where all the quantities in $a_{7,7}$ are in pu, $D = \omega_b/(L_m^2 - L_r L_s)$ and the partial derivative $\frac{\partial v_{dr}}{\partial i_{dr}}$ is calculated numerically through MatLab/Simulink. In this sense, for each case $a_{7,7}^n$ and $a_{7,7}^0$ are defined as Equation (4.5).
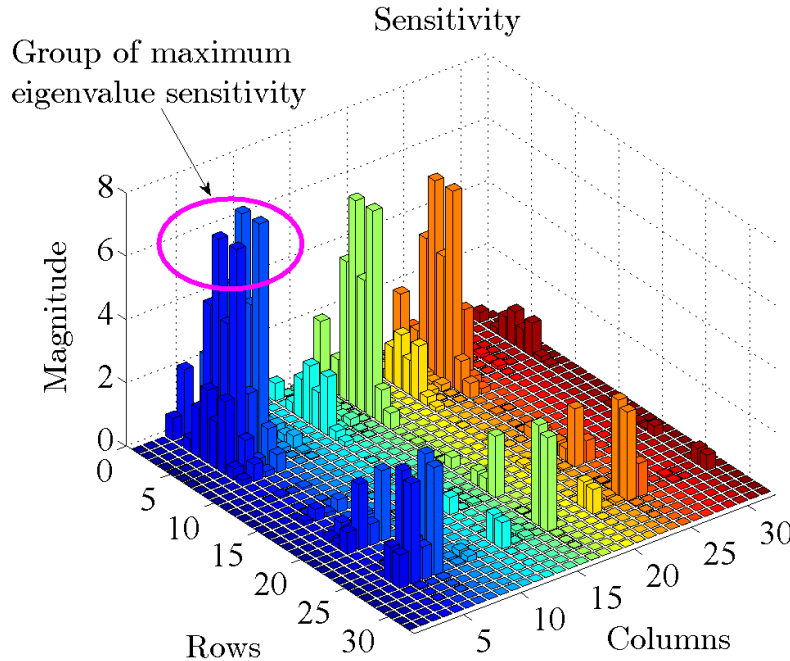

Figure 4.13: Sensitivity matrix for Case B with 10% of compensation level, $S^{12/13}$.

In accordance with the definition of eigenvalue sensitivity, if the parameters in $a_{7,7}^n$ are changed, such that the condition $(a_{7,7}^n - a_{7,7}^0) < 0$ is fulfilled, the damping characteristic

of $\lambda_{12/13}$ is improved. In this context, if the parameter R_r is increased, the condition $(a_{7,7}^n - a_{7,7}^0) < 0$ is fulfilled and $\lambda_{12/13}$ move to the left in the s-plane.

Hence, the damping characteristic $\lambda_{12/13}$ can be improved by modifying the parameters R_r, L_s, L_r or any parameter or gain of the control signal v_{dr}, as well as the system stability can be improved. It is evident due to parameter variation that several eigenvalues could be affected; the aim is to improve the critical eigenvalue without major affectation on the rest of the eigenvalues.

Figure 4.14 shows the comparative of $\lambda_{12/13}$ with different values of L_r and K_{Pidr} versus compensation levels. It is worth of mentioning that parameter L_r is used in the control signal v_{dr}, then its sensitivity is of major concern. The solid curve (black curve) shows the Base Case without BESS, the dash curve (magenta curve) shows the Base Case with BESS, the dot curve (blue curve) shows the Base Case with ΔK_{Pidr} of 1×10^{-2} to 1×10^{-3} and the dot-dash curve (green curve) shows the Case Base with ΔL_{lr} of 0.16 pu to 0.18 *pu* Similar result is observed under a variation of L_{ls} as the dot-dash curve. According to above analysis, the major eigenvalue sensitivity of the critical eigenvalue ($\lambda_{12/13}$) are in the parameters L_{lr} and L_{ls}. In general, it is possible to improve the damping of the system using the eigenvalue sensitivity analysis through the modification of the parameters involved in the SSR phenomenon.
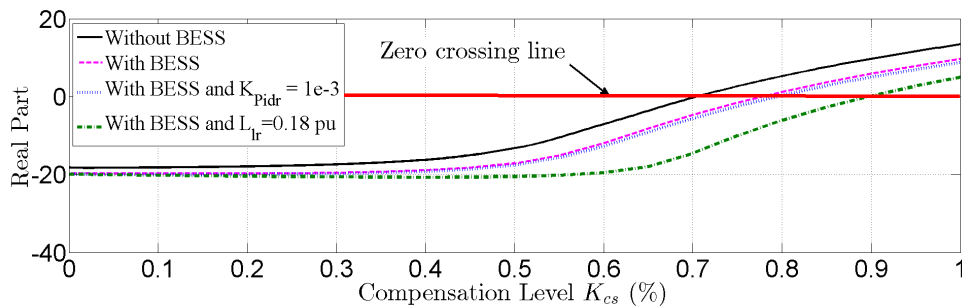
Figure 4.14: Comparative of parameters variations of the real part of the electromechanical mode, computed by ODES.

4.6 Chapter Discussion

The BESS integration in a system is a subject that is taking more importance due to its ability to compensate for active power and to improve the frequency of a system or microgrid. In this analysis, the BESS shows excellent performance to mitigate the SSR while is compensating active power in the DFIG-based WECS.

The participation factors indicate two main conclusions. The first one is that in the process of SSR due to a series-compensated transmission line, the interaction is mainly with the induction generator model. The second one is that the BESS integration does not modify the interaction process of the series-compensated transmission line with the

induction generator. In this context, the participation factor indicates that the rotor currents are always involved in the SSR issues. Thus, a solution for this problem can be to modify the rotor currents; which is proposed in the next chapter.

Using the modal analysis, the critical modes are determined and it is demonstrated that the resonance zone is reduced due to the active power injection. Conforming to the investigation, the injection of active power to the system modifies the bandwidth of the subsynchronous induced mode which produces the mode that makes the system unstable change, reducing the resonance zone. In other words, the injection of active power does not modify the model that makes the system unstable, instead modify the induced mode.

Finally, an extra improvement is achieved by the eigenvalue sensitivity. In this scenario, it is indicated the parameters can be modified to improve the stability of the system under an SSR condition without affecting the other modes. The best improvement is achieved by modifying the rotor leakage inductance; which matches with the participation factors analysis.

Proposed Controller Scheme to Mitigate SSR Issues

5.1 Introduction

In this section, the proposed mitigation scheme (PMS) is integrated into the BESS control and is analyzed for SSR issues in a DFIG-based wind farm. The main idea of the PMS lies in isolating the source that produces resonance with the part that interacts, in this case, with the induction generator, as was demonstrated with the participation factors and eigenvalue sensitivity analysis in the previous chapter.

5.2 System Description

The BESS is modeled as was described in Sections 2.2.7 and 2.2.11; in that sections, the control law is explained. The purpose of the PMS is to focus on the compensation of the current that produces SSR and the other control scheme is focuses on active power management (the reactive power control is deactivated).

5.3 Proposed Mitigation Scheme (PMS)

Figure 5.1 shows the BESS control scheme with the auxiliary signals i_{dh} and i_{qh} pointed out inside of a blue box. According to the disturbance detected, in this case TA, the main idea lies in mitigating the subharmonic currents induced in the induction machine, which are the origin of the undamped oscillations. These signals are calculated from the line current, which is $i_l = i_s + i_g + i_b$. Figure 5.2 shows the simplified system of study, where the location of the currents of interest are shown; the current signal of interest (i_l) is between the filter and the node where the currents of the back-to-back converter, DFIG, and the BESS join. Figure 5.3 shows the manipulation of the measured currents from

the line (for each phase i_{la}, i_{lb}, and i_{lc}), where the three-phase signals are transformed in a *dq* synchronously-oriented reference frame (θ), then a second-order transfer function is applied to decouple the low frequencies of the current from the frequencies above the fundamental frequency. In this sense, i_{dqf} represents the i_{df} and i_{qf} currents correspond to the fundamental frequency. The remaining current signals i_{dqh} (i.e. i_{dh} and i_{qh}), represent the remaining components from frequencies below to the fundamental frequency.
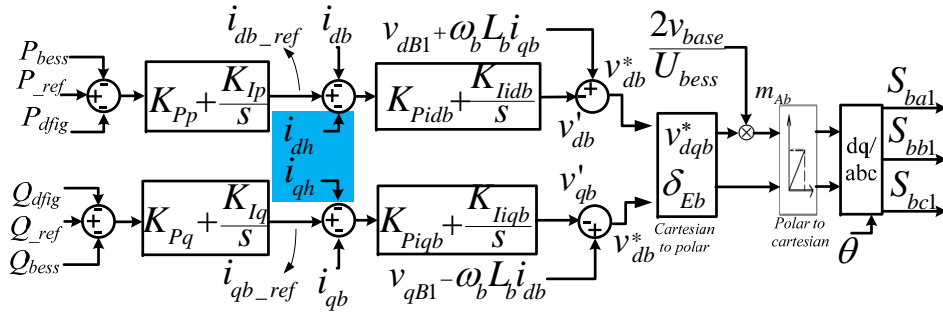
Figure 5.1: BESS scheme control with proposed loop controller.
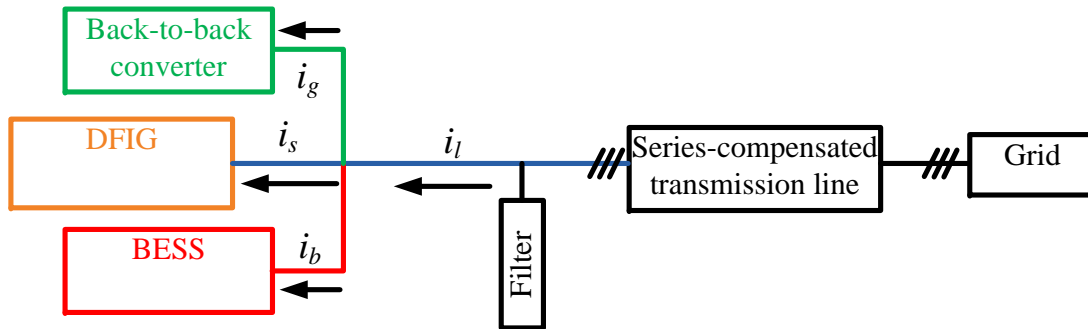
Figure 5.2: Simplified system showing the measured auxiliary signal.
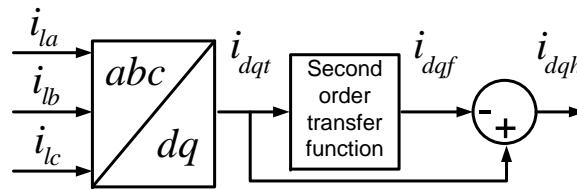
Figure 5.3: Proposed mitigation scheme for the auxiliary loops.

The signals i_{dh} and i_{qh} are added as feedback in the inner current loop of the BESS scheme control. The second order transfer function is defined as follows:

$$\frac{i_{dqf}}{i_{dqt}} = \frac{\omega_p^2}{s^2 + 2\zeta_p\omega_p s + \omega_p^2} \tag{5.1}$$

where $\zeta_p = 0.7$ is the damping ratio and $\omega_p = (4)(2)(\pi)$ is the characteristic frequency. Figure 5.4 shows the Bode diagram of the second-order transfer function; it is observed that the phase margin is infinite and the gain margin is infinite.
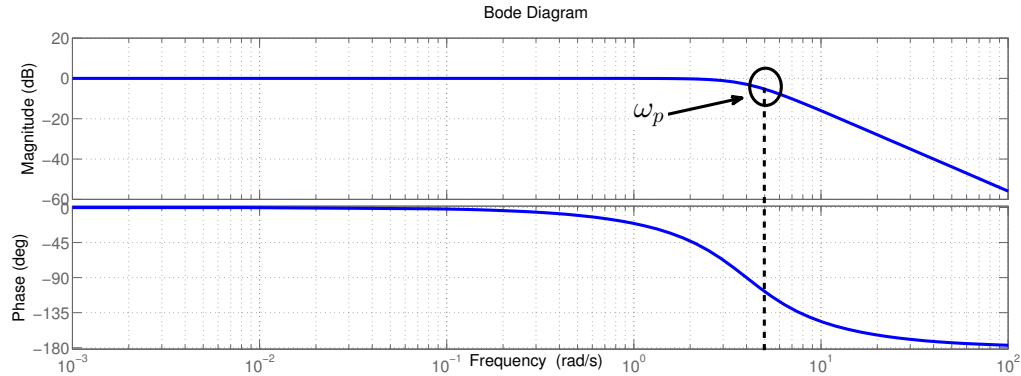
Figure 5.4: Bode diagram of the proposed second order transfer function.

Besides, in consonance with the main idea of the proposed mitigation scheme, the frame dq and the second-order transfer function makes $i_{df} \approx constant$ and $i_{qf} \approx constant$ for a steady-state operation. Otherwise, if harmonics components are included in the current i_l, the signals i_{dh} and i_{qh} will oscillate due to low frequencies, in this case, produced by TA. In this scenario, the filtered signal (i_{dqf}) and the control signals (i_{dqh}) will not produce a magnitude amplification or a phase swift, conforming to the Bode diagram.

Following the explained above, the subharmonic components produced by a small disturbance will be compensated by the controller of the BESS avoiding the interaction with the induction generator.

5.4 Dynamic Performance of the System with the PMS

In this section, the dynamic simulation is performed and three cases are assessed to show the dynamic characteristic of the proposed scheme that minimizes or mitigates the SSR effect. At the beginning of the simulation and until the system reaches a steady-state, the series compensation for the three cases is 10%, then according to the previous section, the system with the BESS becomes unstable at 78% of series compensation. In this context, for the simulation in this section, the series compensation switches from 10% to 78% for the following three cases:

1. The first case comprises the system without BESS.
2. The second case comprises the system with the BESS, only with the active power compensation (APC) stage.

3. The third case comprises the system with the BESS, the APC plus the proposed mitigation scheme (PMS) shown in Figures 5.1 and 5.3.

The general configuration of the system comprises the following statements. The BESS integration is after the system reaches its steady-state, at 90 seconds. In the third case, the PMS is activated at the same time as the active power compensation, at 90 seconds. The small disturbance is set at 100.3 seconds.

Figure 5.5 shows the behavior of the three cases described above. The displayed figures are the back-to-back DC-voltage on Figure 5.5a, the electric torque of the generator on Figure 5.5b, the voltage on the bus B1 on Figure 5.5c, and the active power delivered to the network 5.5d. The blue line shows the case without BESS, the green line shows the case with BESS with the active power compensation control, and the red line shows the case with active power compensation plus the PMS controls. It can be observed that the system becomes unstable for case 1, the system shows sustained oscillations for case 2, and the system shows damping oscillations for case 3. In this context, the dynamic simulation shows an enhancement in the stability for this particular scenario.

The previous dynamic simulation indicates that the BESS can be used as a multi-task device, in this sense, the compensation of active power can be done, as well as the PMS can be applied to solve SSR issues. In this scenario, the effect of only the PMS control in the system is investigated. In the following dynamic simulations, the DC voltage and the active-reactive powers of the back-to-back converter are only shown due to that the state variables behave similarly; as shown in Figure 5.5. The series compensation remains similar to the previous cases; 10% to 78%.

Figure 5.6 shows two cases, the dynamic simulation with only the PMS and the case with the APC plus PMS, it is performed to demonstrate the effect of the active power control and the action of the PMS on the system. The three figures maintain the following pattern, the blue line is the response with only the PMS control and the red line is the response with the APC plus PMS. Figure 5.6a shows the back-to-back converter DC voltage, it can be observed that the dynamic response is similar for the two cases. Figure 5.6b shows the total active power delivered to the network, it can be observed two behaviors, the dynamic response is similar for the two cases and there is a difference in magnitude due to the active power delivered to the network. Figure 5.6c shows the active and reactive power required by the BESS to mitigate the SSR issue with only the action of the PMS. In conclusion, the PMS achieves its objective without the aid of the APC, and the two schemes can work individually or together to achieve their goal without any trouble between them. Besides, in this scenario, the component of subsynchronous frequency which produces the SSR can be mitigated and the required active and reactive power required for such purposes is finite, as it can be seen, both powers remain zero after a couple of seconds, which helps to avoid the oversizing of the batteries bench.

5.5 Small-Signal-Stability Analysis with the PMS

The aims of the SSS analysis are to show the critical eigenvalues which become the system unstable and to determine how the eigenvalues changes due to the PMS control. In general, in this section, the qualitative characteristics of the system are investigated.

Figure 5.7 shows the eigenvalues involved in the SSR issues (identified in Section 3.6), for two cases, the first case is the BESS connected to the system with only the PMS (Figures 5.7a and 5.7b) and the second case is the BESS with the APC plus the PMS (Figures 5.7c and 5.7d). Where **Sup Ind** refers to the supersynchronous induced mode, **Sub Ind** refers to the subsynchronous induced mode, **EM** refers to the electromechanical mode, and **Mech** refers to the mechanical mode. The eigenvalues are evaluated with a sweep in series compensation from 0% to 100%.

It is shown the frequency and the real part for each case. Despite the compensation level, the system remains stable, it can be observed in the real part of the figures since is always negative, besides the **frequency gap of SSR** of 2 Hz described in Section 3.6.2 is not overcome as it can be seen in the figures of frequency, where the first case shows a difference of 44.95 Hz - 42.14 Hz = 2.81 Hz and for the second case the difference is 45.01 Hz - 42.25 Hz = 2.76 Hz.

It can be concluded that the PMS dominates the dynamic response of the system due to the differences in the evolution of the real part and the frequency for each case remains almost equal for the two cases. In this sense, the dynamic simulation end eigenvalue analysis confirms that the APC and the PMS can work individually and even together without any trouble.

Figure 5.8 shows the subsynchronous induced and the electromechanical modes for three cases, the first case is when the BESS is not integrated into the system, the second case is when the BESS is integrated to the system with only the APC, the third case is when the BESS is integrated into the system with only the PMS. The four figures include the black line, which is the mode without BESS, the blue line the mode with only APC, and the green line the mode with only PMS.

Figure 5.8a shows the frequency related to the subsynchronous induced modes, in this case, there is no remarkable change in the modes related to the system without BESS and with only APC. While the mode with only the PMS shows a change with respect to the other two modes as the compensation level increase. The real part of the subsynchronous induced modes (Figure 5.8b) indicates that the effect of the PMS almost produces a change from a negative to positive as the series compensation increase, but there is not a positive real part reached for any mode.

On the other hand, Figure 5.8c shows the frequency of the electromechanical mode for the three cases; without BESS, with only APC, and PMS. In this figure, it is observed that in the resonance zone (described in the previous chapter) around $K_{cs} = 78\%$ the frequency oscillate between 40 Hz and 42 Hz which is near to the frequency of subsynchronous resonance. While Figure 5.8d shows the real part of the electromechanical modes, it can

be observed an improvement on the mode with only PMS in such a way that, the system overcomes the resonance zone observed on the other two modes.

5.6 Chapter Discussion

The series compensation level in real scenarios is about 30%, the cases analyzed in this chapter consider a range from 0% to 100% to show the boundaries of the mitigation schemes. In this particular case, the torque amplification is the phenomenon that produces SSR (as it is explained in Section 3.6.3), in this context, the resulting SSR is due to harmonics of current that is induced in the stator windings of the induction generator. As it is shown in this chapter, the PMS can compensate for those current harmonics in any scenario isolating the generation part from the transmission part of the subsynchronous components of current.

The BESS can be used as a multitask device, in this Thesis the BESS is used with two schemes, subsynchronous harmonic compensation, and active power control. The two schemes can be applied at the same time or individually without any trouble. It is demonstrated that the energy required to mitigate the current harmonic is finite, namely after the transient, the BESS stops injecting current harmonics.
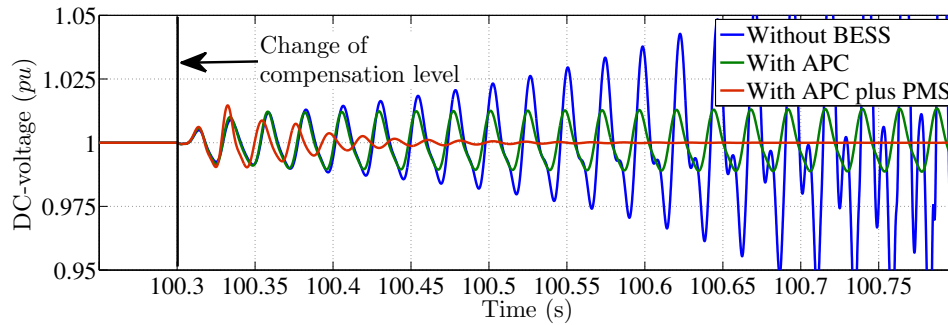
(a) Back-to-Back dc-Voltage
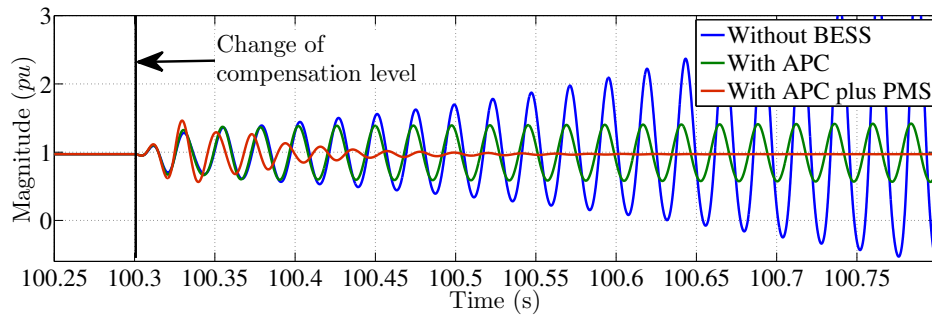
(b) Electric Torque
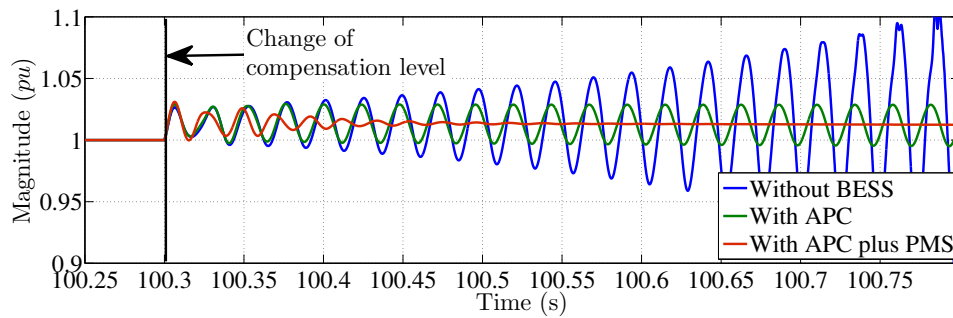
(c) Voltage of bus B1
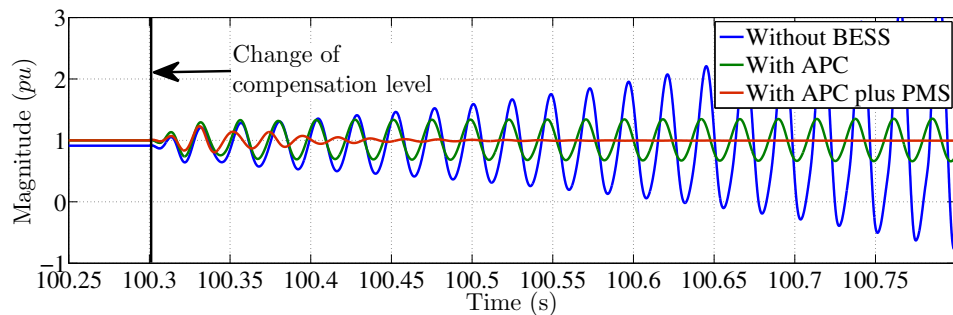
(d) Active Power Delivered to the Network

Figure 5.5: Performance of the system assessed by dynamic simulation of the three cases, without BESS, with APC, and with BESS-PMS.
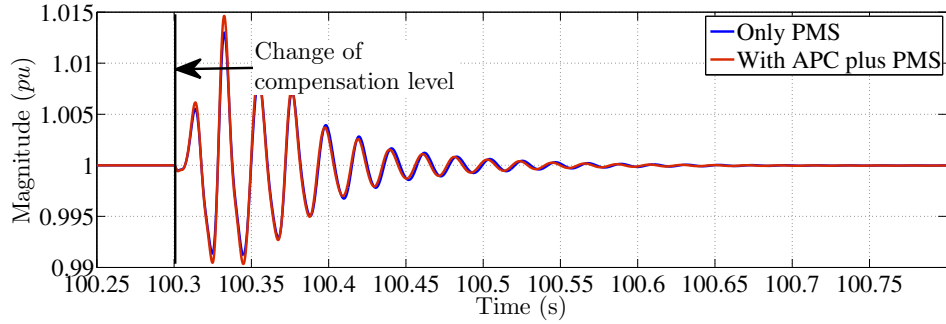
(a) Back-to-Back DC-Voltage
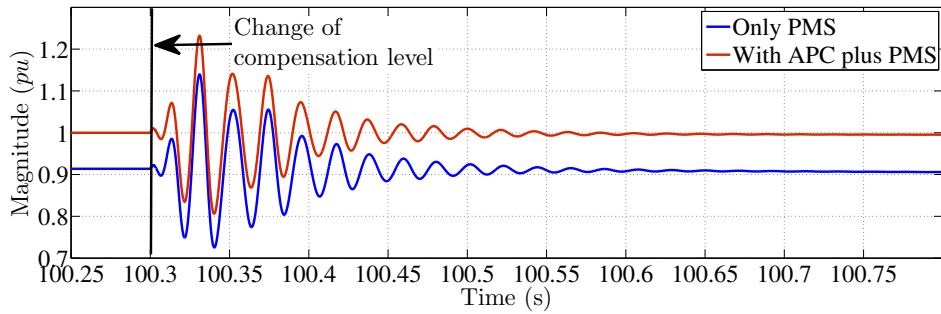
(b) Total active power
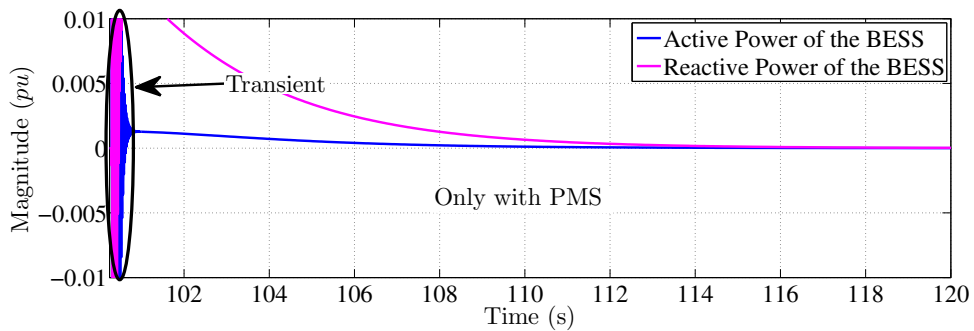
(c) Active and reactive power of the BESS for only the PMS

Figure 5.6: Performance of the system with the APC-PMS compared to only the PMS control.
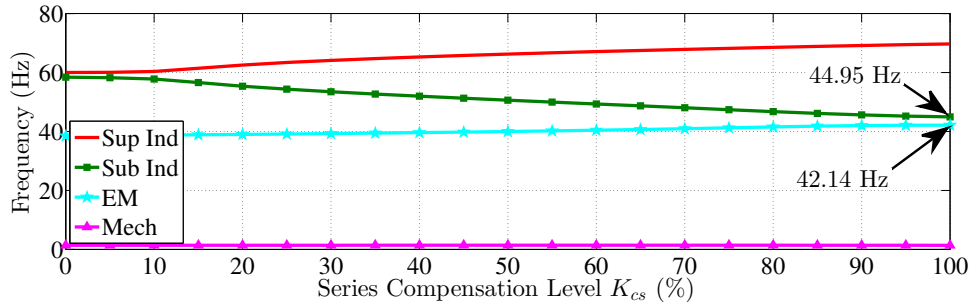
(a) Variation of the frequency for the eigenvalues involved in SSR with only PMS.
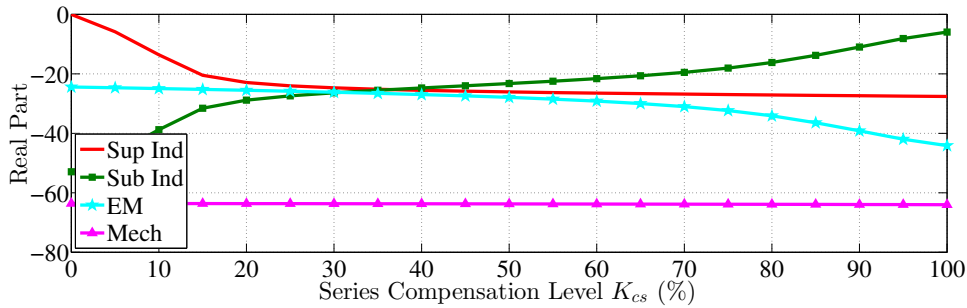
(b) Variation of the real part for the eigenvalues involved in SSR with only PMS.
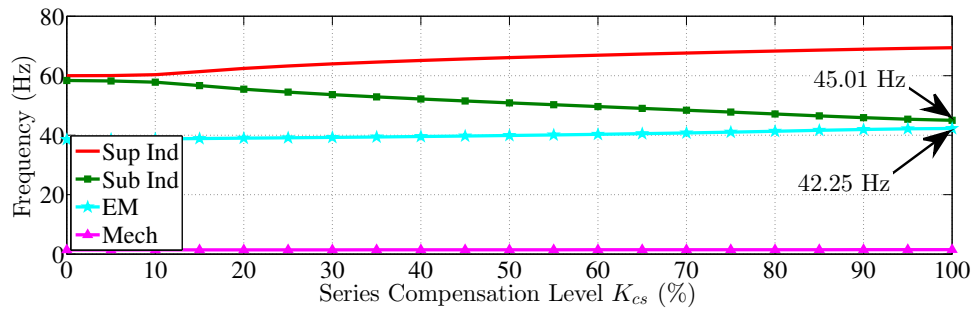
(c) Variation of the frequency for the eigenvalues involved in SSR with APC plus PMS.
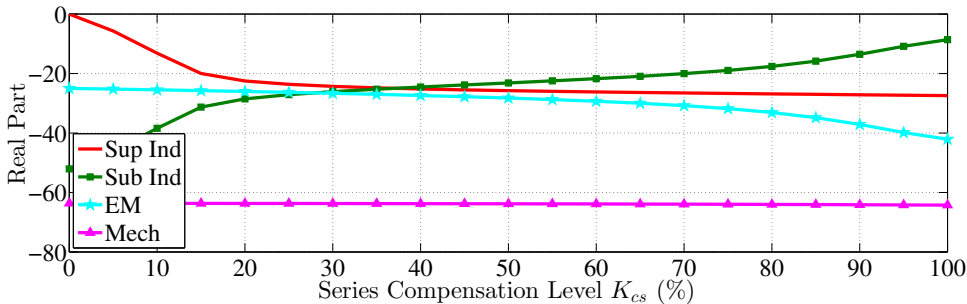
(d) Variation of the real part for the eigenvalues involved in SSR with APC plus PMS.

Figure 5.7: Dynamic evolution of the real part and frequency of the main eigenvalues with respect to the percentage of series compensation, only with PMS and APC plus PMS.
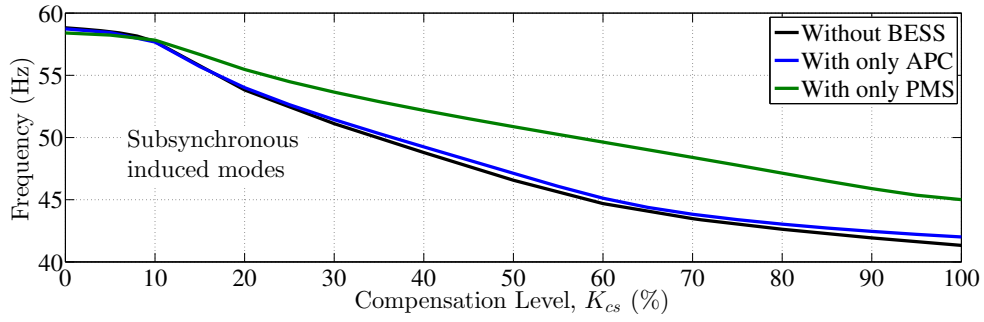
(a) Variation of the frequency for subsynchronous induced mode.
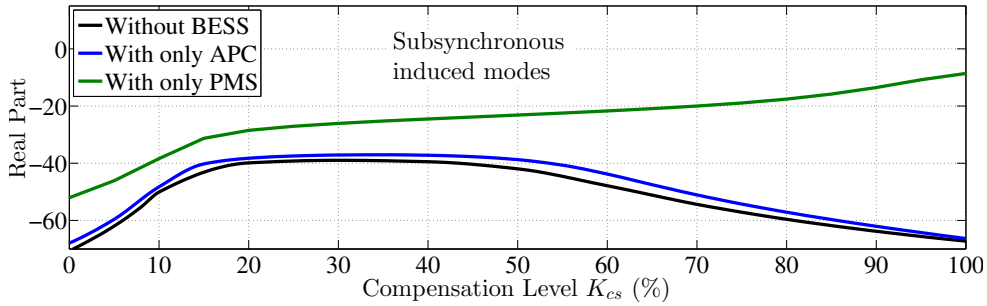
(b) Variation of the real part for the subsynchronous induced mode.
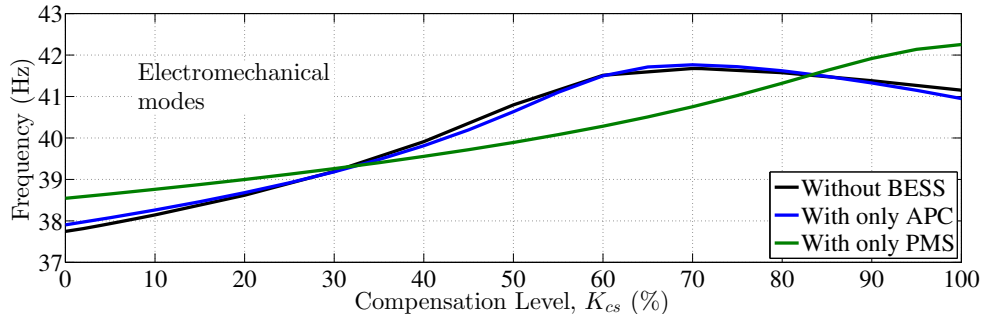
(c) Variation of the frequency for the electromechanical mode.
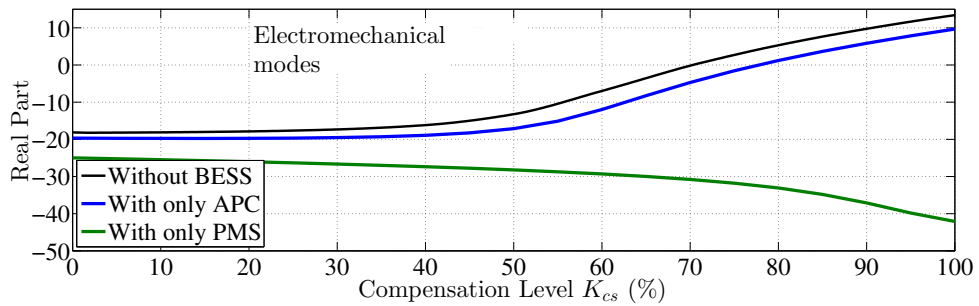
(d) Variation of the real part for the electromechanical mode.

Figure 5.8: Dynamic evolution of the real part and frequency of the subsynchronous induced and electromechanical modes. The case without the BESS, with only APC, and with only PMS.

Conclusions

An integral study of the DFIG-based wind farm in the presence of an SSR condition was presented in this Thesis. The results show the process of how the phenomenon of SSR is generated under a transient in a series-compensated transmission line. Besides, it shows how the back-to-back converter intervenes and can be part of the solution or part of the problem. Moreover, the integration of a BESS as a solution to improve the stability and power control of the WECS was investigated. According to the topics discussed in Thesis, the most remarkable results are described in the following paragraphs.

In reviewing the state of the art, a lack of a complete methodology of how can be tuned the back-to-back converter controllers for a DFIG-based wind farm was found. In this context, a study of the GSCC and RSCC was developed, the challenges associated with this topology involve the mathematical development of the transfer function of the state variables to control. Basically, the RSCC involves mechanical state variables of the induction machine to be controller, besides that, the dynamic model of the induction machine is quite complex due to the decoupling of the stator and rotor state variables is not an easy task. Based on all of the above, a complete methodology for tuning the controllers of the DFIG-based back-to-back converter was presented. The proposed methodology includes a tuning process that does not require a transfer function for the outer loop. A plant for the voltage control of the induction machine stator terminals was proposed. In general, five approaches were applied to tuning the DFIG-based back-to-back converter controllers. As a result, the proposed methodology improves the system stability under resonance conditions.

On the other hand, modal impedance and small-signal-stability analysis were applied to generate a methodological procedure that identifies the modes involved in SSR, moreover, the origin that produces SSR was determined. Based on modal impedance and small-signal-stability analysis the system that is prone to SSR can be characterized to implement a target solution. It was demonstrated that modal impedance can discriminate the sources of resonance, in this case, the capacitor which produces it. There are three phenomena that produce SSR (IGE, TI, and TA); as a result, the phenomenon of TA was identified as the cause that originates SSR. In this context, a target solution can be implemented to

91

mitigate the SSR issues.

In this Thesis, the BESS integration as a tool to solve the problems related to SSR was investigated. Two schemes were applied in the controller for the BESS, the first one includes a well-reported scheme for active power control, the second scheme is proposed as a solution to mitigate the specific phenomenon of torque amplification. The results shown in this research are three, 1) the active power control can improve the stability of the system, in this case, by modifying the electromechanical mode, 2) the proposed control scheme for the BESS can compensate the components of current that are induced into the induction generator, the stability of the system is improved by modifying of the subsynchronous induced mode, and 3) the two schemes that improve the system under SSR condition can operate at the same time or individually in the BESS control without any trouble or disadvantage.

As it was demonstrated, the advantages of the BESS are outstanding due to its capacity of storage energy and release when it is necessary. These attributes make the BESS the FACT with the major capacity to solve issues. The major challenge that was found in this Thesis about the BESS integration is to propose and apply a specific scheme in the control block targeted for a specific phenomenon. It was demonstrated that power management can improve the stability of the DFIG-based system due to a small disturbance, it can be called a general solution. The target of the proposed mitigation scheme is to isolate the series compensated transmission line of the induction machine avoiding the interaction of the subcomponent of current (produced by a small disturbance in the transmission line side) with the induction machine.

Future Work

According to the state of the art, the future of the BESS is promising, besides its application to solve a set of problems related to power generation and transmission is quite relevant for the worldwide interest.

In the area of subsynchronous oscillation, the BESS has shown an excellent performance to solve those issues. The IGE or TI could also be the origin of SSR, then new schemes to protect the system must be developed.

There is still uncertainty on the benefits of the use of modal impedance compared to other techniques such as impedance modeling or Nyquist plot. In this context, a comparative study highlighting the benefits or drawbacks of each method applied to WECS prone to SSR is required.

Nowadays, the interaction of several generation sources of electricity has become a reality. The schemes of a generation that involve the interconnection of WECS, photovoltaic, the called "green hydrogen" must be studied to avoid future problems for bulk transmission of electricity.

The energy transition is also a reality and this is reaching each country. In the per-

spective of the author, the electricity demand will be increased due to the massive use of electric vehicles. Next to the commitment to mitigate climate change green energy must provide a stable background to avoid the use of fossil fuel-based energy. In this context, the study of BESS and the schemes for bulk transmission of energy will increase covering a great interest of the scientific community; the solution will be focused on schemes based on wind-to-hydrogen to produce fuel, and wind-to-batteries schemes to transmit energy through series-compensated overhead transmission lines or HVDC. In such scenarios, the subsynchronous oscillations will be prone to appear.

Bibliography

[1] A. E. Leon and J. A. Solsona, "Sub-synchronous interaction damping control for dfig wind turbines," *IEEE Transactions on Power Systems*, vol. 30, no. 1, pp. 419–428, 2015.

[2] GWEC, "Wind report, global wind energy council of 2020," March 2021.

[3] SENER, "Prospectivas de energía renovables 2018-2032," March 2019.

[4] B. Agrawal and R. Farmer, "Use of frequency scanning techniques for subsynchronous resonance analysis," *IEEE Transactions on Power Apparatus and Systems*, vol. PAS-98, no. 2, pp. 341–349, 1979.

[5] "Proposed terms and definitions for subsynchronous oscillations," *IEEE Transactions on Power Apparatus and Systems*, vol. PAS-99, no. 2, pp. 506–511, 1980.

[6] "Terms, definitions and symbols for subsynchronous oscillations," *IEEE Transactions on Power Apparatus and Systems*, vol. PAS-104, no. 6, pp. 1326–1334, 1985.

[7] L. C. Gross, "Sub-synchronous grid conditions: New event, new problem, and new solutions," *in Proc. Western Protective Relay Conf.*, pp. 1–19, 2010.

[8] ABB, "Series compensation: boosting transmission capacity," 2021.

[9] N. G. Hingorani and L. Gyugyi, *Understanding FACTS: Concepts and Technology of Flexible AC Transmission Systems*, pp. 425–429. 2000.

[10] J. W. Butler and C. Concordia, "Analysis of series capacitor application problems," *Transactions of the American Institute of Electrical Engineers*, vol. 56, no. 8, pp. 975–988, 1937.

[11] "Reader's guide to subsynchronous resonance," *IEEE Transactions on Power Systems*, vol. 7, no. 1, pp. 150–157, 1992.

[12] F. Yan, X. Wang, Y. Xu, and C. Chen, "Dynamic equivalence of torsional interaction in multi-identical-machine power system," *Electric Power Components and Systems*, 207.

[13] L. A. Kilgore, L. C. Elliott, and E. R. Taylor, "The prediction and control of self-excited oscillations due to series capacitors in power systems," *IEEE Transactions on Power Apparatus and Systems*, vol. PAS-90, no. 3, pp. 1305–1311, 1971.

[14] J. W. Ballance and S. Goldberg, "Subsynchronous resonance in series compensated transmission lines," *IEEE Transactions on Power Apparatus and Systems*, vol. PAS-92, no. 5, pp. 1649–1658, 1973.

[15] R. Tweedie and H. W. Abrams, "Electrical features of the 1590 mw coal-slurry-supplied mohave generating station," *IEEE Transactions on Power Apparatus and Systems*, vol. PAS-90, no. 2, pp. 725–735, 1971.

[16] N. G. Hingorani and L. Gyugyi, *Static Series Compensators: GCSC, TSSC, TCSC and SSSC*, pp. 209–265. 2000.

[17] Xiangning Xiao, Benfeng Gao, Chengyong Zhao, and Xu Kun, "A novel ssr-damping scheme based on imbalance operation of sssc," in *2010 International Conference on Power System Technology*, pp. 1–5, 2010.

[18] F. D. de Jesus, E. H. Watanabe, L. F. W. de Souza, and J. E. R. Alves, "Ssr and power oscillation damping using gate-controlled series capacitors (gcsc)," *IEEE Transactions on Power Delivery*, vol. 22, no. 3, pp. 1806–1812, 2007.

[19] K. M. Alawasa, Y. A. I. Mohamed, and W. Xu, "New approach to damp subsynchronous resonance by reshaping the output impedance of voltage-sourced converters," in *2013 IEEE Power Energy Society General Meeting*, pp. 1–5, 2013.

[20] K. M. Alawasa, Y. A. I. Mohamed, and W. Xu, "Active mitigation of subsynchronous interactions between pwm voltage-source converters and power networks," *IEEE Transactions on Power Electronics*, vol. 29, no. 1, pp. 121–134, 2014.

[21] X. Zheng and Z. Xu, "A combined control scheme to mitigate ssr for steady state and transient state of power systems," in *2010 International Conference on Power System Technology*, pp. 1–6, 2010.

[22] N. Rostamkolai, R. J. Piwko, E. V. Larsen, D. A. Fisher, M. A. Mobarak, and A. E. Poitras, "Subsynchronous interactions with static var compensators-concepts and practical implications," *IEEE Transactions on Power Systems*, vol. 5, no. 4, pp. 1324–1332, 1990.

[23] M. Bahrman, E. V. Larsen, R. J. Piwko, and H. S. Patel, "Experience with hvdc - turbine-generator torsional interaction at square butte," *IEEE Transactions on Power Apparatus and Systems*, vol. PAS-99, no. 3, pp. 966–975, 1980.

[24] V. Virulkar and G. Gotmare, "Sub-synchronous resonance in series compensated wind farm: A review," *Renewable and Sustainable Energy Reviews*, vol. 55, pp. 1010 – 1029, 2016.

[25] C. T. Wu, K. J. Peterson, R. J. Piwko, M. D. Kankam, and D. H. Baker, "The inter-mountain power project commissioning-subsynchronous torsional interaction tests," *IEEE Transactions on Power Delivery*, vol. 3, no. 4, pp. 2030–2036, 1988.

[26] N. A. E. R. Corporation, "Lesson learned. sub-synchronous interaction between series-compensated transmission lines and generation," *Technical Report*, pp. 1–3, 2011.

[27] Z. Miao, "Impedance-model-based ssr analysis for type 3 wind generator and series-compensated network," *IEEE Transactions on Energy Conversion*, vol. 27, no. 4, pp. 984–991, 2012.

[28] A. T. Memorandum, "Technical memorandum comments on ercot nprr562 other informational terms," *Comments on ERCOT NPRR562*, pp. 1–3, 2013.

[29] G. D. Irwin, A. K. Jindal, and A. L. Isaacs, "Sub-synchronous control interactions between type 3 wind turbines and series compensated ac transmission systems," in *2011 IEEE Power and Energy Society General Meeting*, pp. 1–6, 2011.

[30] T. Ackermann and L. Soder, *Wind Power in Power Systems*. 10 2005.

[31] V. Yaramasu, B. Wu, P. C. Sen, S. Kouro, and M. Narimani, "High-power wind energy conversion systems: State-of-the-art and emerging technologies," *Proceedings of the IEEE*, vol. 103, no. 5, pp. 740–788, 2015.

[32] F. Blaabjerg and K. Ma, "Wind energy systems," *Proceedings of the IEEE*, vol. 105, no. 11, pp. 2116–2131, 2017.

[33] GWEC, "Wind report, global wind energy council of 2019," March 2020.

[34] M. Liserre, R. Cárdenas, M. Molinas, and J. Rodriguez, "Overview of multi-mw wind turbines and wind parks," *IEEE Transactions on Industrial Electronics*, vol. 58, no. 4, pp. 1081–1095, 2011.

[35] S. Bhowmik, R. Spee, and J. H. R. Enslin, "Performance optimization for doubly fed wind power generation systems," *IEEE Transactions on Industry Applications*, vol. 35, no. 4, pp. 949–958, 1999.

[36] R. Datta and V. T. Ranganathan, "A method of tracking the peak power points for a variable speed wind energy conversion system," *IEEE Transactions on Energy Conversion*, vol. 18, no. 1, pp. 163–168, 2003.

[37] P. Pourbeik, R. J. Koessler, D. L. Dickmander, and W. Wong, "Integration of large wind farms into utility grids (part 2 - performance issues)," in *2003 IEEE Power Engineering Society General Meeting (IEEE Cat. No.03CH37491)*, vol. 3, pp. 1520–1525 Vol. 3, 2003.

[38] H. A. Mohammadpour, "Analysis of sub-synchronous resonance in doubly-fed induction generator-based wind farms interfaced with gate – controlled series capacitor," *IET Generation, Transmission and Distribution*, vol. 8, pp. 1998–2011(13), December 2014.

[39] H. A. Mohammadpour and E. Santi, "Sub-synchronous resonance analysis in dfig-based wind farms: Definitions and problem identification — part i," in *2014 IEEE Energy Conversion Congress and Exposition (ECCE)*, pp. 812–819, 2014.

[40] I. B. M. Matsuo, F. Salehi, L. Zhao, Y. Zhou, and W. Lee, "Optimized frequency scanning of nonlinear devices applied to subsynchronous resonance screening," *IEEE Transactions on Industry Applications*, vol. 56, no. 3, pp. 2281–2291, 2020.

[41] Z. Miao, "Impedance-model-based ssr analysis for type 3 wind generator and series-compensated network," *IEEE Transactions on Energy Conversion*, vol. 27, no. 4, pp. 984–991, 2012.

[42] K. Sun, W. Yao, J. Fang, X. Ai, J. Wen, and S. Cheng, "Impedance modeling and stability analysis of grid-connected dfig-based wind farm with a vsc-hvdc," *IEEE Journal of Emerging and Selected Topics in Power Electronics*, vol. 8, no. 2, pp. 1375–1390, 2020.

[43] M. Amin and M. Molinas, "Impedance based stability analysis of vsc-based hvdc system," in *2015 IEEE Eindhoven PowerTech*, pp. 1–6, 2015.

[44] H. Liu and J. Sun, "Impedance-based stability analysis of vsc-based hvdc systems," in *2013 IEEE 14th Workshop on Control and Modeling for Power Electronics (COMPEL)*, pp. 1–8, 2013.

[45] M. Amin and M. Molinas, "Understanding the origin of oscillatory phenomena observed between wind farms and hvdc systems," *IEEE Journal of Emerging and Selected Topics in Power Electronics*, vol. 5, no. 1, pp. 378–392, 2017.

[46] M. Amin, M. Molinas, J. Lyu, and X. Cai, "Impact of power flow direction on the stability of vsc-hvdc seen from the impedance nyquist plot," *IEEE Transactions on Power Electronics*, vol. 32, no. 10, pp. 8204–8217, 2017.

[47] M. Amin and M. Molinas, "A gray-box method for stability and controller parameter estimation in hvdc-connected wind farms based on nonparametric impedance," *IEEE Transactions on Industrial Electronics*, vol. 66, no. 3, pp. 1872–1882, 2019.

[48] H. A. Mohammadpour, S. M. H. Mirhoseini, and A. Shoulaie, "Comparative study of proportional and ts fuzzy controlled gcsc for ssr mitigation," in *2009 International Conference on Power Engineering, Energy and Electrical Drives*, pp. 564–569, 2009.

[49] "First benchmark model for computer simulation of subsynchronous resonance," *IEEE Transactions on Power Apparatus and Systems*, vol. 96, no. 5, pp. 1565–1572, 1977.

[50] A. Singh and A. K. Bohre, "Market analysis in a restructured power system with tcsc by lmp calculation," in *2020 International Conference on Computational Intelligence for Smart Power System and Sustainable Energy (CISPSSE)*, pp. 1–7, 2020.

[51] H. A. Mohammadpour and E. Santi, "Sub-synchronous resonance analysis in dfig-based wind farms: Mitigation methods — tcsc, gcsc, and dfig controllers — part ii," in *2014 IEEE Energy Conversion Congress and Exposition (ECCE)*, pp. 1550–1557, 2014.

[52] H. A. Mohammadpour, M. M. Islam, E. Santi, and Y. Shin, "Ssr damping in fixed-speed wind farms using series facts controllers," *IEEE Transactions on Power Delivery*, vol. 31, no. 1, pp. 76–86, 2016.

[53] Y. C. Choo, A. P. Agalgaonkar, K. M. Muttaqi, S. Perera, and M. Negnevitsky, "Sub-synchronous torsional interaction behaviour of wind turbine-generator unit connected to an hvdc system," in *IECON 2010 - 36th Annual Conference on IEEE Industrial Electronics Society*, pp. 996–1002, 2010.

[54] W. Qu and J. Jiang, "Ssti and its mitigation in wind farms connected with an hvdc line," *Procedia Computer Science*, vol. 111, pp. 399–405, 2017. The 8th International Conference on Advances in Information Technology.

[55] S. Velpula, R. Thirumalaivasan, and M. Janaki, "Stability analysis on torsional interactions of turbine-generator connected with dfig-wecs using admittance model," *IEEE Transactions on Power Systems*, vol. 35, no. 6, pp. 4745–4755, 2020.

[56] W. Ren and E. Larsen, "A refined frequency scan approach to sub-synchronous control interaction (ssci) study of wind farms," *IEEE Transactions on Power Systems*, vol. 31, no. 5, pp. 3904–3912, 2016.

[57] P. Li, J. Wang, L. Xiong, M. Ma, Z. Wang, and S. Huang, "Mitigating subsynchronous control interaction using fractional sliding mode control of wind farm," *Journal of the Franklin Institute*, vol. 357, no. 14, pp. 9523–9542, 2020.

[58] P. Li, J. Wang, L. Xiong, S. Huang, Z. Wang, and M. Ma, "Ssci mitigation of grid-connected dfig wind turbines with fractional-order sliding mode controller," *Wind Energy*, vol. 23, no. 7, pp. 1564–1577, 2020.

[59] A. Chen, D. Xie, D. Zhang, C. Gu, and K. Wang, "Pi parameter tuning of converters for sub-synchronous interactions existing in grid-connected dfig wind turbines," *IEEE Transactions on Power Electronics*, vol. 34, no. 7, pp. 6345–6355, 2019.

[60] R. Moreno-Sánchez, C. A. Núñez-Gutiérrez, N. Visairo-Cruz, J. Hernández-Ramírez, and J. Segundo-Ramírez, "Understanding the origin of ssr in series-compensated dfig-based wind farms: Analysis techniques and tuning," *IEEE Access*, vol. 9, pp. 117660–117672, 2021.

[61] P. M. Anderson and A. Bose, "Stability simulation of wind turbine systems," *IEEE Transactions on Power Apparatus and Systems*, vol. PAS-102, no. 12, pp. 3791–3795, 1983.

[62] L. Yang, Z. Xu, J. Østergaard, Z. Y. Dong, K. P. Wong, and X. Ma, "Oscillatory stability and eigenvalue sensitivity analysis of a dfig wind turbine system," *IEEE Transactions on Energy Conversion*, vol. 26, no. 1, pp. 328–339, 2011.

[63] *Analysis of Electric Machinery and Drive Systems*. John Wiley & Sons, Ltd, 2013.

[64] A. Nabavi-Niaki and M. R. Iravani, "Steady-state and dynamic models of unified power flow controller (upfc) for power system studies," *IEEE Transactions on Power Systems*, vol. 11, no. 4, pp. 1937–1943, 1996.

[65] P. kUNDUR. New York: McGraw-Hill, 1994.

[66] R. Pena, J. C. Clare, and G. M. Asher, "Doubly fed induction generator using back-to-back pwm converters and its application to variable-speed wind-energy generation," *in IEE Proceedings - Electric Power Applications*, vol. vol. 143, no. no. 3, pp. pp. 231–241, May 1996.

[67] G.-C. Hsieh and J. Hung, "Phase-locked loop techniques. a survey," *IEEE Transactions on Industrial Electronics*, vol. 43, no. 6, pp. 609–615, 1996.

[68] M. A. Casacca and Z. M. Salameh, "Determination of lead-acid battery capacity via mathematical modeling techniques," *IEEE Transactions on Energy Conversion*, vol. 7, no. 3, pp. 442–446, 1992.

[69] Z. M. Salameh, M. A. Casacca, and W. A. Lynch, "A mathematical model for lead-acid batteries," *IEEE Transactions on Energy Conversion*, vol. 7, no. 1, pp. 93–98, 1992.

[70] J. Appelbaum and R. Weiss, "An electrical model of the lead-acid battery," in *INT-ELEC '82 - International Telecommunications Energy Conference*, pp. 304–307, 1982.

[71] M. T. Lawder, B. Suthar, P. W. C. Northrop, S. De, C. M. Hoff, O. Leitermann, M. L. Crow, S. Santhanagopalan, and V. R. Subramanian, "Battery energy storage system (bess) and battery management system (bms) for grid-scale applications," *Proceedings of the IEEE*, vol. 102, no. 6, pp. 1014–1030, 2014.

[72] C. L. C. Lu and C. Wu, "Dynamic modelling of battery energy storage system and application to power system stability," *in IEE Proceedings - Generation, Transmission and Distribution*, vol. Vol. 142, no. no. 4, pp. pp. 429–435, July 1995.

[73] A. Oudalov, D. Chartouni, and C. Ohler, "Optimizing a battery energy storage system for primary frequency control," *IEEE Transactions on Power Systems*, vol. 22, no. 3, pp. 1259–1266, 2007.

[74] P. Mercier, R. Cherkaoui, and A. Oudalov, "Optimizing a battery energy storage system for frequency control application in an isolated power system," *IEEE Transactions on Power Systems*, vol. 24, no. 3, pp. 1469–1477, 2009.

[75] S. Teleke, M. E. Baran, S. Bhattacharya, and A. Q. Huang, "Rule-based control of battery energy storage for dispatching intermittent renewable sources," *IEEE Transactions on Sustainable Energy*, vol. 1, no. 3, pp. 117–124, 2010.

[76] J. Zeng, B. Zhang, C. Mao, and Y. Wang, "Use of battery energy storage system to improve the power quality and stability of wind farms," in *2006 International Conference on Power System Technology*, pp. 1–6, 2006.

[77] Z. Yang, C. Shen, L. Zhang, M. L. Crow, and S. Atcitty, "Integration of a statcom and battery energy storage," *IEEE Transactions on Power Systems*, vol. 16, no. 2, pp. 254–260, 2001.

[78] S. K. Tiwari, B. Singh, and P. K. Goel, "Control of wind–diesel hybrid system with bess for optimal operation," *IEEE Transactions on Industry Applications*, vol. 55, no. 2, pp. 1863–1872, 2019.

[79] M. S. J. A. U. T. M. Bajracharya, Chandra; Molinas, "Understanding of tuning techniques of converter controllers for vsc-hvdc," Proceedings of the Nordic Workshop on Power and Industrial Electronics (NORPIE/2008), p. 8, Helsinki University of Technology; Teknillinen korkeakoulu, 2008.

[80] O. Aydin, A. Akdag, P. Stefanutti, and N. Hugo, "Optimum controller design for a multilevel ac-dc converter system," in *Twentieth Annual IEEE Applied Power Electronics Conference and Exposition, 2005. APEC 2005.*, vol. 3, pp. 1660–1666 Vol. 3, 2005.

[81] A. Yazdani and R. Iravani, *Control of Half-Bridge Converter*, pp. 48–68. 2010.

[82] J. G. Ziegler and N. B. Nichols, "Optimum Settings for Automatic Controllers," *Trans. ASME*, pp. 759–768, 06 1942.

[83] K. Åström and T. Hägglund, "Revisiting the ziegler–nichols step response method for pid control," *Journal of Process Control*, vol. 14, no. 6, pp. 635 – 650, 2004.

[84] N. W. Miller, W. W. Price, and J. J. Sanchez-Gasca, "Dynamic modeling of ge 1.5 and 3.6 wind turbine-generators," 2003.

[85] R. Gagnon, M. Fecteau, P. Prud'Homme, E. Lemieux, G. Turmel, D. Pare, and F. Duong, "Hydro-québec strategy to evaluate electrical transients following wind power plant integration in the gaspésie transmission system," *IEEE Transactions on Sustainable Energy*, vol. 3, no. 4, pp. 880–889, 2012.

[86] R. G. et al., "Large-scale real-time simulation of wind power plants into hydro-québec power system," *in Proc. 9th Int. Workshop Largescale Integr. Wind Power Syst. well Transmiss. Netw. Offshore Wind Plants, Quebec City, QC, Canada*, Oct. 2010.

[87] Wilsun Xu, Zhenyu Huang, Yu Cui, and Haizhen Wang, "Harmonic resonance mode analysis," *IEEE Transactions on Power Delivery*, vol. 20, no. 2, pp. 1182–1190, 2005.

[88] I. J. Perez-arriaga, G. C. Verghese, and F. C. Schweppe, "Selective modal analysis with applications to electric power systems, part i: Heuristic introduction," *IEEE Transactions on Power Apparatus and Systems*, vol. PAS-101, no. 9, pp. 3117–3125, 1982.

[89] A. Petersson, T. Thiringer, L. Harnefors, and T. Petru, "Modeling and experimental verification of grid interaction of a dfig wind turbine," *IEEE Transactions on Energy Conversion*, vol. 20, no. 4, pp. 878–886, 2005.

[90] R. D. Kelly, "Electronic circuit analysis and design by driving-point impedance techniques," *IEEE Transactions on Education*, vol. 13, no. 3, pp. 154–167, 1970.

[91] R. Wang, Q. Sun, D. Ma, and Z. Liu, "The small-signal stability analysis of the droop-controlled converter in electromagnetic timescale," *IEEE Transactions on Sustainable Energy*, vol. 10, no. 3, pp. 1459–1469, 2019.

[92] J. M. M. A. E. Leon and J. A. Solsona, "Subsynchronous resonance mitigation using variable-speed wind energy conversion systems,," *in IET Generation, Transmission & Distribution*, vol. vol. 7, no. no. 5, pp. pp. 511–525, May 2013.

[93] E. Reihani and R. Ghorbani, "Load commitment of distribution grid with high penetration of photovoltaics (pv) using hybrid series-parallel prediction algorithm and storage," *Electric Power Systems Research*, vol. 131, pp. 224–230, 2016.

[94] R. G. Farmer, "Second benchmark model for computer simulation of subsynchronous resonance ieee subsynchronous resonance working group of the dynamic system performance subcommittee power system engineering committee," *IEEE Power Engineering Review*, vol. PER-5, no. 5, pp. 34–34, 1985.

[95] S. Muyeen, R. Takahashi, T. Murata, J. Tamura, and M. H. Ali, "Application of statcom/bess for wind power smoothening and hydrogen generation," *Electric Power Systems Research*, vol. 79, no. 2, pp. 365–373, 2009.

[96] O. B. Adewuyi, R. Shigenobu, K. Ooya, T. Senjyu, and A. M. Howlader, "Static voltage stability improvement with battery energy storage considering optimal control of active and reactive power injection," *Electric Power Systems Research*, vol. 172, pp. 303–312, 2019.

[97] L. X. W. Guo and S. Dai, "Fault current limiter-battery energy storage system for the doubly-fed induction generator: analysis and experimental verification," *in IET Generation, Transmission & Distribution*, vol. vol. 10, no. no. 3, pp. pp. 653–660, Feb. 2016.

[98] L. Fan, R. Kavasseri, Z. L. Miao, and C. Zhu, "Modeling of dfig-based wind farms for ssr analysis," *IEEE Transactions on Power Delivery*, vol. 25, no. 4, pp. 2073–2082, 2010.

Appendix A

Parameters and Nomenclature

Table A.1: Gains used in the BESS.

Gains	Literature	Calculated	Gains
K_{Pp}	0.1595	K_{Ip}	1/0.25
K_{Pidb}	3	K_{Iidb}	80
K_{Pq}	0.1595	K_{Ipq}	1/0.25
K_{Piqb}	3	K_{Iiqb}	80

Table A.2: WECS parameters.

Symbol	Description	Value
S_B	Single machine	1.667 MVA
V_B	Stator voltage (L-L rms)	575 V
f_o	Nominal frequency	60 Hz
ω_b	Base frequency	$2\pi f_o$
ω_{mb}	Base mechanical frequency	125.66 r/s
ω_r	Mechanical rotor speed	1.02
U_{dc}	DC-link voltage	1.15 kV
C_{dc}	DC-link capacitance	10 mF
f_{sw}	Commutation frequency	4980 Hz
R_{wt}	Turbine radius	37.5 m
C_p	Power coefficient	from [?]
V_w	Wind speed	13 m/s
β	Pitch angle	3.072°
N_{tg}	Gearbox ratio	1
P_{pp}	Pole-pair number	3
f_r	Rotor electrical frequency	1.02
H_{wt}	Turbine inertia constant	4.32 s
H_g	Generator inertia constant	0.685 s
K_{tg}	Shaft stiffness	1.11
D_{tg}	Shaft mutual damping	1.5
L_{ls}	Stator leakage inductance	0.018
L_{lr}	Rotor leakage inductance	0.016
L_m	Mutual inductance	2.9
R_s	Stator resistance	0.023
R_r	Rotor resistance	0.016
F	Generator mechanical damping	0.01
r_{sw}	VSC switch on-state resistance	0.001 Ω
R_T	Transformer equivalent resistance	0.001
L_T	Transformer equivalent inductance	0.005/3
R_{L1}	Transmission line equivalent resistance	0.02573
L_{L1}	Transmission line equivalent inductance	0.01972
R_{L2}	Transmission line equivalent resistance	0.001
L_{L2}	Transmission line equivalent inductance	0.006
L_g	GSC inductance	0.3
R_g	GSC resistance	0.003

Except where indicated, parameters are in *per unit* system.

Mathematical Explanations

The aim of this appendix is for the demonstration of some mathematical developments.

B.1 PWM Time Delay Approximation

The time delay model is required to model physical processes, it is described mathematically as:

$$G_{td} = e^{-\tau_{td}s} \tag{Beq.1}$$

This model is very common, nevertheless, there are some major consequences as: complicates the analysis and design of feedback systems, it makes satisfactory control more difficult to achieve, reduces the stability of a system, and it limits the achievable response time of the system. In consequence, there are some approximations that can be used. One can be obtained graphically and the second is based on Taylor series expansion. The following approximation can be used as long as, the time delay being sufficiently small compared to rate of change of the controlled signal. If the input signal were with a constant slope the approximation would be perfect for any value of τ_{td}. When the input signal varies rapidly, a small value of τ_{td} will give a good approximation. The approximations are explained below.

- The Padé approximation provides a family of approximations of increasing accuracy and complexity:

$$e^{\tau_{td}s} = \frac{e^{-\tau_{td}s/2}}{e^{\tau_{td}s/2}} \approx \frac{1 - \tau_{td}s/2 + \tau_{td}^2 s^2/4 - \tau_{td}^3 s^3/12 + ... + \frac{(-\tau_{td}s/2)^k}{k!}}{1 + \tau_{td}s/2 + \tau_{td}^2 s^2/4 + \tau_{td}^3 s^3/12 + ... + \frac{(\tau_{td}s/2)^k}{k!}} \tag{Beq.2}$$

- In some cases a very simple approximation given by a first-order lag can be used:

$$e^{\tau_{td}s} \approx \frac{1}{\tau_{td}s + 1} \tag{Beq.3}$$

- Another approximation can be:

$$e^{\tau_{td}s} = \frac{e^{-\tau_{td}s/2}}{e^{\tau_{td}s/2}} \approx \frac{\left(1 - \frac{\tau_{td}s}{2k}\right)^k}{\left(1 + \frac{\tau_{td}s}{2k}\right)^k} \tag{Beq.4}$$

B.2 Inner Current Controller Transfer Function Simplification

The simplification idea is based on the reduction of a second-order model into a first-order model. This simplification can be achieved through a signal-prove input, as a unit step. This input must provide a equal output for both systems.

The closed-loop second order transfer function from Equation (3.6) is rewritten as follows:

$$G_{so} = \frac{1}{2T_a^2 s^2 + 2T_a s + 1} \tag{Beq.5}$$

The proposed reduction is selected such that, the zero-pole reduction being achieve by the cancellation of the zero of the controller with the pole of the proposed simplification of the first-order transfer function. In this sense, the proposed model is:

$$G_{fo} = \frac{1}{T_{eq}s + 1} \tag{Beq.6}$$

The error of (Beq.5) and (Beq.6) are evaluated under a unit-step input. Then, the equivalent time constant T_{eq} is equating to the error of the two transfer functions.

The respective error functions respect a step-unit function ($U(s) = \frac{1}{s}$) as input are:

$$Err_1(s) = \frac{1}{s} - \frac{1}{s}\frac{1}{2T_a^2 s^2 + 2T_a s + 1} = \frac{2T_a^2 s + 2T_a}{2T_a^2 s^2 + 2T_a s + 1} \tag{Beq.7}$$

$$Err_2(s) = \frac{1}{s} - \frac{1}{s}\frac{1}{T_{eq}s + 1} = \frac{T_{eq}}{T_{eq}s + 1} \tag{Beq.8}$$

Now, the integral in the time domain of the two transfer functions to be equal is:

$$\int_0^\infty Err_1(t)dt = \int_0^\infty Err_2(t)dt \tag{Beq.9}$$

Using the definition of Laplace transform, it is possible to establish the next equality for (Beq.7) and extrapolate to (Beq.8).

$$\mathcal{L}[Err_1(t)] = Err_1(s) = \int_0^\infty e^{-st} Err_1(t)dt \qquad \text{(Beq.10)}$$

Taking the condition $s \to 0$, the above equation becomes:

$$\lim_{s \to 0} Err_1(s) = \int_0^\infty Err_1(t)dt \qquad \text{(Beq.11)}$$

Hence, the equality in (Beq.9) can be substituted by:

$$\lim_{s \to 0} Err_1(s) = \lim_{s \to 0} Err_2(s) \qquad \text{(Beq.12)}$$

Then, the error of the two functions are:

$$\lim_{s \to 0} \frac{2T_a^2 s + 2T_a}{2T_a^2 s^2 + 2T_a s + 1} = \lim_{s \to 0} \frac{T_{eq}}{T_{eq}s + 1} \qquad \text{(Beq.13)}$$

Finally, the value for T_{eq} to fulfill the requirements is:

$$T_{eq} = 2T_a. \qquad \text{(Beq.14)}$$

B.3 Outer Controller Tuning Criterion

Equation (3.13) with the constants K and T_c can be rewritten as:

$$G_{udc,OL}(s) = K_{Pudc} \left(\frac{T_{Iudc}s + 1}{T_{Iudc}s} \right) \left(\frac{K}{T_{eq}s + 1} \right) \left(\frac{1}{T_c s} \right) \qquad \text{(Beq.15)}$$

The terms of above transfer function is rearranged and the frequency terms is change with $s \to j\omega$ we have:

$$G_{udc,OL}(j\omega) = \left(\frac{K_{Pudc}K}{T_c T_{Iudc}(j\omega)^2} \right) \left(\frac{T_{Iudc}(j\omega) + 1}{T_{eq}(j\omega) + 1} \right) \qquad \text{(Beq.16)}$$

The Nyquist criteria of stability are:

$$|G_{udc,OL}(j\omega)| = 1 \tag{Beq.17}$$

and

$$\angle G_{udc,OL}(j\omega) = -180° + \Phi_M \tag{Beq.18}$$

where Φ_M is the phase margin. Then, from the angle condition from the open loop of the outer controller is:

$$\angle G_{udc,OL}(j\omega) = -180° + \tan^{-1}(\omega T_{Iudc}) - \tan^{-1}(\omega T_{eq}) = 180° + \varphi \tag{Beq.19}$$

The angle φ is positive for all the values of ω. Differentiation of this angle with respect to ω can give the maximum value of phase margin. The value of T_{Iudc} should be designed to be small, specially when φ approaches Φ_M, otherwise the response to the disturbance becomes slow. In this sense, the maximization condition $\frac{d\varphi}{d\omega} = 0$, the angle is maximum when $\omega_d = \frac{1}{\sqrt{T_{Iudc}T_{eq}}}$. Hence the phase margin is:

$$\Phi_M = \tan^{-1}\sqrt{\frac{T_{Iudc}}{T_{eq}}} - \tan\sqrt{\frac{T_{eq}}{T_{Iudc}}} \tag{Beq.20}$$

This condition gives the tuning criterion for the time constant of the controller as:

$$T_{Iudc} = T_{eq}\left(\frac{1 + \sin\Phi_M}{1 - \sin\Phi_M}\right) \tag{Beq.21}$$

The resulting open loop frequency characteristic will have a maximum phase of Φ_M at the crossover frequency of ω_d, symmetric about $\frac{1}{T_{Iudc}}$ and $\frac{1}{T_{eq}}$. Then by the symmetric property, we can also write:

$$T_{Iudc} = a^2 T_{eq} \tag{Beq.22}$$

where a is a symmetrical distance between $1/T_{Iudc}$ to ω_d, and $1/T_{eq}$ to ω_d. Now, from the magnitude condition, the tuning for the gain of controllers can be found as follows:

$$|G_{udc,OL}(j\omega)| = \frac{K_{Pudc}K}{\omega_d^2 T_{Iudc}T_c}\sqrt{\frac{(\omega_d T_{Iudc})^2 + 1}{(\omega_d T_{eq})^2 + 1}} = 1 \tag{Beq.23}$$

Then, the proportional gain is obtained as follows:

$$K_{Pudc} = \frac{T_c}{K\sqrt{T_{Iudc}T_{eq}}}. \tag{Beq.24}$$

Appendix C

Simulation Software and System Integration

The simulation software used in this Thesis are PSCAD and MatLab. PSCAD is used mainly to validate the models described above and the integrated system, as well. The dynamic simulations depicted in this Thesis are computed by the ordinary differential equation solver. In this sense, this section is devoted to describe the process of simulation with the aid of ODES of MatLab.

The mathematical models described above are programmed in the MatLab editor with the aid of ODES and declaring functions the system is simulated. Then, the linearization of the entire system is done using *fsolve* of MatLab.

The complete system shown in Figure 2.1 is integrated into a function where all the dynamic models are declared as a function of themselves. The following sections capture the code of the complete system programmed, simulated, and solved in the editor of MatLab.

C.1   ODES code

The ordinary differential equation solver used to simulate the entire system is the ode23tb as shown in line 15 of the main code, in this line, the function System contains all the models programmed as function; the input and output are indicated. In this file, the main code encompasses all the programmed differential equations, where the variable t records the vector of time of the entire simulation and the variable y records the entire vector of the state variables.

```
1
2          dy = zeros;   % states initialization
3          % Initial Conditions
4
5          x2 = [0  0];      x5 = [0  0  0  0  0]; x10 = [x5  x5];
6          x01 = [1  0  1  x2  x2  1  x5  0  1  0  x10  x5  0]';
```

```
 7
 8          disp('Length of state variables:');
 9          length(x01)
10
11          % ODE's options
12          options=odeset('RelTol',1e-6,'AbsTol',1e-6);
13
14          % Differential equations solver
15          tic;[t,y]=ode23tb('System',[0,100],x01,options);toc;
```

C.2   Dynamic Model Integration

The MatLab function called System integrates all the differential equations explained in Section 2.2 and the state variables are defined and those ones are used as input in its corresponding mathematical model. The inputs, base values, state variables, *abc* to *dq* and *dq* to *abc* transformations, control references are indicated.

```
 1          function dy = System(t,y)
 2
 3          % Parameters (inputs)
 4          f = 60;              % base frequency
 5          nP = 6;              % pole number
 6          pp = nP/2;           % pole pair number
 7          Wb = 2*pi*f;         % angular velocity
 8          Wmb = Wb/pp;         % base mechanical speed
 9          Pb = (5/6)*2e6;      % base power
10          Tb = Pb/Wmb;         % base torque
11          Vbase = 575*sqrt(2/3);
12          Ibase = (Pb*sqrt(2)/(575*sqrt(3)));
13          Zbase = Vbase/Ibase;
14          Lbase = Zbase/Wb;
15          Cbase = 1/(Wb*Zbase);
16
17          %% References
18          Vdc_ref = 1150;
19          Vrms_ref = 1.0;
20          Wmpu_ref = 1.02;
21
22          %% States Variables
23          Wmpu     = y(1);              % generator mechanical speed
24          gama     = y(2);              % angular displacement
```

```
25        Wwtpu    = y(3);              % turbine  mechanical  speed
26        Iqs      = y(4);              % stator  current  of q component
27        Ids      = y(5);              % stator  current  of d component
28        Iqr      = y(6);              % rotor  current  of q component
29        Idr      = y(7);              % rotor  current  of d component
30        Wi       = y(8)*Wb;           % PLL  auxiliarly  angular  speed
31        gamaB1   = y(9);              % PLL  auxiliarly  angular
             position
32        Xidg     = y(10);             % GSCC  auxiliarly  variable
33        Xvdg     = y(11);             % GSCC  auxiliarly  variable
34        Xvqg     = y(12);             % GSCC  auxiliarly  variable
35        Idg      = y(13);             % GSC  current  of d component
36        Iqg      = y(14);             % GSC  current  of q component
37        Vdcf     = y(15)*Vdc_ref;         % BtB DC voltage
38        X1       = y(16);             % digital-filter  auxiliarly
             variable
39        X2       = y(17);             % digital-filter  auxiliarly
             variable
40        Xus      = y(18);             % RSCC  auxiliarly  variable
41        Xvdr     = y(19);             % RSCC  auxiliarly  variable
42        Xw       = y(20);             % RSCC  auxiliarly  variable
43        Xvqr     = y(21);             % RSCC  auxiliarly  variable
44        Vdct     = y(22);             % synchronously  voltage  at  bus
             B1
45        Vqct     = y(23);             % synchronously  voltage  at  bus
             B1
46        Idcol    = y(24);             % transmission  line  current
47        Iqcol    = y(25);             % transmission  line  current
48        Vdcs     = y(26);             % series  capacitor  voltage
49        Vqcs     = y(27);             % series  capacitor  voltage
50        Xep      = y(28);             % BESS  control  auxiliarly
             variable
51        Xid      = y(29);             % BESS  control  auxiliarly
             variable
52        Xiq      = y(30);             % BESS  control  auxiliarly
             variable
53        Idb      = y(31);             % BESS  current
54        Iqb      = y(32);             % BESS  current
55
56
57        %% reference  frame  (synchronous)
```

```matlab
58      Kiw  =1/1.6667;              % auxiliary
59      Wau = -Xw/Kiw;              % auxiliary
60      Thetar  = Wb*(Wmpu_ref*t+Wau);
61      Thetaf  = Wb*t;
62      Betaf  = Thetaf-Thetar;
63      ThetaB1  = mod(Wb*t+gamaB1,2*pi);

64
65      %% avoid zero-crosing
66      if  Vdcf <  0.001
67      Vdc =  0.001;
68      else
69      Vdc =  Vdcf;
70      end

71
72      %% Transformations  matrices  abc2dq  and  dq2abc  (
            synchronous)
73      Tdq02abc  =  [ sin(Thetaf)             cos(Thetaf)            1
74      sin(Thetaf-2*pi/3)  cos(Thetaf-2*pi/3)  1
75      sin(Thetaf+2*pi/3)  cos(Thetaf+2*pi/3)  1];

76
77      Tabc2dq   = (2/3)*[ sin(Thetaf)   sin(Thetaf-2*pi/3)   sin(
            Thetaf+2*pi/3)
78      cos(Thetaf)    cos(Thetaf-2*pi/3)    cos(Thetaf+2*pi/3)
79      1/2                1/2                     1/2];

80
81      Tdq02abcR =  [ sin(Betaf)            cos(Betaf)            1
82      sin(Betaf-2*pi/3)  cos(Betaf-2*pi/3)  1
83      sin(Betaf+2*pi/3)  cos(Betaf+2*pi/3)  1];

84
85      %% States  dq0  to  abc
86      Idqg    = [Idg  Iqg  0]';
87      Idqr    = [Idr  Iqr  0]';

88
89      Ig      = Tdq02abc*Idqg;
90      Ir      = Tdq02abcR*Idqr;

91
92      %% Source
93      vp =  575*sqrt(2/3);
94      Vpa =  vp*sin(Wb*t);
95      Vpb =  vp*sin(Wb*t-2*pi/3);
96      Vpc =  vp*sin(Wb*t+2*pi/3);
```

```
97          Vso = [ Vpa  Vpb  Vpc ] '/ Vbase ;

98

99          Vdqso = Tabc2dq∗Vso ;
100         Vdso = Vdqso ( 1 ) ;  Vqso = Vdqso ( 2 ) ;

101

102         %% Voltage  bus  B1
103         [ VdB1 , VqB1 , dVdct , dVqct ] = VoltageB1 ( Vdct , Vqct , Idcol ,
                 Iqcol , Ids , Iqs , Idg , Iqg , Idb , Iqb , Zbase , Cbase ,Wb) ;
104         VdqB1 = [ VdB1  VqB1  0 ] ';
105         VB1 = Tdq02abc∗VdqB1 ;

106

107         %% Powers
108         Pgs = VdB1∗( Ids+Idg )+VqB1∗( Iqs+Iqg ) ;
109         Qgs = VqB1∗( Ids+Idg )−VdB1∗( Iqs+Iqg ) ;
110         Pbes = VdB1∗Idb+VqB1∗Iqb ;
111         Qbes = VqB1∗Idb−VdB1∗Iqb ;

112

113         %% Line  model
114         y l i = [ Idcol , Iqcol , Vdcs , Vqcs ] ';
115         d y l i = LineSec ( y l i , t , Vdso , Vqso , VdB1 , VqB1 , Cbase , Lbase ,Wb)
                 ;

116

117         %% Wind  and  Turbine  Model
118         yWIM = [ Wwtpu ,  Wmb,  Tb ] ';
119         Twtpu = Turbine ( t ,yWIM) ;

120

121         %% Drive  Train  Model
122         yDTM = [ Wwtpu ,  Wmb,  gama ,  Wmpu,  Twtpu ] ';
123         [ Tmpu , dWwtpu , dgama ] = Shaft ( yDTM) ;

124

125         %% PLL  Model
126         [ dWi , dgamaB1 , Ws , VdB1c , VqB1c ] = PLL ( ThetaB1 , Wi , f ,Wb, VB1 ) ;

127

128         %% BESS  model
129         Ew = Wmpu_ref−Wmpu ;

130

131         yb = [ Xep  Xid  Xiq  Idb  Iqb ] ';
132         dyb = BESS(Ew, t , yb , VdB1 , VqB1 , VdB1c , VqB1c , Ws , Thetaf ,
                 ThetaB1 , Zbase , Vbase , Cbase ,Wb, Pgs , Pbes , Qgs , Qbes ) ;

133

134         %% Grid−Side  Converter  and  Control
```

```
135          [dXidg,dXvdg,dXvqg,dIdg,dIqg,Sg] = GSC(t,ThetaB1,Ig,
                Vbase,Wb,Vdc_ref,Vdc,Xidg,Xvdg,Xvqg,VdB1c,VqB1c,VdB1,
                VqB1,Ws,Zbase,Thetaf);

136

137      %% Rotor-Side Converter and Control
138          [dX1,dX2,dXus,dXvdr,dXw,dXvqr,Vqr,Vdr,Sr] = RSC(Wmpu_ref
                ,Vrms_ref,X1,X2,Xus,Xvdr,Xw,Xvqr,Iqs,Iqr,Ids,Idr,Ir,
                Thetar,Betaf,VdB1,VqB1,Wmpu,Ws,Vdc,Zbase,Vbase,Wb,t);

139

140      %% Dc-Link Back to Back Converter
141          dVdcf = dcLink(Vdc_ref,Wb,Zbase,Ig,Ir,Sg,Sr);

142

143      %% DFIG Model (synchronous reference frame)
144          [didt, dWmpu, dThetam] = DFIG(Wmb,Wb,Wmpu,pp,Ids,Iqs,Idr
                ,Iqr,VdB1,VqB1,Vdr,Vqr,Tmpu);

145

146      %% Vector of differencial equations
147          dy = [dWmpu dgama dWwtpu didt dWi dgamaB1 dXidg dXvdg
                dXvqg dIdg dIqg dVdcf dX1 dX2 dXus dXvdr dXw dXvqr
                dVdct dVqct dyli dyb];
```

C.3   MatLab Voltage of bus B1 Model

This function is used to calculate the voltage in *dq* synchronous reference frame of the bus B1 in any system operation condition.

```
1          function [VdB1,VqB1,dVdct,dVqct] = VoltageB1(Vdct,Vqct,
                Idcol,Iqcol,Ids,Iqs,Idg,Iqg,Idb,Iqb,Zbase,Cb,Wb)

2

3      %% Parameters
4      Rt = 0;%1e3/Zbase;  % en pu
5      Ct = 1e-3/Cb;
6      % Rli = 10e-3/Zbase;
7      %% Voltage bus B1
8      Idt = Idcol-Ids-Idg-Idb;
9      Iqt = Iqcol-Iqs-Iqg-Iqb;
10     dVdct = Wb*(Idt+1*Ct*Vqct)/Ct;
11     dVqct = Wb*(Iqt-1*Ct*Vdct)/Ct;
12     VdB1 = Vdct+Rt*Idt;
13     VqB1 = Vqct+Rt*Iqt;
```

C.4 MatLab Transmission Line and Series Compensation Model

This function models the transmission line and the series compensation as well. The series compensation is codified by changing the constant in line 14.

```matlab
function dyli = LineSec(yli, t, Vdso, Vqso, VdB1, VqB1, Cbase, Lbase, Wb)

%% States Variables
Idcol = yli(1);
Iqcol = yli(2);
Vdcs  = yli(3);
Vqcs  = yli(4);

%% Parameters
Lt = 0.005/3;            % in pu, transformer impedance
Lnt = 0.006;            % in pu, system impedance
Ll = 0.4*0.049321323;   % in pu, line impedance
Xl = Ll*Lbase*Wb;       % reactance
Xcs = 0.1*Xl;           % series compensation

if t > 100
Xcs = 0.8*Xl;
end

Ltot = Ll+Lt+Lnt;
Cs = (1/(Xcs*Wb))/Cbase;
Rtot = 0.02772526;      % in pu, line and transmformer

dIdcol = Wb*(Vdso-VdB1-Vdcs-Rtot*Idcol+1*Ltot*Iqcol)/Ltot;
dIqcol = Wb*(Vqso-VqB1-Vqcs-Rtot*Iqcol-1*Ltot*Idcol)/Ltot;

dVdcs = Wb*(Idcol+1*Cs*Vqcs)/Cs;
dVqcs = Wb*(Iqcol-1*Cs*Vdcs)/Cs;

dyli = [dIdcol dIqcol dVdcs dVqcs];
```

C.5 MatLab Wind and Turbine Model

The wind turbine is modeled in *per − unit* system, the output of this model is the mechanical torque delivered by the wind speed; the wind speed is a constant.

```matlab
function Twtpu = Turbine(t,yWTM)

Wwtpu = yWTM(1);
Wmb   = yWTM(2);
Tb    = yWTM(3);
Vw = 13;                % wind speed velocity m/s

if t > 300
Vw = 13;
end

DA = 1.225;             % (kg/m^3) air density
Rwt = 37.5;             % (mts) blade radius
C1 = 0.73; C2 = 151; C3 = 0.58; C4 = 0.002; C5 = 2.14;
    C6 = 13.2; C7 = 18.4; C8 = -0.02; C9 = -0.003;
Lamda = 8.1; % 8.1
The = 0.05362346*180/pi; % beta, pitch angle
Lamdai = ((1/(Lamda+C8*The))-(C9/(The^3+1)))^-1;
Cp = C1*(C2/Lamdai-C3*The-C4*The^C5-C6)*exp(-C7/Lamdai);
Awt = pi*Rwt^2;
Pwt = 0.5*DA*Awt*Cp*Vw^3;
Twt = Pwt/(Wwtpu*Wmb);
Twtpu = Twt/Tb;
```

C.6 MatLab Drive Train Model

The drive train model delivers the mechanical torque to the induction machine.

```matlab
function [Tmpu,dWwtpu,dgama] = Shaft(yDTM)

%% Drive train model

Wwtpu = yDTM(1);
Wmb   = yDTM(2);
gama  = yDTM(3);
Wmpu  = yDTM(4);
```

```
9        Twtpu = yDTM(5);

10

11       Ks = 1.11;   % Shaft Stiffness
12       D = 1.5;      % Mutual Damping
13       Hwt = 4.32;   % Inertia Constant

14

15       Tmpu = Ks*gama+D*Wmb*(Wwtpu−Wmpu);
16       dWwtpu = (Twtpu−Tmpu)/(2*Hwt);
17       dgama = Wmb*(Wwtpu−Wmpu);
```

C.7 MatLab Phase-Locked Loop (PLL) Model

The PLL is modeled using a change of variable, it is due to the linearization algorithm (computed by the function *fsolve*) requires to find out a equilibrium point. Then, the differential equation $\frac{d\theta^{\varepsilon}}{dt} = K_{Ipll}\omega_s dt$ (described in Section 2.2.10) is changed as it is shown in the lines 19 and 20.

```
1        function [dWi,dgamaB1,Ws,VdB1c,VqB1c] = PLL(ThetaB1,Wi,f
            ,Wb,VB1)

2

3        % PLL bus B1

4

5        Kp = 180;
6        Ki = 3200;
7        % Kit = 1;

8

9        Tv = (2/3)*[sin(ThetaB1)  sin(ThetaB1−2*pi/3)  sin(ThetaB1
            +2*pi/3)
10       cos(ThetaB1)  cos(ThetaB1−2*pi/3)  cos(ThetaB1+2*pi/3)
11       1/2        1/2                 1/2];

12

13       VdqB1c = Tv*VB1;
14       VdB1c = VdqB1c(1);
15       VqB1c = VdqB1c(2);
16       dWi = Ki*VqB1c/Wb;
17       W = Kp*VqB1c+Wi;
18       Freq = W/(2*pi);
19       % dThetaB1 = Kit*W;
20       dgamaB1 = W−Wb;
21       Ws = Freq/f;
```

C.8 MatLab BESS Model

The BESS model and its controls are modeled without reactive power control due to the RSCC performs such task. This function is modeled in *pu* system.

```matlab
function dyb = BESS(Ew,t,yb,VdB1,VqB1,VdB1c,VqB1c,Ws,
    Thetaf,ThetaB1,Zbase,Vbase,Cbase,Wb,Pgs,Pbes,Qgs,Qbes)

%% Variable states
Xep     = yb(1);
Xid     = yb(2);
Xiq     = yb(3);
Idb     = yb(4);
Iqb     = yb(5);


%% Transformation
Tabc2dq   = (2/3)*[ sin(Thetaf)   sin(Thetaf-2*pi/3)   sin(
    Thetaf+2*pi/3)
cos(Thetaf)   cos(Thetaf-2*pi/3)   cos(Thetaf+2*pi/3)
1/2                1/2                   1/2];

Tdq2abc = [sin(Thetaf)           cos(Thetaf)          1
sin(Thetaf-2*pi/3)  cos(Thetaf-2*pi/3)  1
sin(Thetaf+2*pi/3)  cos(Thetaf+2*pi/3)  1];

Tabc2dqB1   = (2/3)*[ sin(ThetaB1)   sin(ThetaB1-2*pi/3)
    sin(ThetaB1+2*pi/3)
cos(ThetaB1)   cos(ThetaB1-2*pi/3)   cos(ThetaB1+2*pi/3)
1/2                1/2                     1/2];
Idqb = [Idb Iqb 0]';
Ib = Tdq2abc*Idqb;
Idqbc = Tabc2dqB1*Ib;
Idbc = Idqbc(1); Iqbc = Idqbc(2);

%% parameters
Lb = 0.3; % en pu
Rb = 0.003; % en pu
Rsw = 1e-3/Zbase;

% gains loop d
Kpf = 0.1595;
Kif = 1/0.25;
```

```
35        Kpid = 3;
36        Kiid = 80;
37
38        % gains loop q
39        Kpv =  0.1595;%8;
40        Kiv =  1/0.25;%1/2.5e-3;
41        Kpiq = 3;
42        Kiiq = 80;
43
44        % references
45
46        P_ref = -1;
47        Ubdc = 1200;
48        tbess = 10; % BESS strarting time
49
50        % d frame
51        eP = P_ref-Pgs-Pbes;
52
53        if t<tbess; eP = 0; end
54
55        dXep = Kif*eP;
56        Id_ref = Kpf*eP+Xep;
57
58        if t<tbess; Id_ref = 0; end
59
60        Eid = Id_ref-Idb;
61        dXid = Kiid*Eid;
62        Vd_ = Eid*Kpid+Xid;
63
64        if Vd_ > 1.1; Vdbs = 1.1; elseif Vd_ < -1.1;
65        Vdbs = -1.1; else Vdbs= Vd_; end
66
67        % q frame
68        Iq_ref = 0.00;
69        Eiq = Iq_ref-Iqb;
70        dXiq = Eiq*Kiiq;
71        Vq_ = Eiq*Kpiq+Xiq;
72
73        if Vq_ > 1.1; Vqbs = 1.1; elseif Vq_ < -1.1;
74        Vqbs = -1.1; else Vqbs = Vq_; end
75
```

```
76      Vdbctr = VdB1+1*Lb*Iqb-Vdbs;
77      Vqbctr = VqB1-1*Lb*Idb-Vqbs;
78      Vdq = sqrt(Vdbctr^2+Vqbctr^2);
79      thetabs = atan2(Vqbctr,Vdbctr);
80      Vdqbss = Vdq*2*Vbase/Ubdc;
81
82      if Vdqbss > 1.1;
83      Vdqbs = 1.1;
84      elseif Vdqbss <= 0;
85      Vdqbs = 0;
86      else
87      Vdqbs = Vdqbss;
88      end
89
90      Vdbpwm = Vdqbs*cos(thetabs);
91      Vqbpwm = Vdqbs*sin(thetabs);
92      Vdqbpwm = [Vdbpwm Vqbpwm 0]';
93
94      Tvi = [sin(Thetaf)            cos(Thetaf)           1
95      sin(Thetaf-2*pi/3)  cos(Thetaf-2*pi/3)  1
96      sin(Thetaf+2*pi/3)  cos(Thetaf+2*pi/3)  1];
97
98      Vabcbpwm = Tvi*Vdqbpwm;
99      Vbmoda = Vabcbpwm(1);
100     Vbmodb = Vabcbpwm(2);
101     Vbmodc = Vabcbpwm(3);
102     Sba = Vbmoda/2+1/2;
103     Sbb = Vbmodb/2+1/2;
104     Sbc = Vbmodc/2+1/2;
105     Sbx = (1/3)*(Sba+Sbb+Sbc);
106     Vbvsc = Ubdc*[Sba-Sbx Sbb-Sbx Sbc-Sbx]';
107     Vdqb = Tabc2dq*Vbvsc/Vbase;
108     Vdbvsc = Vdqb(1); Vqbvsc = Vdqb(2);
109
110     %% Filter Chuck equations for the BESS
111     We = 1;
112     dIdb = Wb*(VdB1+We*Lb*Iqb-(Rb+Rsw)*Idb-Vdbvsc)/Lb;
113     dIqb = Wb*(VqB1-We*Lb*Idb-(Rb+Rsw)*Iqb-Vqbvsc)/Lb;
114     dyb = [dXep dXid dXiq dIdb dIqb];
```

C.9 MatLab Grid-Side Converter and Controller Model

The GSCC and the VSC are modeled in this function, the voltage-oriented reference frame is used for the controller and the synchronous reference frame is used to model the VSC.

```matlab
function [dXidg,dXvdg,dXvqg,dIdg,dIqg,Sg] = GSC(t,
    ThetaB1,Ig,Vbase,Wb,Vdc_ref,Vdc,Xidg,Xvdg,Xvqg,VdB1c,
    VqB1c,VdB1,VqB1,Ws,Zbase,Thetaf)

%% Grid-Side Converter
% Transformation Matrix
Tabc2dqB1 = (2/3)*[ sin(ThetaB1)   sin(ThetaB1-2*pi/3)
    sin(ThetaB1+2*pi/3)
cos(ThetaB1)   cos(ThetaB1-2*pi/3)   cos(ThetaB1+2*pi/3)
1/2              1/2                    1/2];
Tabc2dq = (2/3)*[ sin(Thetaf)   sin(Thetaf-2*pi/3)   sin(
    Thetaf+2*pi/3)
cos(Thetaf)   cos(Thetaf-2*pi/3)   cos(Thetaf+2*pi/3)
1/2              1/2                    1/2];

Idqgc = Tabc2dqB1*Ig;
Idgc = Idqgc(1); Iqgc = Idqgc(2);

Kp1 = 8;
Ki1 = 1/2.5e-3;
Kp2 = 0.83;
Ki2 = 1/0.2;

Lg = 0.3;
Rg = 0.003;

Evdc = (Vdc_ref-Vdc)/Vdc_ref;
dXidg = Ki1*Evdc;
Idg_ref = Kp1*Evdc+Xidg;
Eidg = Idg_ref-Idgc;
dXvdg = Ki2*Eidg;
Vdgs = Kp2*Eidg+Xvdg;

if Vdgs > 1.1; Vdg = 1.1; elseif Vdgs < -1.1; Vdg =
    -1.1;
else Vdg = Vdgs; end
```

```matlab
33          Iqg_ref = 0;
34          Eiqg = Iqg_ref-Iqgc;
35          dXvqg = Ki2*Eiqg;
36          Vqgs = Kp2*Eiqg+Xvqg;

38          if Vqgs > 1.1; Vqg = 1.1; elseif Vqgs < -1.1; Vqg =
                -1.1;
39          else Vqg = Vqgs; end

41          Vdgctr = VdB1c+Ws*Lg*Iqgc-Vdg;
42          Vqgctr = VqB1c-Ws*Lg*Idgc-Vqg;
43          Vdqgb = sqrt(Vdgctr^2+Vqgctr^2);
44          thetag = atan2(Vqgctr,Vdgctr);
45          Vdqgs = Vdqgb*Vbase*2/Vdc;

47          if Vdqgs > 1.1; Vdqg = 1.1; elseif Vdqgs <= 0; Vdqg = 0;
48          else Vdqg = Vdqgs; end

50          if t < 0.0; mar = 0.1; Vdqg = mar*Vbase*2/Vdc;
51          thetag = -10*pi/180; dXidg = 0; dXvdg = 0; dXvqg = 0;
                end

53          Vdgpwm = Vdqg*cos(thetag);
54          Vqgpwm = Vdqg*sin(thetag);
55          Vdqgpwm = [Vdgpwm Vqgpwm 0]';

57          Tvi = [sin(ThetaB1)           cos(ThetaB1)           1
58          sin(ThetaB1-2*pi/3) cos(ThetaB1-2*pi/3) 1
59          sin(ThetaB1+2*pi/3) cos(ThetaB1+2*pi/3)  1];

61          Vabcgpwm = Tvi*Vdqgpwm;
62          Vgmoda = Vabcgpwm(1);
63          Vgmodb = Vabcgpwm(2);
64          Vgmodc = Vabcgpwm(3);

66          Sga = Vgmoda/2+1/2;
67          Sgb = Vgmodb/2+1/2;
68          Sgc = Vgmodc/2+1/2;
69          Sg  = [Sga Sgb Sgc]';
70          Sgx = (1/3)*(Sga+Sgb+Sgc);
71          Vgvsc = Vdc*[Sga-Sgx Sgb-Sgx Sgc-Sgx]';
```

```
72
73          % inductance y series resistance (Choke filter)
74          Rch = Rg;
75          Lch = Lg;
76          rsw = 1e-3/Zbase;
77
78          Vdqgx = Tabc2dq*Vgvsc/Vbase;
79          Vdvscg = Vdqgx(1); Vqvscg = Vdqgx(2);
80          Idqg = Tabc2dq*Ig;
81          Idg = Idqg(1); Iqg = Idqg(2);
82
83          dIdg = Wb*(VdB1+Ws*Lch*Iqg-Vdvscg-Idg*(Rch+rsw))/(Lch);
84          dIqg = Wb*(VqB1-Ws*Lch*Idg-Vqvscg-Iqg*(Rch+rsw))/(Lch);
```

C.10   MatLab Rotor-Side Converter and Controller Model

The RSCC and the VSC are modeled in this function, the flux-rotor reference frame is used for the controller and the rotor reference frame is used to model the VSC. To avoid errors due to zero integration, the states variables to be controlled in the RSCC begin in opened-loop.

```
1          function [dX1,dX2,dXus,dXvdr,dXw,dXvqr,Vqr,Vdr,Sr] = RSC
               (Wmpu_ref,Vrms_ref,X1,X2,Xus,Xvdr,Xw,Xvqr,Iqs,Iqr,Ids,
               Idr,Ir,Thetar,Betaf,VdB1,VqB1,Wmpu,Ws,Vdc,Zbase,Vbase,
               Wb,t)
2
3          % Rotor-Side Converter
4          tctr = 1; % RSCC starting time
5          Lls = 0.18;
6          Lm  = 2.9;
7          Llr = 0.16;
8          Lr = Llr+Lm;
9          Ls = Lls+Lm;
10         rsw = 1e-3/Zbase;
11
12         % fluxes in the synchronous reference frame
13         Fqs = (Iqs*Ls+Iqr*Lm);
14         Fds = (Ids*Ls+Idr*Lm);
15         Fss = sqrt(Fds^2+Fqs^2);
```

```
16        Phi_P = atan2(Fqs,Fds);
17        if t < tctr*0.1; Phi_P = 0; end
18
19        % filter for the flux
20        Z = 1;
21        Wo = 10*2*pi;
22        G = 1;
23        dX1 = X2;
24        dX2 = -2*Z*Wo*X2-Wo^2*X1+Wo^2*Phi_P*G;
25        Phi = X1;
26
27        ThetaPhi = mod(Wb*t+Phi,2*pi);
28        ThetaPR = ThetaPhi-Thetar;
29
30        if Fss <= 0.01; Fs = 0.01; else Fs = Fss; end
31
32        % Rotor currents transformation into ThetaPR refernce
              frame
33        Tabc2dqR = (2/3)*[ sin(ThetaPR)   sin(ThetaPR-2*pi/3)
              sin(ThetaPR+2*pi/3)
34        cos(ThetaPR)   cos(ThetaPR-2*pi/3)   cos(ThetaPR+2*pi/3)
35        1/2                1/2                      1/2];
36
37        Idq0r_F = Tabc2dqR*Ir;
38        Idr_F = Idq0r_F(1);
39        Iqr_F = Idq0r_F(2);
40
41        % Proportional and integral gains
42        Kpus = 2;
43        Kius = 1/0.05;
44        Kpidr = 0.01;
45        Kiidr = 1/4;
46        Kpw = 5.3731;
47        Kiw =1/1.6667;
48        Kpiqr = 0.05;
49        Kiiqr = 1/0.02;
50
51        VrmsB1 = sqrt(VdB1^2+VqB1^2);
52        Evrms = Vrms_ref-VrmsB1;
53
54        if t < tctr*1.3; Evrms = 0; end
```

```
55          dXus = Kius*Evrms;
56          Idr_ref = Kpus*Evrms+Xus;
57
58          Eidr = Idr_ref-Idr_F;
59          if  t < tctr*1.3;  Eidr = 0;  end
60          dXvdr = Kiidr*Eidr;
61          Vdrs = Kpidr*Eidr+Xvdr;
62
63          if Vdrs > 1.1;  Vdrc = 1.1;  elseif Vdrs < -1.1;  Vdrc =
                -1.1;
64          else  Vdrc = Vdrs;  end
65
66          Ew = Wmpu_ref-Wmpu;
67          if  t < tctr;  Ew = 0;  end
68          dXw = Kiw*Ew;
69          Iqr_ref_p = Kpw*Ew+Xw;
70          Iqr_ref = -Iqr_ref_p*Ls/(Lm*Fs);
71
72          Eiqr = Iqr_ref-Iqr_F;
73          if  t < tctr;  Eiqr = 0;  end
74          dXvqr = Kiiqr*Eiqr;
75          Vqrs = Kpiqr*Eiqr+Xvqr;
76
77          if Vqrs > 1.1;  Vqrc = 1.1;  elseif Vqrs < -1.1;  Vqrc =
                -1.1;
78          else  Vqrc = Vqrs;  end
79
80          Wslip = Ws-Wmpu;
81          alpha = 1-(Lm^2/(Ls*Lr));
82
83          Vdrctr = Vdrc-Wslip*alpha*Lr*Iqr_F;
84          Vqrctr = Vqrc+Wslip*(Fs*Lm/Ls+Lr*alpha*Idr_F);
85          Vdqrb = sqrt(Vdrctr^2+Vqrctr^2);
86          thetar = atan2(Vqrctr,Vdrctr);
87          Vdqrs = Vdqrb*Vbase*2/Vdc;
88
89          if Vdqrs > 1.1;  Vdqr = 1.1;  elseif Vdqrs <= 0;  Vdqr = 0;
90          else  Vdqr = Vdqrs;  end
91
92          Vdrpwm = Vdqr*cos(thetar);
93          Vqrpwm = Vdqr*sin(thetar);
```

```
94
95          if  t < tctr;  Vdrpwm = 0;  Vqrpwm = 0;  end
96          Vdqrpwm = [Vdrpwm Vqrpwm 0]';
97
98          Tvir = [sin(ThetaPR)              cos(ThetaPR)              1
99          sin(ThetaPR-2*pi/3)  cos(ThetaPR-2*pi/3)   1
100         sin(ThetaPR+2*pi/3)  cos(ThetaPR+2*pi/3)    1];
101
102         Vabcpwmr = Tvir*Vdqrpwm;
103         Vrmoda = Vabcpwmr(1);
104         Vrmodb = Vabcpwmr(2);
105         Vrmodc = Vabcpwmr(3);
106
107         Sra = Vrmoda/2+1/2;
108         Srb = Vrmodb/2+1/2;
109         Src = Vrmodc/2+1/2;
110         Sr = [Sra Srb Src]';
111         Srx = (1/3)*(Sra+Srb+Src);
112         Vrvsc = Vdc*[Sra-Srx Srb-Srx Src-Srx]';
113
114         Vr = Vrvsc/Vbase-Ir*rsw;      % Rotor voltage [pu]
115
116         % Rotor
117         Vrab = Vr(1)-Vr(2);
118         Vrbc = Vr(2)-Vr(3);
119         Tvrotor = (1/3)*[2*cos(Betaf)  cos(Betaf)+sqrt(3)*sin(
                Betaf)
120         2*sin(Betaf)  sin(Betaf)-sqrt(3)*cos(Betaf)];
121
122         Vrqd = Tvrotor*[Vrab Vrbc]';
123         Vqr = Vrqd(1);
124         Vdr = Vrqd(2);
```

C.11   MatLab DC-link and Back-to-Back Converter Model

The function of the DC-link and back-to-back is modeled as its fundamental model.

```
1          function  dVdcf = dcLink(Vdc_ref,Wb,Zbase,Ig,Ir,Sg,Sr)
2
```

```
3          % B2B parameters
4          Cbase = 1/(Wb*Zbase);
5          Cdcf = 0.01/Cbase;
6
7          % capacitor equations
8          Igdc = Ig(1)*Sg(1)+Ig(2)*Sg(2)+Ig(3)*Sg(3);
9          Irdc = Ir(1)*Sr(1)+Ir(2)*Sr(2)+Ir(3)*Sr(3);
10
11         dVdcf = Wb*(Igdc-Irdc)/(Cdcf);
```

C.12   MatLab DFIG Model

The staring condition of the induction machine is zero, the differential equations are solved according its currents, and the the induction machine is modeled in *pu* system. The phase of the mechanical position (θ_m) of the induction machine (as it is shown in line 40 of the function) needs a change of variable to avoid that the state variable increase indefinitely.

```
1          function [didt, dWmpu, dThetam] = DFIG(Wmb,Wb,Wmpu,pp,
               Ids,Iqs,Idr,Iqr,Vds,Vqs,Vdr,Vqr,Tmpu)
2
3          %% induction machine equations
4          Rs  = 0.023;
5          Rr  = 0.016;
6          Lls = 0.18;
7          Llr = 0.16;
8          Lm  = 2.9;
9          Hg  = 0.685;
10         F   = 0.01;
11
12         Ls = Lls+Lm;
13         Lr = Llr+Lm;
14
15         % Rotor reference frame
16         wr = Wmpu*Wmb*pp/Wb;    % pu
17         wf = Wb/Wb;             % pu
18
19         L = [Ls  0   Lm  0
20         0   Ls  0   Lm
21         Lm  0   Lr  0
22         0   Lm  0   Lr ];
23
```

```
24        Fiqs = (Ls*Iqs+Lm*Iqr);
25        Fids = (Ls*Ids+Lm*Idr);
26        Fiqr = (Lr*Iqr+Lm*Iqs);
27        Fidr = (Lr*Idr+Lm*Ids);
28
29        Vqdsr = [Vqs-Rs*Iqs-wf*Fids
30        Vds-Rs*Ids+wf*Fiqs
31        Vqr-Rr*Iqr-(wf-wr)*Fidr
32        Vdr-Rr*Idr+(wf-wr)*Fiqr];
33
34        didt = Wb*L^-1*Vqdsr;
35
36        % Te = 1.5*pp*(Fiqs*Ids-Fids*Iqs); % physical units
37        Te = Lm*(Iqr*Ids-Idr*Iqs);              % pu
38
39        dWmpu = (1/(2*Hg))*(Tmpu-Te-F*Wmpu); % pu
40        dThetam = Wmb*Wmpu;
```